ANALYSIS OF INSTABILITIES AND THEIR IMPACT ON FRICTION FACTOR IN HOLE-PATTERN SEALS

A Dissertation

by

AARTHI SEKARAN

Submitted to the Office of Graduate Studies of
Texas A&M University
in partial fulfillment of the requirements for the degree of

DOCTOR OF PHILOSOPHY

Approved by:

Chair of Committee,	Gerald L.Morrison
Committee Members,	Robert A.Handler
	Devesh Ranjan
	Prabir Daripa
Head of Department,	Jerald A.Caton

December 2012

Major Subject: Mechanical Engineering

ABSTRACT

The determination of the leakage and consequently the friction factor is an important part of analyzing the flow through a seal. This is done experimentally by means of a flat plate tester, which allows for the simplified representation of the seal pattern on a flat plate surface tested under a range of clearances and pressure drops. The setup mounts a smooth plate opposite a second plate which may be smooth or have a roughened surface while the separation between plates is held constant. The present study analyzes the phenomenon of friction factor 'upset' – wherein it was seen that as the pressure drop across the parallel plates is increased, there is a sudden increase in the friction factor (i.e. a decrease in flow rate) at a certain Reynolds number and for any further increase in the pressure differential, the friction factor shows the expected trend and decreases slowly. This phenomenon was initially believed to be an anomaly in the rig and was attributed to choking at an upstream flow control valve. The present author differs from that view and hypothesized that the reason for the abrupt change is linked to the flow mechanics of the system and the current study analyzes the same.

Preliminary analysis of available data has established that the cause for the 'upset' was not related to the switch from a normal mode resonance driven by the Helmholtz frequency of the cavities on the stator to a shear layer instability, as was seen earlier by Ha. The friction factor jump for this case is therefore proposed to be due to a change of the instability modes as the fluid passes over the cavities in the plate. A

detailed analysis of the physics of the flow will be carried out via a numerical simulation using a Large Eddy Simulation (LES) model from ANSYS Fluent. Results will be validated through comparisons with experimental data from the flat plate test rig.

This is dedicated to you, dad. I couldn't have done this without you.

.

ACKNOWLEDGEMENTS

I would like to thank the chair of my committee, Dr. Gerald Morrison whose continued support and encouragement throughout my stay here at A&M has been invaluable. I've learned a lot from him in terms of both technical knowledge and also about being a great teacher. I could not have asked for a better advisor and mentor for my doctoral study.

In addition to my advisor, I would like to thank the rest of my dissertation committee – Dr. Robert Handler, Dr. Devesh Ranjan and Dr. Prabir Daripa. Their insightful comments and suggestions during this study have helped encourage me to look at the problem differently and more thoroughly. I would also like to thank Dr. Childs for allowing me to use the flat plate test rig which is a part of this test cell at the Turbomachinery laboratory.

Thanks also go to my friends and colleagues at the Turbomachinery laboratory at Texas A&M University. In particular, I am grateful to Abhay Patil, Stephen Arthur and Shankar Narayanan for helping me with the setup and running of the rig. My sincere thanks also go out to the faculty and staff of the Mechanical Engineering Department for making my time at Texas A&M University a great experience.

I am indebted to my family for all their love and support through the duration of my study – dad, you have always been and will always be my hero; Preethi, you've been my best cheerleader through everything. I'd also like to thank my fiancée, Saikishan for

his love and encouragement; Sai, your optimism is contagious and has driven me to dream bigger. Finally, I'd like to thank Sai's parents – Mrs. Suryaprabha and Mr. Suryanarayanan. Being a part of their family has made me feel truly blessed and encouraged me to give my best, in research and in life.

Finally, I'd like to acknowledge that A&M has given me some of the best years of my life this far. It is true – 'There's a spirit that can ne'er be told'.

NOMENCLATURE

Greek

α	Empirical constant corresponding to phase delay (time between upstream receptivity and vortex-corner interaction)
δ_{ij}	Dirac delta function
κ	Empirical constant corresponding to average convection speed of vortices
γ	Ratio of specific heats
γ_A	Area ratio
λ	Wavelength
η	Kolmogorov length scale
ρ	Density of air [ML^{-3}]
ρ_{flow}	Density at the flow meter [ML^{-3}]
σ_{ij}	Viscous stress tensor
θ	Momentum thickness of boundary layer [L]
θ_0	Momentum thickness of boundary layer at upstream edge of cavity
τ	Time lag [T]
τ_f	Wall shear stress [$ML^{-1}\ T^{-2}$]
τ_{ij}	Subgrid stress tensor
μ	Dynamic viscosity [$ML^{-1}\ T^{-1}$]
μ_t	Eddy viscosity

Roman

A/D	Analog-to-digital converter
A	Cross-sectional area of channel [L^2]
A_S	Surface area [L^2]
CFD	Computational Fluid Dynamics
C_{ph}	Convective speed of vortices
C_{pl}	Clearance between plates [L]
C_S	Smagorinsky constant
dρ	Change in density across control volume [ML^{-3}]
dx	Differential length of control volume [L]
dp	Differential pressure across control volume [$ML^{-1}\ T^{-2}$]
dV	Differential velocity across control volume [LT^{-1}]
D	Depth of cavity [L]
D_h	Hydraulic diameter [L]
DNS	Direct Numerical Simulations
f	Dominant shedding frequency
f_f	Fanning friction factor
G	Filter function in ANSYS Fluent
H	Local clearance [L]
HP	Hole-pattern seals
h_d	Hole depth [L]

h_φ	Hole diameter [L]
L	Length of cavity [L]
L_S	Mixing length for subgrid scales (LES) [L]
LES	Large Eddy Simulations
M	Mach number
$\dot{m}$	Mass flow rate [MT^{-1}]
P	Pressure [$ML^{-1}\ T^{-2}$]
P_{exit}	Exit pressure at test section [$ML^{-1}\ T^{-2}$]
P_{flow}	Pressure upstream of flow meter [$ML^{-1}\ T^{-2}$]
P_{inlet}	Inlet pressure at test section [$ML^{-1}\ T^{-2}$]
$\dot{q}$	Volumetric flow rate measured by flow meter [L^3T^{-1}]
R	Gas constant for air [$L^2\ T^{-2}K^{-1}$]
RANS	Reynolds Averaged Navier Stokes
Re	Reynolds number
SGS	Subgrid scale
S_{ij}	Rate of strain tensor
St	Strouhal number
T	Static temperature [K]
T_{exit}	Exit temperature at test section [K]
T_{flow}	Pressure upstream of flow meter [K]
T_{inlet}	Inlet temperature at test section [K]

T_t	Stagnation temperature [K]
$\boldsymbol{u}$	Velocity vector representing all three components of velocity
$\bar{\boldsymbol{u}}$	Resolved scales of velocity vector representing all three components of velocity
$\boldsymbol{u}'$	Subgrid scale velocity vector representing all three components of velocity
U	Bulk flow circumferential velocity [L/T]
U_m	Axial mean velocity relative to the surface [L/T]
V	Axial velocity in the X direction [L/T]
W_{pl}	Plate width or channel width [L]
$\boldsymbol{x}$	Distance vector
X	Horizontal coordinate [L]
Y	Vertical coordinate [L]

TABLE OF CONTENTS

Page

LIST OF FIGURES

Page

Page

Page

Page

Page

1. INTRODUCTION

1.1 Introduction to annular and hole-pattern seals

Seals are known to be one of the most important components of a turbomachine owing to their ability to prevent leakage between the stages of a machine and also their contribution to its stability. With the increased need for better performance and more efficient turbomachines in the industry, it has become essential to study the physical behavior of seals as well and determine their precise impact on the behavior of the system. There are a wide variety of seals that can be used in a machine ranging from static seals (such as gaskets and O-rings, which are in contact with stationary surfaces) to dynamic seals (such as annular seals which are not in contact with sliding or rotating surfaces).

The choice of the sealing mechanism is entirely dependent on the application and is the result of careful consideration of many factors such as the acceptable amount of leakage between parts, cost and the stability of the system. Annular seals are chosen where a very tight seal is not required and also has the advantage of being simple in construction and cheap. Labyrinth seals on the other hand, can provide a good seal but tend to cause issues with the rotordynamic stability of the system. Honeycomb seals (Fig.1) are therefore seen as a viable alternative in cases where both the leakage characteristics and the stability of the system are of importance. The honeycomb seal was originally introduced in the 1960s as a replacement for aluminum labyrinth seals

and research from the late nineties [4, 5, 6] shows that these seals were able to provide stability in otherwise unstable systems

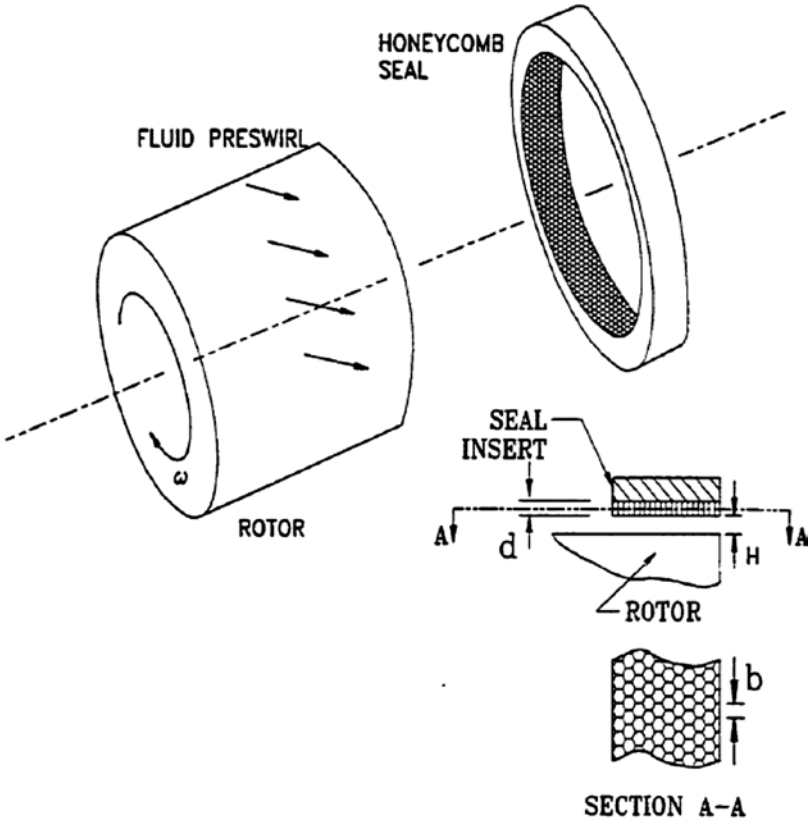

Figure 1 – A honeycomb seal around a smooth rotor [3]

Though honeycomb seals were able to provide satisfactory leakage and stability characteristics, the complex manufacturing of these seals and the rub related shaft

damage that is prevalent in use produce significant disadvantages as well. Hole-pattern (HP) seals were thus developed as an alternative. These seals are geometrically similar to honeycomb seals, the main difference being that they are manufactured with circular holes instead of hexagonal as shown in Fig. 2. Yu and Childs [7] compared three hole-pattern damper seals with a honeycomb seal. Their results show that hole-pattern seals generally provided a high effective damping and the overall performance of honeycomb and hole-pattern seals is comparable, showing that they can replace honeycomb seals for most applications.

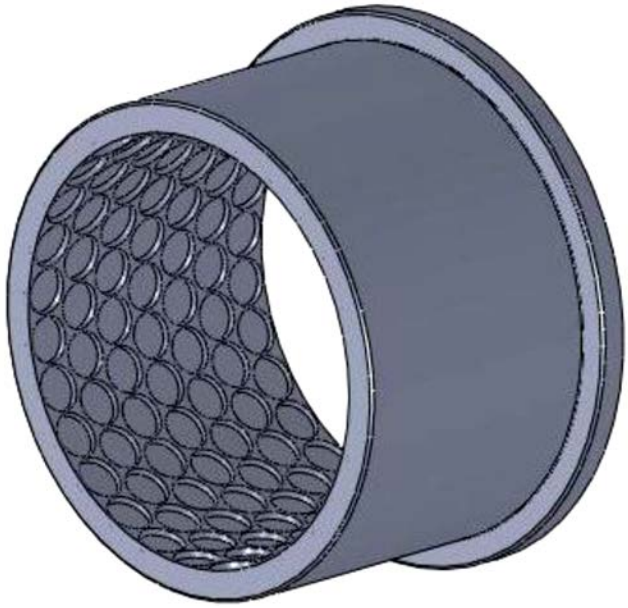

Figure 2 – A hole-pattern seal [1]

1.2 Importance of determining friction factor for leakage and rotordynamic studies

The friction factor has been an important subject of study in engineering applications since the landmark paper by Moody [8] that discussed the prediction of friction factors for circular pipes. Moody proposed the friction factor as a function of Reynolds number and surface roughness. For increasing Reynolds number, as per the Moody diagram, the friction factor decreases asymptotically in the turbulent regime; however, this does not hold for flow between closely spaced surfaces. A review of current literature shows that there is little information on friction factor data for closely spaced parallel plates and there is no analytical expression for its prediction.

With regard to honeycomb seals, a two-control-volume method using a bulk flow theory was proposed by Ha [3] which allowed for the determination of the rotordynamic coefficients of the seal. In applying this numerical solution from the governing equations, a perturbation of the variables pressure P, local clearance H, axial velocity V and circumferential velocity U is employed. The resulting equations are separated into zeroth and first order equations. The leakage of the seal is then predicted using the zeroth order equations for which the friction factor is needed as an input. The first order equations are solved to find the dynamic coefficients but they require partial derivatives of the friction factor with respect to the perturbation variables as inputs to define shear stresses at the boundaries. In order to carry out these computations it is therefore seen that the determination of the friction factor is necessary.

Though a range of studies have been carried out to determine and model the friction factor [3, 7, 8, and 9], recent tests using hole-pattern seals showed a peculiar

trend in the friction factor variation. It was observed that that as the pressure drop across the parallel plates was increased, there was a sudden decrease in the flow rate at a certain Reynolds number. This trend was mirrored by the sudden increase in friction factor at the same Reynolds number, and was seen as cause for concern since it could have serious effects on the rotordynamic stability of the system. Although it was postulated that this phenomenon was the result of flow choking at an upstream control valve [1] and was eliminated by employing two upstream control valves in series, the present author believes that it could be related to the mechanics of the flow itself. Cavity flows in literature that have reported such large changes in the friction factor have shown underlying changes in instability modes and the present study is an attempt to analyze and detect any presence of the same.

2. OBJECTIVES

This work will focus on studying the physics of the flow through a hole-pattern seal and attempt to further analyze the reason for the friction factor upset phenomenon. The geometry of the seal under review is the same as that used by Asirvatham [1] and the plate used along with its dimensions are shown in Fig.3. As seen here, the diameter of the holes is 3.175mm, the depth is 0.9mm and the clearance between the HP plate and the smooth plate is 0.254mm.

Results from previous studies [3] indicate that the distinct variation in the friction factor at a certain Reynolds number could be related to the presence of a flow instability in the seal. In order to test this hypothesis, the experiment will be re-run with using the same plates and parameters as Asirvatham [1]. The purpose of this part of the study would be to replicate the 'upset' phenomenon seen and also obtain high resolution pressure fluctuation data which is currently unavailable. Analyzing these spectra would allow determine if there is a change in the flow behavior, indicating a change in instability modes and help determine further investigation methods.

In order to study the flow more closely, a simplified geometry of the seal will also be examined, which, at the first principle is flow over a cavity with a top boundary to represent the clearance. A detailed numerical analysis will be carried out for this geometry using a range of CFD simulations in ANSYS Fluent. In order to determine the modeling technique that is able to capture the flow instabilities and also be

computationally efficient, Large Eddy Simulations (LES) will first be carried out with cavity flows that are known to have instabilities.

An extensive amount of work has been done on open cavity flows (without a top boundary) and it has been seen that flow over a cavity can lead to one of three kinds of instabilities –

1. Shear layer instability – where small disturbances in the free shear layer over the cavity are amplified owing to a Kelvin Helmholtz instability. Further interactions with the trailing edge of the cavity results these disturbances having an upstream influence thus causing a 'feedback- loop' type effect
2. Wake mode instability – where large structures (whose size is comparable to the dimensions of the cavity itself) are shed from the upstream lip of the cavity and behave like the flow behind a bluff body
3. Normal mode resonance – is characterized by a compression wave in the cavity, similar to that in a Helmholtz resonator.

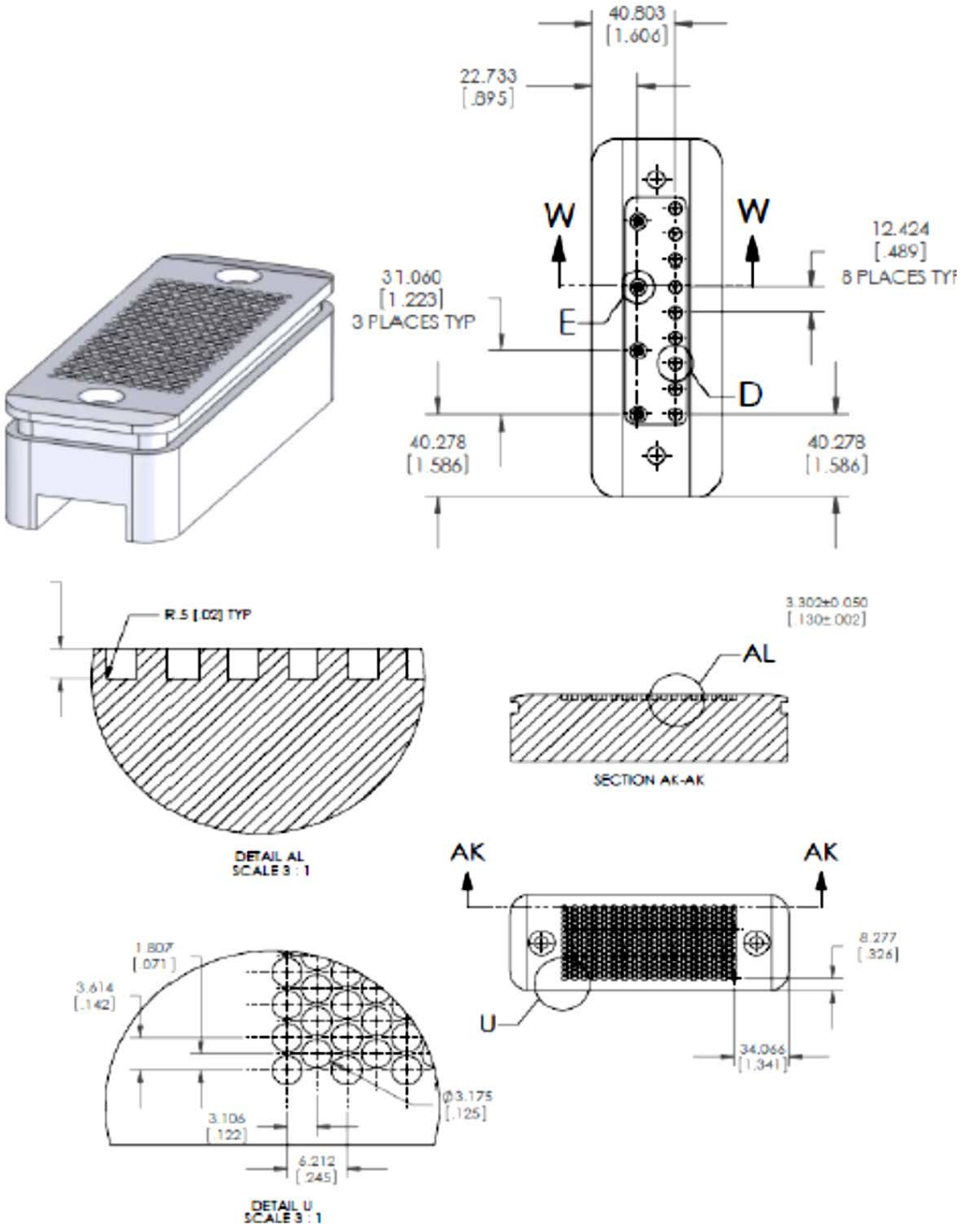

Figure 3 – Geometry of hole-patterned plate used by Asirvatham [1]

The friction factor upset can be related to the occurrence of one or more of these modes or even a combination of them. The initial objective is therefore to determine if LES can predict the occurrence of these instabilities since most related numerical studies have used Direct Numerical Simulations (DNS) which is computationally more intensive.

Once a method of simulation is determined, the current geometry will be modeled using boundary conditions from Asirvatham [1] and corresponding mass flow rates and friction factor will be calculated. These results will then be compared to the experimental values for validation.

3. LITERATURE REVIEW

3.1 Experimental studies related to friction factor calculation

Though the work done by Moody [8] was instrumental, as mentioned earlier, there has been little work done in terms of studying the friction factor in closely spaced parallel plates (i.e. channel flow). The work done by Ha [9] was preceded by a study by Elrod [11] who attempted to model the friction factor of honeycomb seals with a smooth rotor and honeycomb stator. This model was able to predict static and stability characteristics of the seal better than other models present at the time but still was unable to predict the direct stiffness which is an important component of the rotordynamic analysis of the seal.

Ha [9] was one of the first investigators to work with the flat plate tester in its current configuration and his base results showed that the honeycomb surfaces gave larger friction factor than smooth surfaces. Most of his test cases show a constant or slightly varying trend of the friction factor with change in Reynolds number but around 30% of the cases showed a friction factor jump when testing opposing honeycomb surfaces. The occurrence of the jump was also accompanied by high pressure oscillations which were found to be the result of a normal mode resonance which resulted in large scale coherent flow fluctuation in resonance with the Helmholtz frequency [3].

The cases that did not show the jump, on the other hand, contained the normal mode resonance and a feedback mode resonance - it was concluded that the presence of this feedback mode interfered with the normal mode such that the normal mode coherent structure did not attain amplitudes that would trigger non-linear effects. Fig. 4 shows the occurrence of the jump as well as the frequency spectra for the cases with and without the jump, showing the difference in dominant modes present.

Related studies were also carried out by Thomas [12] and Nava [13] who used a different flat plate tester with water as the working medium. Their results showed that the friction factor, in general, increased with increasing clearance between the plates and also that there was a clearance (referred to a plateau clearance) beyond which the friction factor does not increase. The same results were also confirmed by Childs and Fayolle [14] for hole-pattern seals using a liquid medium. These studies suggest that fluid compressibility is an important factor for the existence of the friction factor jump.

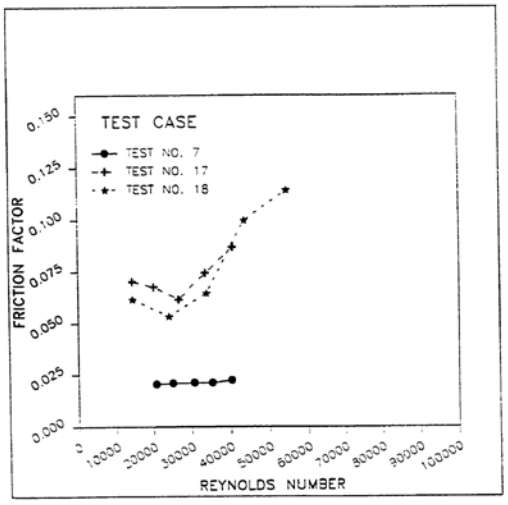

(a)

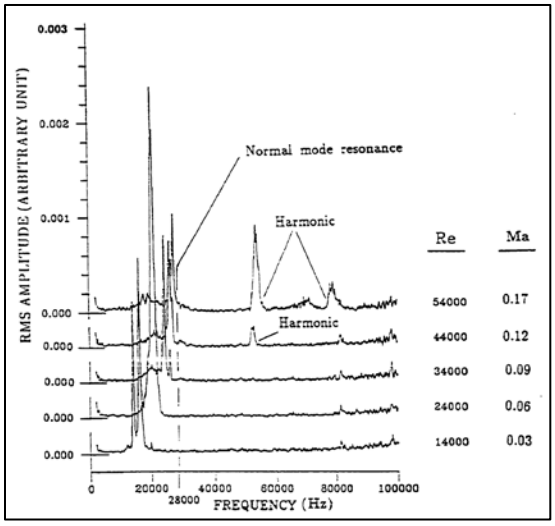

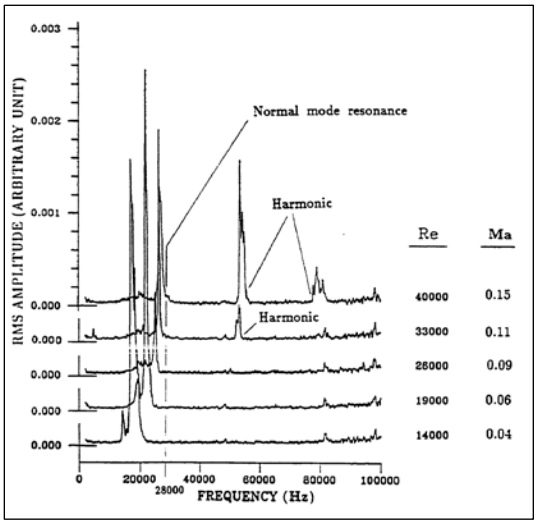

(b) **(c)**

Figure 4(a) – Variation of friction factor with Reynolds number showing the jump

(b), (c) – Frequency spectra for cases with and without the jump [2]

3.2 Review of work on flow instabilities

Since an early analysis of previous experimental data [1, 2] of the friction factor jump indicates an instability related phenomenon, it is necessary to study and understand the types of instabilities that can occur in the seal. The hole-pattern can be studied more closely by analyzing a simplified model of the seal and looking at a single hole or cavity. Taking a two dimensional section, this simplifies the study to the flow over a cavity with a top boundary representing the distance between the plates.

Cavity instabilities have been the subject of study for the last half century and their complexity derives from the many processes such as boundary layer separation, shear layer instability and acoustic radiation that affect the flow. Most of these processes are correlated making it difficult to identify the exact nature and source in these flow mechanisms [15]. These instabilities are however linked to the change in the total drag and generation of flow-induced oscillations which affect the stability of the system. This makes it essential to understand these flows thoroughly and determine their behavior in the system.

Of all the organized instabilities, based on seal geometry, the shear layer and the wake mode are the only ones that may be applicable for the present case (Helmholtz instabilities are seen in deeper cavities, usually with a neck at the entrance region). From the early work of Rossiter [16], cavity oscillations in compressible flow are typically described as a flow-acoustic resonance mechanism. This trend was characterized by small instabilities in the shear layer, which interact with the downstream corner of the cavity and generate acoustic waves; these waves propagate

back upstream and create new disturbances in the shear layer. For incompressible flow, this upstream influence is felt instantaneously while there is an acoustic delay for compressible flow. Resonance occurs at a specific frequency owing to the reinforcement of disturbances and this type of instability is called a shear-layer (or Rossiter) mode. Fig. 5 shows a schematic of this instability.

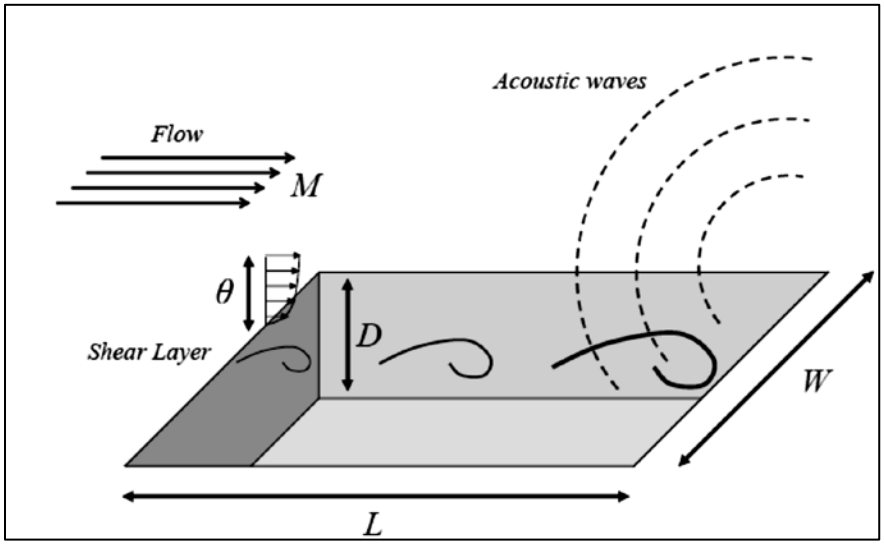

Figure 5 – Schematic of shear layer instability in an open cavity [17]

In addition to identifying the mechanism of the instability, Rossiter also developed a semi-empirical formula to predict the resonant frequencies for flow over a cavity without an opposing wall. This was done by carrying out an extensive range of

tests on two-dimensional rectangular cavities of different length to depth ratios and at different Mach numbers.

The relation obtained was –

$$St_n = \frac{f_n L}{U} = \frac{n-\alpha}{M+\frac{1}{\kappa}} \qquad n = 1,2,3, \ldots. \tag{1}$$

where St_n is the Strouhal number corresponding to the n –th mode frequency (f_n). The empirical constants κ and α correspond to the average convection speed of the vortical disturbances in the shear layer and phase delay (usually the values of $\frac{1}{\kappa}$ = 1.75 and α = 0.25 are used). Though data from a large number of experiments show agreement with the above equation, a significant amount of scatter has been seen owing to the discrepancies between experimental conditions (mainly different *L/D, L/*θ_0*,* Re_θvalues – where θ_0 is the momentum thickness of the boundary layer at the upstream cavity edge) [17]. Also, this equation does not indicate whether self-sustained oscillations do occur and if they do, which modes are present and dominant.

The other instability mechanism seen in cavity flow was that observed in an incompressible flow experiment by Gharib and Roshko [18]. They observed a significant change in the behavior of the cavity oscillation when the ratio of the cavity length relative to the upstream boundary layer momentum thickness was increased. It was seen that the flow was characterized by large-scale vortex shedding from that cavity leading edge (similar to that behind a bluff body) and was classified as a 'wake mode'. As the large vortex forms at the leading edge, free stream fluid enters in the

cavity and impinges on the bottom; this is followed by the vortex being shed from the leading edge and ejected from the cavity, leading to an increase in drag.

This mode was also successfully replicated in many two-dimensional numerical simulations [19, 20] but is hard to detect experimentally. Shieh and Morris [21] also showed that two dimensional cavities in the wake mode could return to a shear-layer mode when three-dimensional disturbances are present in the incoming boundary layer. Work by Suponitsky et al. [22] also showed that the development of a three-dimensional flow field, generated by random inflow disturbance into a two-dimensional cavity oscillating in wake mode, led to the transition to shear layer mode, regardless of the amplitude and shape of the inflow disturbances. These studies helped determine the course of action with regard to the type of simulations to be performed and the important parameters to be monitored.

4. METHODOLOGY

The current study will focus on closely studying the flow through the flat plate tester by using two methods –

(a) Re-testing the plates where the jump phenomenon was seen earlier using higher frequency pressure fluctuation measurements.

(b) Simulating the flow through the parallel plates using LES

4.1 Experimental analysis using the flat plate test rig

The initial parts of the project will involve re-taking the data for the flat plate tested by Asirvatham [1]. A simplified schematic of the flow loop (that is rated for up to 104 bars) is shown in Fig. 6 and a detailed view of the flat plate tester itself is shown in Fig.7. As the figure indicates, there are two flat plates that have distinctly different surfaces – the test plate is the one with the hole-pattern on it and the smooth plate is the one that acts as the opposing surface and forms the clearance required. In addition to the flowmeter shown in the loop, the setup also has the ability to take a series of pressure measurements; the smooth plate used has two pressure transducers that monitor the pressure at the inlet and exit of the assembly while the hole plate has nine transducers along its length that record the static pressure variation along the plate length.

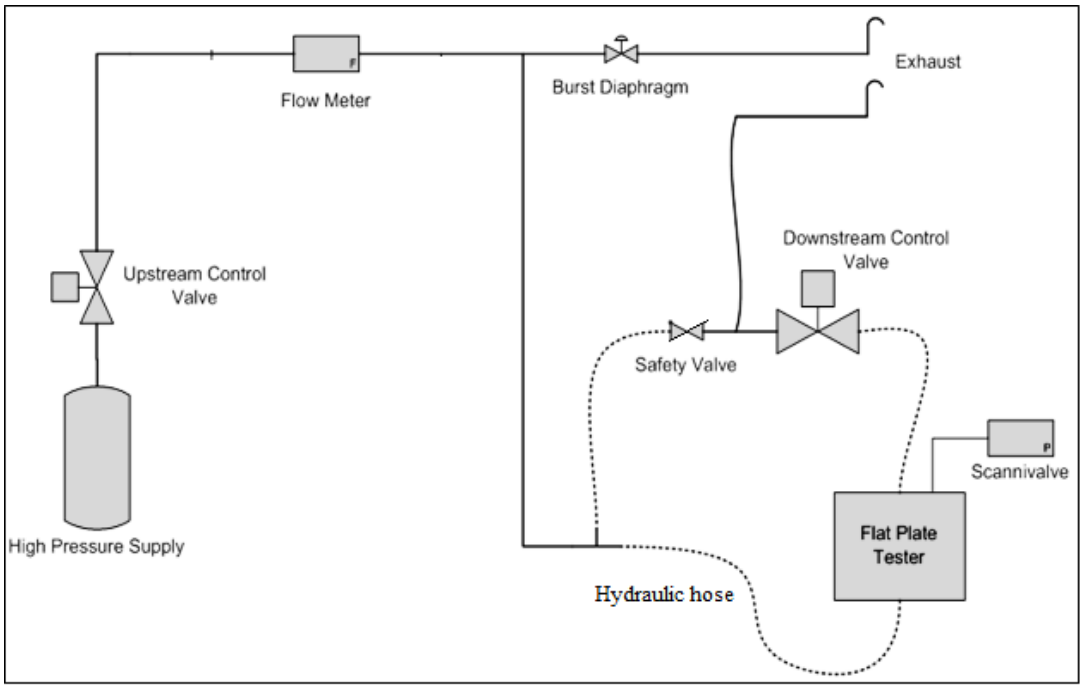

Figure 6 – Flow loop for flat plate test rig

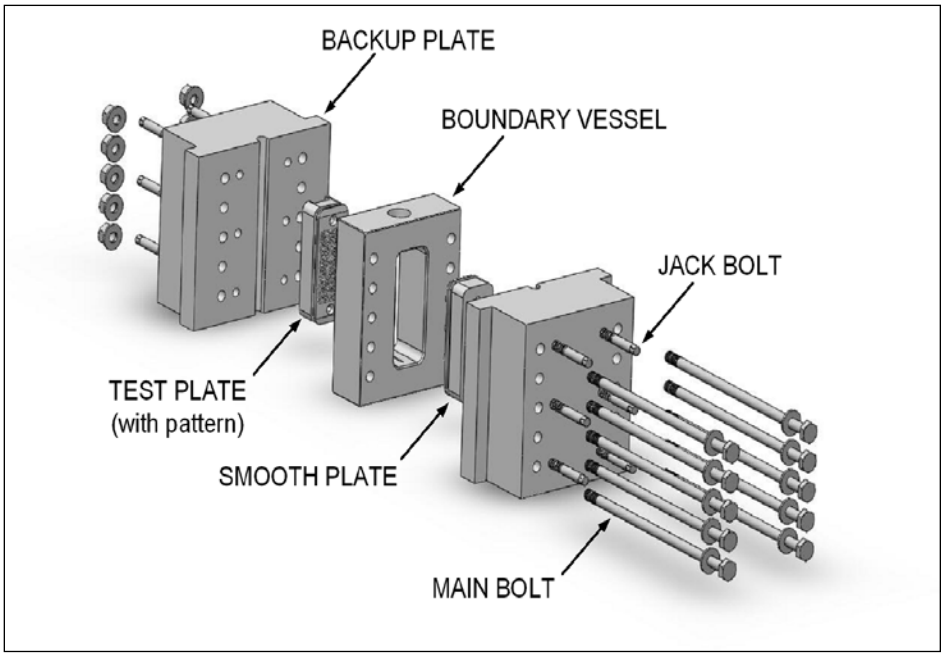

Figure 7 – Detailed view of the flat plate tester [2]

Along with the static pressure, the plates also have eight dynamic pressure probes (four on each plate) which are capable of high frequency pressure fluctuation data. It was seen by Rowley [19] that the predicted instabilities could show dominant frequencies of the order 100,000 Hz; however owing to the sampling rate of the A/D system used by Asirvatham [1] and Kheireddin [2], the highest frequency that could be detected was limited to 50,000 Hz and hence the presence or absence of these instabilities cannot be confirmed from existing data. Since the frequency response of the transducers makes them capable of detecting frequencies up to 250 kHz, a higher sampling rate can be obtained from the same setup by using a different A/D converter. It is proposed to use a Tektronix oscilloscope for this purpose since this oscilloscope allows sampling rates up to 1 giga samples per second.

This setup will therefore allow acquisition of pressure fluctuations that will determine the validity of the CFD data and help provide a deterministic reason for the occurrence of the friction factor jump.

4.2 Numerical study of flow through parallel plates

The later parts of the work will involve simulating the flow through two open cavities of different *L/D* ratios to determine if the modeling technique used captures the different modes that would be seen for these cavities as according to Rowely [19]. To do this, the problem setup used is as shown in Fig.8. Since this reference and most others advocate the use of DNS to detect these instabilities, this first step will help

establish a method of simulation that is less computationally expensive and also less time consuming.

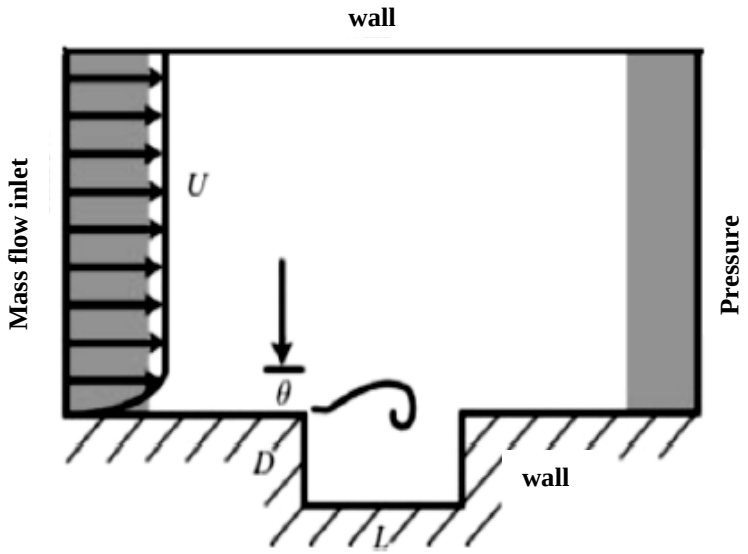

Figure 8 – Problem setup to check for instabilities in an open cavity [19]

To carry out these simulations, the domain shown in Fig.8 will be meshed with structured quadrilateral cells. The cells will be grouped closely at the boundaries along the top of the cavity so as to ensure the boundary layer and the relevant flow features here are accurately captured. Though the number of cells would be around 3,000,000 a coarse representative mesh is shown in Fig.9 for an *L/D* ratio of 4 to indicate the

relative density of the grid in different parts of the domain. In addition to the normal boundary for the domain (shown at 3.5L = 14D in Fig.9), the upstream boundary (or inflow) is chosen at 4.3D to allow the development of the boundary layer. Also, the downstream boundary is chosen at 9.2D in order to ensure that it does not interfere with the flow close to the downstream edge of the cavity. An identical domain is created for a cavity with an L/D ratio of 2 in order to observe the presence of both types of instabilities (in accordance with [19]). For the dimensions of this cavity, since the aforementioned reference restricted the description of the domain in terms of the depth alone, the seminal work of Krishnamurty [23] was referred to (since it was used as the benchmark for Rowley's study [19]) and the depth of the cavities was set to 0.05 in. The other dimensions were calculated accordingly as accounted earlier.

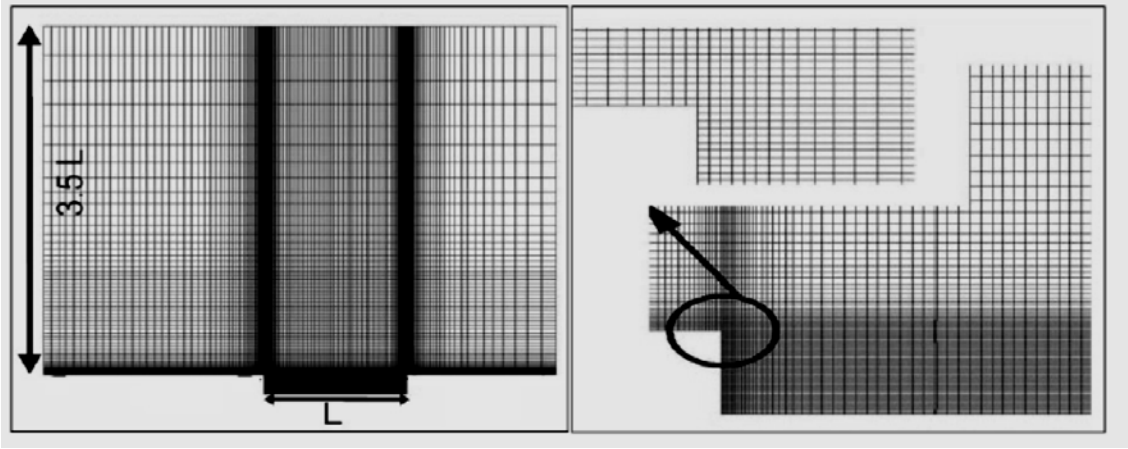

Figure 9 – Representative mesh for domain shown in Fig.8

The simulation will be run using ANSYS Fluent 12.0.16 with bounded central order differencing for the spatial derivatives of the governing equations and a second order implicit scheme for the time derivatives. The subgrid-scale stresses will be modeled using the Smagorinsky-Lilly model with C_S , the Smagorinsky constant set to 0.1. The main advantages of using this subgrid scale model are its manageability and its computational stability, making it an appropriate choice for most engineering applications [24]. In addition to the parameters mentioned above, the time step size during transient simulations will be limited to a fairly small step size of the order of 1e-8 seconds in order to ensure that all relevant flow structures are well captured.

Once a suitable method of simulation has been determined, the next step will involve the construction of a suitable model for the setup in question. To understand the behavior of the flow, the model will be reduced to a simple two dimensional formulation keeping the dimensions as according to the pattern tested by Asirvatham[1]. This type of formulation will also help with the objective of investigating the flow thoroughly without having to take on the computational expense of simulating the entire test surface. Another reason for simulating one cavity relates to the fact that earlier research [25] has shown that in addition of neighboring cavities does not affect the existence or the value of the dominant frequency of the system. The addition of more cavities would lead to the detection of higher harmonics but the basic nature of the instability is unaltered. A representative grid for this set of simulations along with the corresponding dimensions is shown in Fig.10.

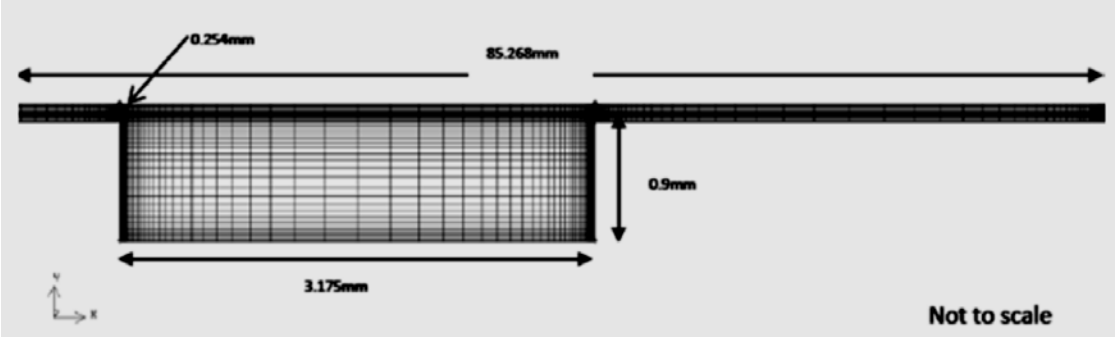

Figure 10 – Representative mesh for LES simulations based on geometry from [1]

5. THEORY OF FLAT PLATE TESTING AND DESCRIPTION OF TEST RIG

5.1. Theory of flow through narrow channels and concept of flat plate testing

The test section of the flat plate rig represents a rectangular channel that can be modeled by the control volume shown in Fig. 11. This derivation has been obtained from John and Keith [26] and Dr. G. Morrison's class notes [27]. The following section details in the derivation of the friction factor based on the Fanno line flow. The assumptions made for this analysis are –

(a) The flow is assumed to be one dimensional since the width of the plate is much larger than the clearance

(b) Air is assumed to behave as an ideal gas with constant specific heats

(c) Area change effects, body forces and work across the control surface are small enough to be neglected

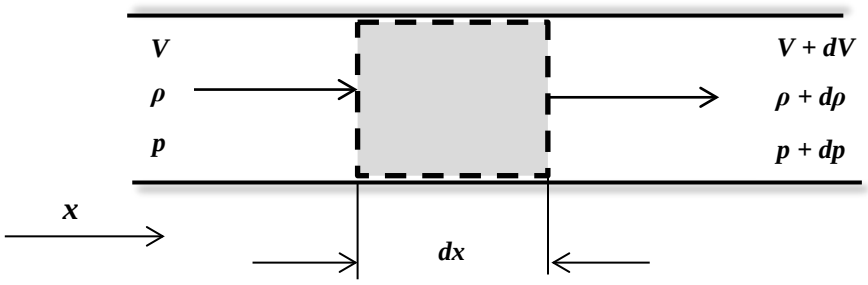

Figure 11 – Control volume for adiabatic, constant area channel flow

The control volume for the derivation is shown in Fig. 9. The momentum equation in the *x* direction for this control volume gives –

$$-\tau_f A_s - AdP = \rho AVdV \tag{2}$$

where τ_f is the wall shear stress, A_s is the surface over which the frictional forces act, A is the cross-sectional area of the channel and V is the axial velocity in the x direction.

Defining the hydraulic diameter as –

$$D_h = \frac{Cross\ \ sectional\ \ area}{wetted\ \ perimeter} \tag{3}$$

Since the channel is rectangular –

$$D_h = \frac{W_{pl} C_{pl}}{2(W_{pl}+C_{pl})} \tag{4}$$

where W_{pl} and C_{pl} are the width and height of the rectangular channel respectively.

Applying assumption (a), the hydraulic diameter is reduced to –

$$D_h = 2\ C_{pl} \tag{5}$$

Defining the Fanning friction factor as –

$$f_f = \frac{\tau_f}{0.5\ \rho V^2} \tag{6}$$

Using this in Eq. (16) gives –

$$-dP - \frac{1}{2}\rho V^2 f_f \frac{dx}{D_h} = \rho V dV \tag{7}$$

Applying the definition of Mach number M as $M = \frac{V}{\sqrt{\gamma RT}}$ (where γ is the ratio of specific heats and R is the gas constant for air) and using the relation between the static and stagnation temperatures as –

$$T_t = T\left(1 + \frac{\gamma-1}{2}\ M^2\right) \tag{8}$$

Using the equation for the conservation of mass in conjunction with the ideal gas law and the definitions of M and T_t , the following relation is obtained for M –

$$M = \left(\frac{-1+\sqrt{1+2(\gamma-1)\left(\frac{\dot{m}}{PA}\right)^2\left(\frac{RT_t}{\gamma}\right)}}{(\gamma-1)} \right)^{1/2} \tag{9}$$

where $\dot{m}$ is the mass flow rate through the test section. This equation allows for the calculation of M from $\dot{m}$, P and T_t which can be measured and R , γ and A which are known quantities.

Further, using the equations above as seen from Asirvatham [5] -

$$f_f = \frac{C_{pl}(1-M^2)}{\gamma M^3\left(1+\frac{\gamma-1}{2}M^2\right)}\frac{dM}{dx} \tag{10}$$

$\frac{dM}{dx}$ can be calculated by curve fitting the Mach number along x and finding the local derivative of the curve. This allows for the calculation of the friction factor from the available Mach number data.

This theory is applied in the flat plate rig to experimentally determine friction factors for HP seals. The test configuration uses a roughened HP plate that represents the seal surface facing a smooth plate that represents the rotor surface [5]. Air flow between these two plates is through a clearance which represents the radial clearance in a seal. The friction factor is measured in the fully developed regime where the axial velocity can be assumed to be one-directional. Also, the Reynolds number for this case is defined as –

$$Re = \frac{\rho(2H)U_m}{\mu} \tag{11}$$

5.2. Description of the test rig

The objective of the flat plate test rig is to enable a relatively rapid determination of the friction factor for a range of surfaces. The test rig in question uses high pressure air as the working fluid and Fig. 6 shows a simplified schematic of the flow loop for the same. High pressure air that is compressed and stored at the Oran W. Nicks Low- Speed Wind Tunnel is delivered to the test rig that is located at the Turbomachinery Laboratory. The entire flow loop shown is rated for 104 bars, and the safety valve shown ensures that the pressure stays within the recommended limit [1]. The two other important valves are the downstream control valve that helps maintain the exit pressure and the upstream control valve that helps set the inlet pressure.

The flat plate tester itself consists of the test plates that are held in the boundary vessel by backup plates and the entire assembly is kept in place by main bolts as shown in Fig. 7. As the figure indicates, there are two flat plates that have distinctly different surfaces – the test plate is the one with the hole pattern on it and the smooth plate is the one that acts as the opposing surface and forms the clearance required. Both plates are made of 410 annealed stainless steel with very high yield strength in order to withstand stresses induced by high pressure air. They also have the same dimensions of 4.45 cm x 6.35 cm x 15.24 cm and have O-ring grooves around the periphery in order to prevent any leakage. Both plates also have two countersunk holes in order to allow for attachment to the backup plates. Fig. 12 (a) shows the basic construction of the smooth plate while Fig. 12(b) shows the same for the HP plate. Another important parameter in

the manufacture of HP plates is the ratio γ_A which is the ratio of the area occupied by the holes in the seal to the total inner surface area; for the plate under study, γ_A was 75.4%.

In addition to the features mentioned, the plates are also equipped with holes for the static and dynamic pressure transducers. As seen from Fig. 12, both plates have taps for four subminiature high frequency response pressure sensors located along their length; these sensors are mounted flush with the surface of the plate so as not to interfere with the flow. The smooth plate is responsible for the monitoring of the inlet and exit temperatures and pressures of the flow through the clearance and to this end, miniature holes drilled at the inlet and the exit of the exit sides of the plate are connected to thermocouples and pressure transducers which are connected to a bank of LED displays. The HP plate on the other hand is used to collect static pressure data from the nine additional pressure transducers located along its length and this information is sent to the DAQ system (details of which are accounted in later sections).

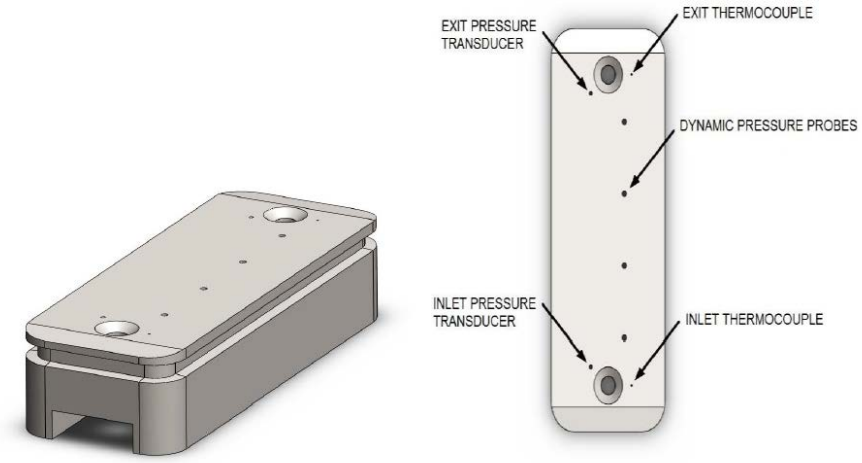

(a)

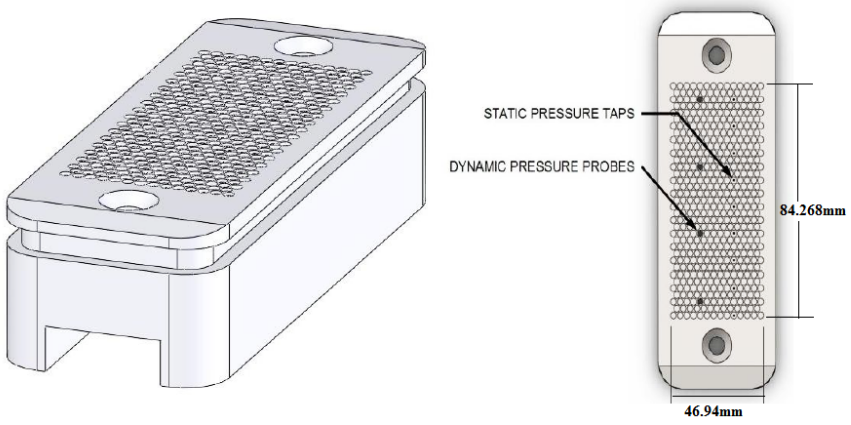

(b)

Figure 12(a) – A typical smooth plate with pressure tap and thermocouple locations, (b) – A typical hole patterned plate with pressure tap and thermocouple locations [1]

Another important part of the rig is the boundary vessel which is the rectangular vessel with a central 'window' that is located at the core of the assembly. This is the part where the two test plates come together and also where the inlet and exit for the air supply are located. Fig. 13 shows the boundary vessel with the smooth plate in place, showing the air passage.

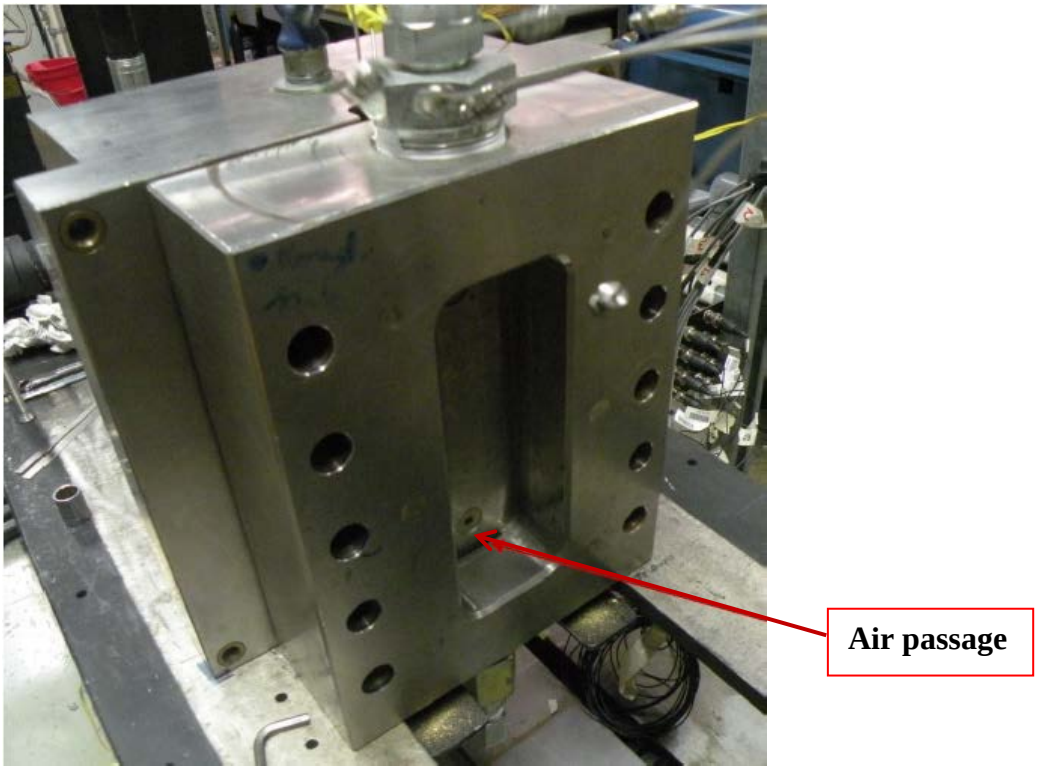

Figure 13 – Photograph of smooth plate and the boundary vessel showing the air passage

The boundary vessel is supported by two backup plates made of heavy blocks of 315 stainless steel which serve to support and keep the test plates in place. The clearance between plates is set by means of stainless steel shims which can be replaced to obtain different clearances. The entire assembly is pulled together by using 5/8 X 16 UNF carbon steel bolts while the test plates are rigidly bolted to the backup plates using flat head screws. Fig. 14 shows the plates and the boundary vessel before assembly while Fig. 15 shows a photograph of the assembled rig.

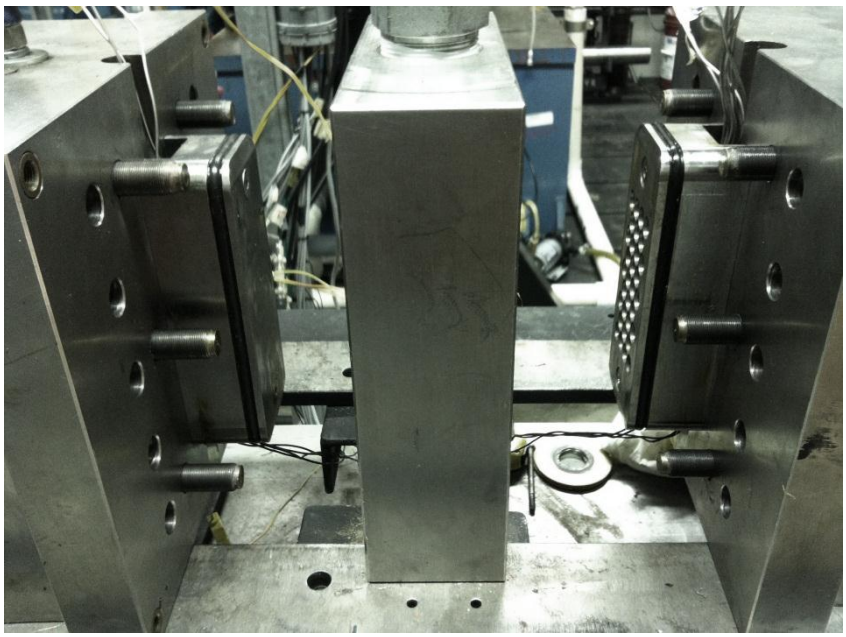

Figure 14 – Photograph of both plates and the boundary vessel before assembly

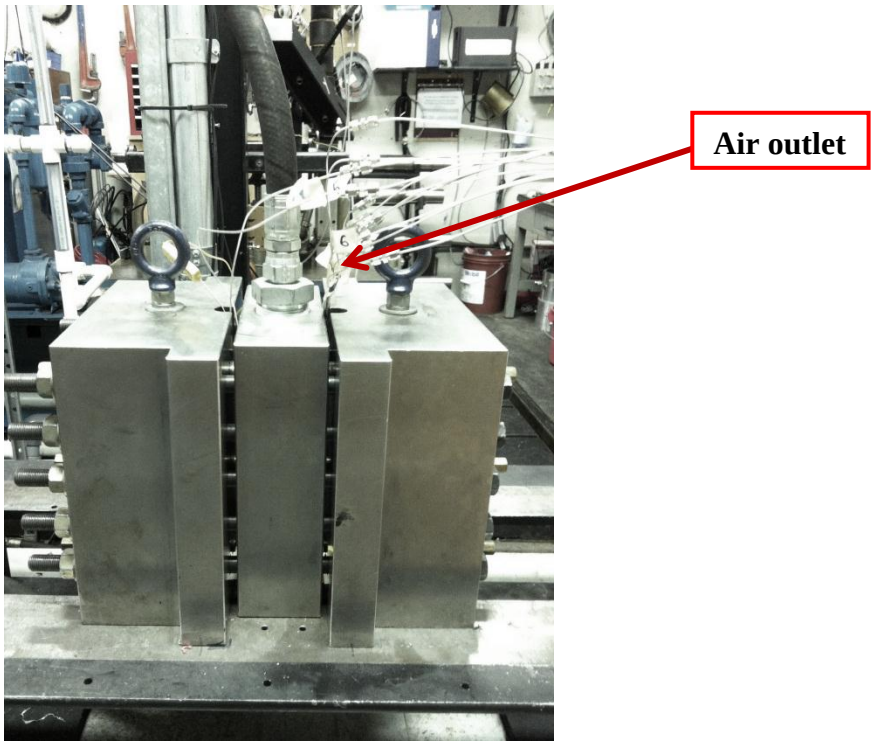

Figure 15 – Photograph of assembled setup showing air outlet

The next few paragraphs discuss the instrumentation of the rig in detail. The inlet and backpressure valves are both Fisher® D4 control valves which are electronically controlled by a potentiometer that sends a 4-20 mA signal. The next component in the flow loop is a Flow Technology® flow meter which has been calibrated at a pressure of 84 bar and a temperature of 295 °K. It is also connected to a digital readout which displays readings in acfm (actual cubic foot per minute) and has an accuracy of ± 0.25%. The flow rate digital display is further connected to a National Instruments® Data Acquisition (DAQ) Board and a LabVIEW program is used to collect the data.

The static pressure tubes connecting the probes along the test plate are made from stainless steel. The tubes are attached with extreme care to the back of the test plates via epoxy to insure that the tubes do not kink or bend. Stainless steel tubes and compression fittings are used to connect the static pressure probes to a Scanivalve® pressure scanner. This particular module has 16 ports that allow multiple-point measurements of the static pressures along the plates. It also has RAM, 16 bit A/D converter and a microprocessor that communicates with a PC through an Ethernet TCP/IP Protocol.

In addition to the static pressure measurements, dynamic pressure data was taken using PCB ® 105C22 transducers - four of which were mounted flush with the surface of the smooth plate and the remaining four were mounted flush with the bottom of the holes of the HP plate. These dynamic pressure sensors are connected to a dynamic DAQ through a BNC to SMB cables. This NI PCI 4472 DAQ board is also used to power these subminiature ICP pressure sensors. Since the sampling frequency of the sensors was limited due to the use of this DAQ, which is limited to a maximum sampling frequency of 102,400 samples per second, an oscilloscope with a higher sampling rate was added to the setup. This involved additional connections from the dynamic sensors on the smooth plate to a Tektronix® TDS 2004C oscilloscope which is capable of recording up to 1 giga samples/second. The oscilloscope interfaces with a computer by means of another LabVIEW code which is designed to record data for the duration of the run.

6. TESTING PROCEDURE, CALCULATION AND RESULTS FROM FLAT PLATE TEST RIG

This section of the work is referenced from Asirvatham [1] and Kheireddin [2] in order to ensure integrity of the results for comparison.

6.1 Testing procedure

The wind low-speed wind tunnel at the Oran W. Nicks facility employs two compressors to obtain high pressure air which is then stored in an air tank at the location. Once the pressure in the tank reaches 104 bar, the compressors are turned off. The flow loop showing the transfer of air from the wind tunnel facility to the Turbomachinery Laboratory is shown in Fig. 16. [28].

Each day of testing begins by verifying that all instrumentation is working properly. Before data acquisition, the entire system is checked for unwanted leakage by opening the inlet control valve and keeping the backpressure valve closed; once the pressure in the system reaches 84 bar, the inlet valve is closed, and the pressure in the system is monitored. If no detectable leaks are found, testing begins. To avoid malfunction of the flow meter, the inlet control valve is opened slowly while the backpressure valve is in the closed position.

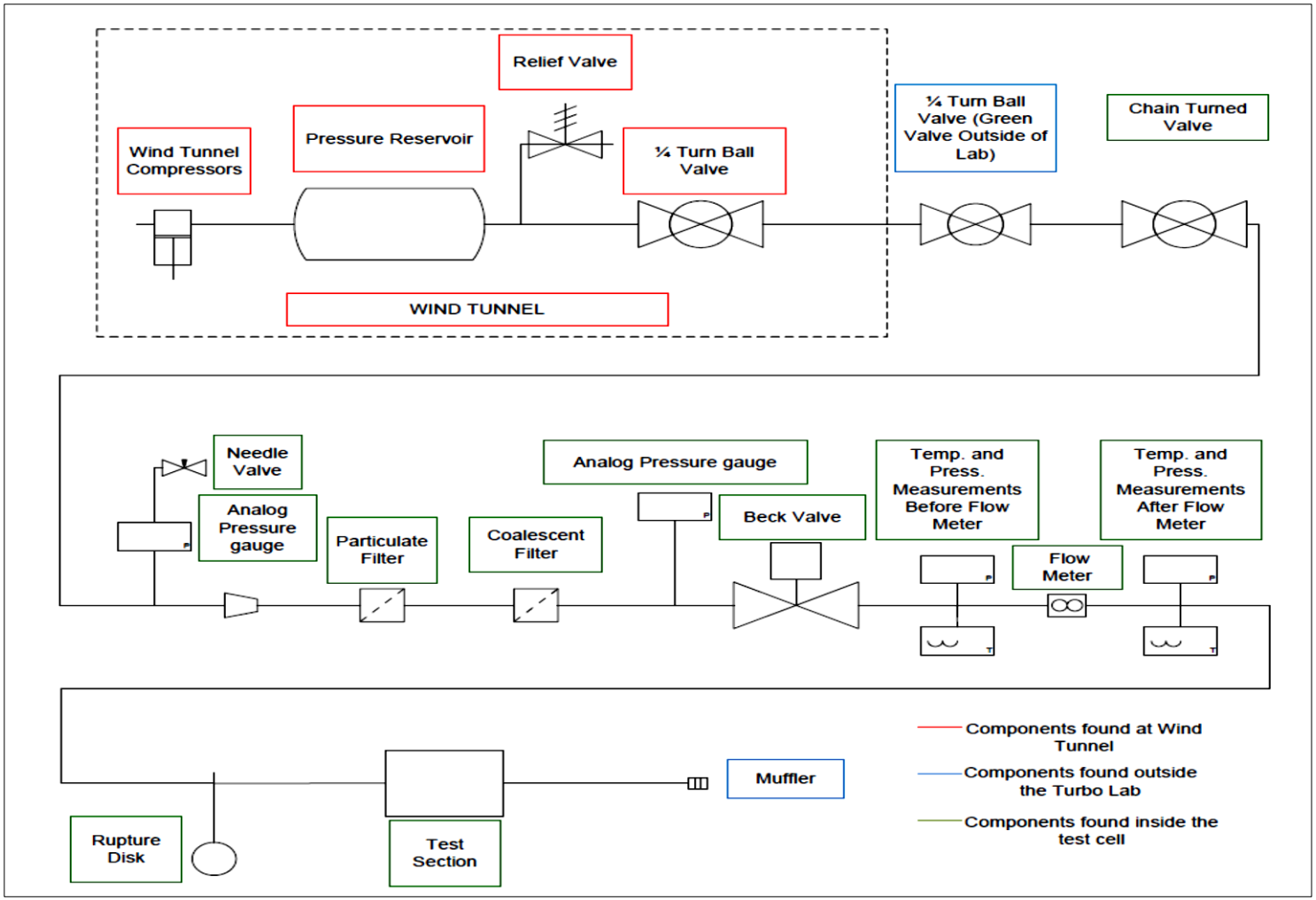

Figure 16 – Flow loop showing transfer of high pressure air to Turbomachinery Laboratory [28]

Once the entire system is pressurized to the desired pressure (this is achieved by opening the inlet valve an appropriate amount, based on the required pressure and the available tank pressure), the backpressure valve is slowly opened until a maximum pressure differential is established. Specified pressure drops are then achieved by closing the backpressure valve. Once steady state flow conditions are established, data is collected through a LabView program as detailed in Chapter 5. At the end of the test day, the flow meter is disconnected from the flow loop and flushed with denatured alcohol so as to remove any moisture that could cause erroneous readings. .

Static data comprising of pressure, temperature and flow rate are collected by the LabView program and this data is further reduced by an Excel code. Asirvatham [1] used a LabView program that is set up to acquire the time signal of the pressure oscillations detected by the dynamic pressure probes sampled at 100k Hz.

6.2 Calculations

Each test run includes the following data being measured –

(a) Volumetric flow rate as measured by the flow meter along with the pressure and temperature upstream of the flow meter, P_{flow} , T_{flow} .

(b) Inlet and exit pressures of the test section measured at the smooth plate, P_{inlet}, P_{exit}

(c) Inlet and exit stagnation temperatures of the test section measured at the smooth plate, T_{inlet}, T_{exit}

(d) Static pressure drop along the length of the HP plate at 9 locations, *P1,P2, P3,…P9*

(e) Dynamic pressure data measured at 4 locations at the smooth plate and 4 locations at the HP plate.

The above test results correspond to a particular plate with a specific C_{pl} for a set P_{inlet} and ΔP which in turn defines the *Re* (The difference between the terms 'pressure difference' and 'pressure ratio' being that they are the difference and ratio between the inlet and exit pressures respectively).

Density at the flow meter is calculated from a formula derived from the ideal-gas relation as –

$$\rho_{flow} = \frac{P_{flow}}{R * T_{flow}} \tag{12}$$

where P_{flow} (N/m^2) is the static pressure upstream of the flow meter, R is the specific gas constant (287 J/Kg/K) and T_{flow} (K) is the static temperature upstream of the flow meter. Although the temperature being measured using the thermocouple is the stagnation temperature, since the Mach number across the flow meter is of the order of 0.1, this can be approximated as the static temperature as well. Further, the mass flow rate is calculated as –

$$\dot{m} = \dot{q} * \rho_{flow} \tag{13}$$

where $\dot{q}$ is the volumetric flow rate measured by the flow meter (m^3/s).

The Reynolds number is calculated as -

$$Re = \frac{\rho\,(2H)U_m}{\mu} = \frac{2*\dot{m}}{C_{pl}*\,\mu} \tag{14}$$

where $\dot{m}$ is calculated as seen earlier (kg/s), C_{pl} is the clearance between plates where the flow goes through while μ is the absolute viscosity of air (Pa s).

Further calculations in the study relate to the calculation of the friction factor and Mach number. Assuming that the change in viscosity is negligible, the Reynolds number is constant along the flow path for a fixed ΔP . The friction factor, f_f then varies throughout the length of the plate and is calculated at all nine points of pressure measurement by the following method.

(a) Calculation of Mach number along the length of the plate

The Mach number, *M* is calculated at the inlet, exit and at the nine points along the plate length where the pressure is measured. This is done using the static pressure values that are measured and also the stagnation temperature T_t at these points. According to the Fanno flow assumptions, this stagnation temperature of the flow should remain constant since there is no heat transfer; however in practice, a small temperature drop (the maximum of which was measured to be 3 K) is seen as the flow reaches the exit. In order to account for this, an average of the inlet and exit temperatures is used as the stagnation temperature of the flow, hence maintaining the adiabatic flow assumption. Recalling Eq. (23), *M* is therefore calculated as –

$$M = \left(\frac{-1+\sqrt{1+2(\gamma-1)\left(\frac{\dot{m}}{PA}\right)^2\left(\frac{RT_t}{\gamma}\right)}}{(\gamma-1)} \right)^{1/2} \tag{15}$$

(b) Calculation of Mach number gradient and Fanning friction factor

The Mach number gradient dM/dx , along the length of the plate is necessary to calculate the friction factor f_f as according to Eq. (10) from Ch. 5 –

$$f_f = \frac{C_{pl}\,(1-M^2)}{\gamma M^3 (1+\frac{\gamma-1}{2}M^2)}\,\frac{dM}{dx} \tag{10}$$

Since the value of P is available at each of the 9 pressure taps, this is used to calculate dp which is further used to compute M and dM using the equation –

$$\frac{dp}{p} = -\frac{dM}{M}\left[\frac{1+(\gamma-1)M^2}{1+\frac{\gamma-1}{2}M^2}\right] \tag{16}$$

This equation is directly derived from the application of the Fanno flow principle and allows for the simultaneous determination of M and dM. These values are then used in the computation of dM/dx which is substituted into Eq. (10) to calculate the Fanning friction factor, f_f .

6.3 Friction factor upset as seen in earlier studies

The most recent occurrence of the upset phenomenon was seen by Asirvatham [1] who observed that the phenomenon was seen while increasing or decreasing ΔP during testing. His work details the existence of one of these cases- a plate with hole diameter, h_φ = 3.175mm, hole depth h_d = 0.9mm, $C_{pl}$of 0.254mm and an inlet pressure of 84 bar. This test was performed by starting at the maximum ΔP (i.e. the exit valve totally open) and closing the exit valve in steps until the minimum ΔP is established. Data is recorded at each step and Fig. 17 shows the variation of $\dot{m}$ with the ΔP as

obtained for this case. As seen here, there is a distinct jump in $\dot{m}$ at $\Delta P = 15\ bar$ which is reflected in Fig. 18 as a drop in f_f.

Based on these results, and an analysis of the data obtained, Asirvatham concluded that the abrupt changes were due to choking at an upstream control valve and reported that the problem had been eliminated by using two upstream valves, in series. The present author however differs from the view that this sudden variation was purely a result of the valve configuration and proposes that the phenomenon of the jump needs further examination. Based on the geometry and the flow conditions, the jump could be indicative of a change in the instability modes of the system as the fluid passes over the cavities of the plate. Placing two valves in series changes the nature of the turbulent flow entering the test section and therefore helped eliminate the unexpected jump.

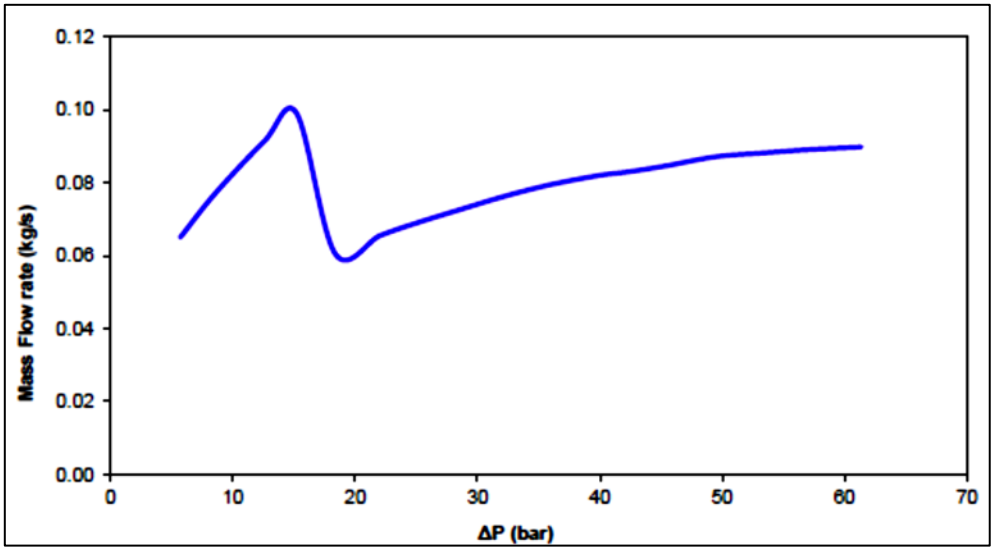

Figure 17 – Variation of $\dot{m}$ with ΔP showing the abrupt change in flow rate [1]

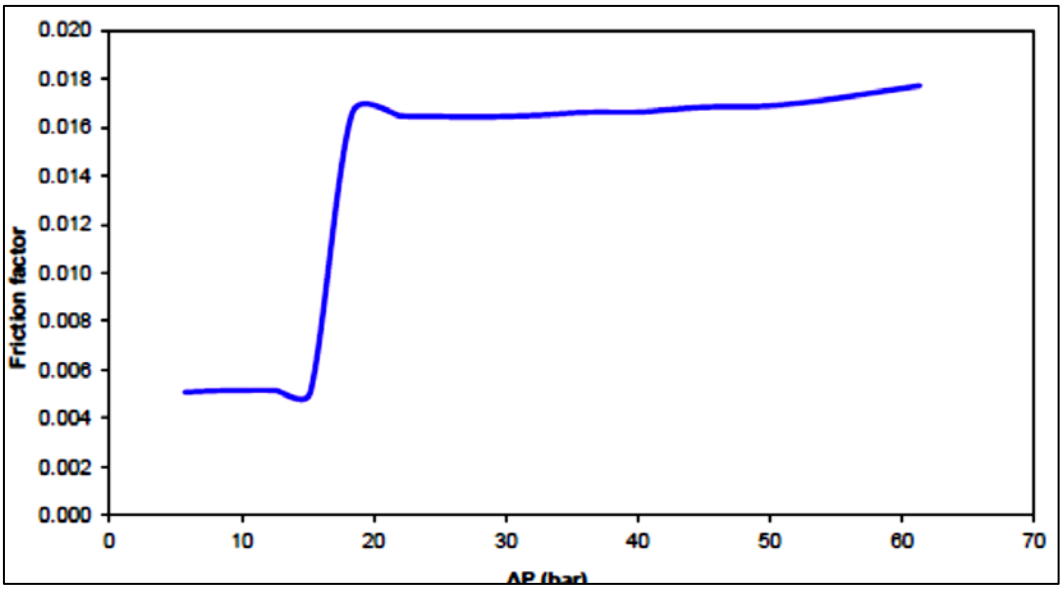

Figure 18 – Variation of f_f with ΔP showing the friction factor jump [1]

6.4 Analysis of friction factor upset as seen in current testing

In order to obtain a more extensive data set of the flow conditions at and before the occurrence of the jump, the flat plate rig was re-run with the same configuration and plates as that used by Asirvatham [1]. Since the occurrence of the jump was seen with a single valve alone, the additional valve upstream was removed. The only addition to the setup, as mentioned earlier was the oscilloscope, in order to allow for high frequency sampling of pressure fluctuations.

Fig. 19(a) shows the variation of mass flow rate with the ΔP as obtained for the case with a plate with h_{φ} = 3.175mm, h_d = 0.9mm, $C_{pl}$of 0.254mm and an inlet pressure of 84 bar.

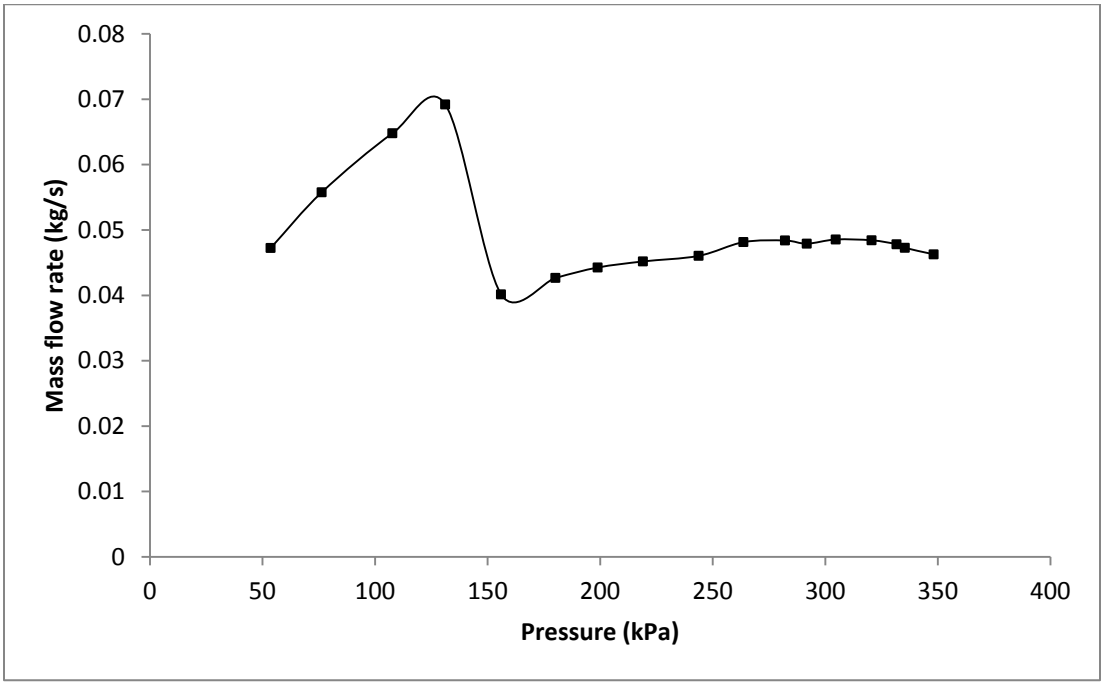

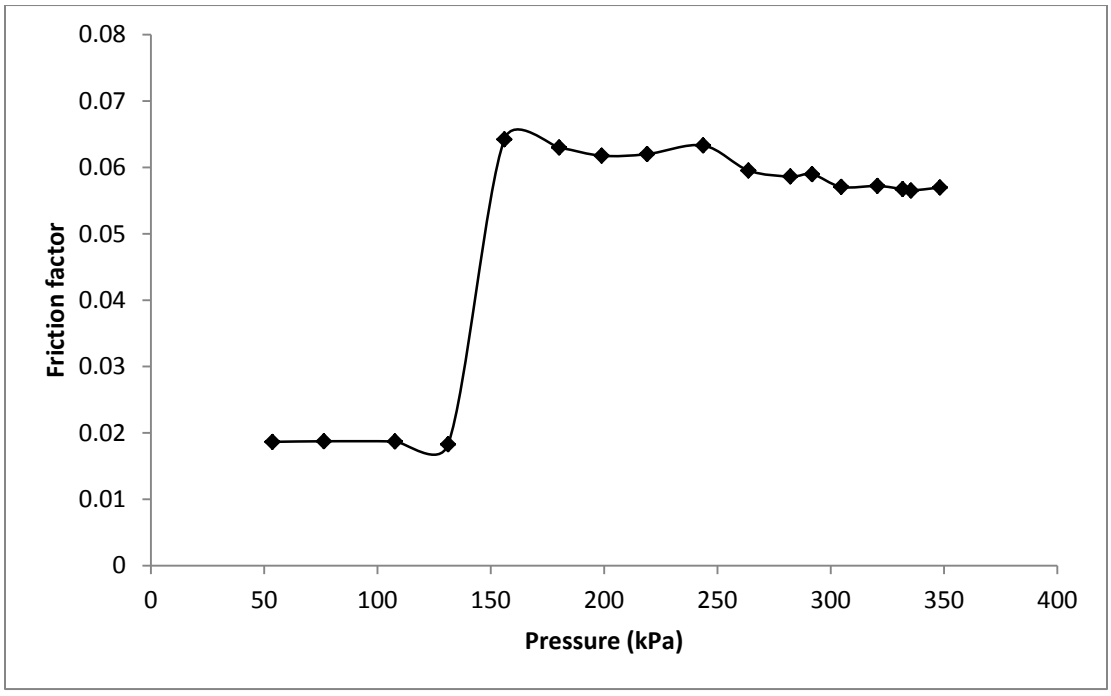

Figure 19 (a) – Variation of $\dot{m}$ with ΔP showing the abrupt change in flow rate, (c) - Variation of f_f with ΔP showing the friction factor jump

These measurements were obtained by continuously decreasing the ΔP over the required range. As seen here, the variation shows the distinct change in mass flow rate at a ΔP of around 155 kPa which is reminiscent of the trend seen by Asirvatham [1]. This variation is complemented by the trend of the friction factor as seen in Fig. 19(b). The plot shows that for a small change in pressure, there is a large change in the friction factor (the friction factor jumps to almost 3.5 times of the value recorded at the previous data point).

Fig. 20 shows the measured static pressure variation along the length of the plate for all the different Reynolds numbers (as defined by Eq. 28) for the same inlet pressure of 84 bar. The first and the last data points correspond to the inlet and the exit pressures measured at the smooth plate while the nine points along the length correspond to the nine pressure measurement points on the HP plate.

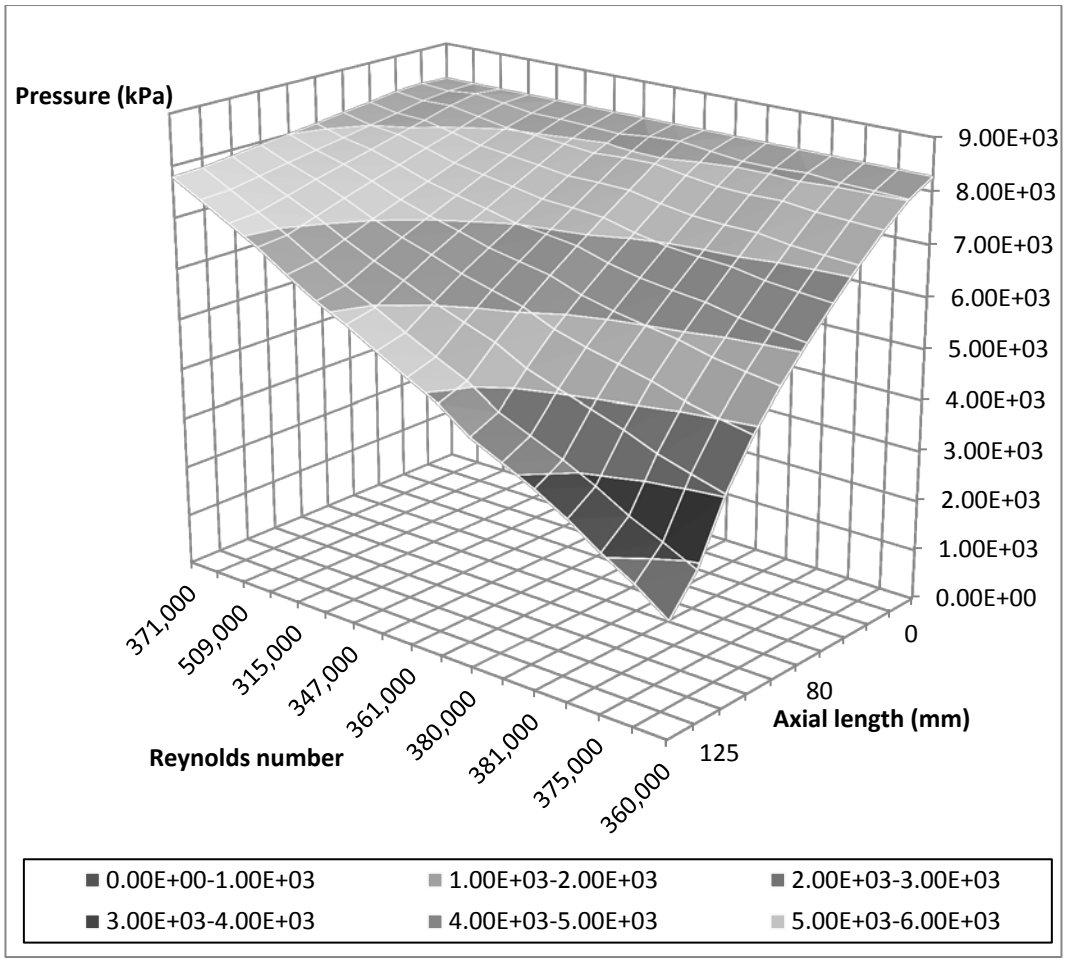

Figure 20 – Pressure drop along the length of the plate varying with the Re

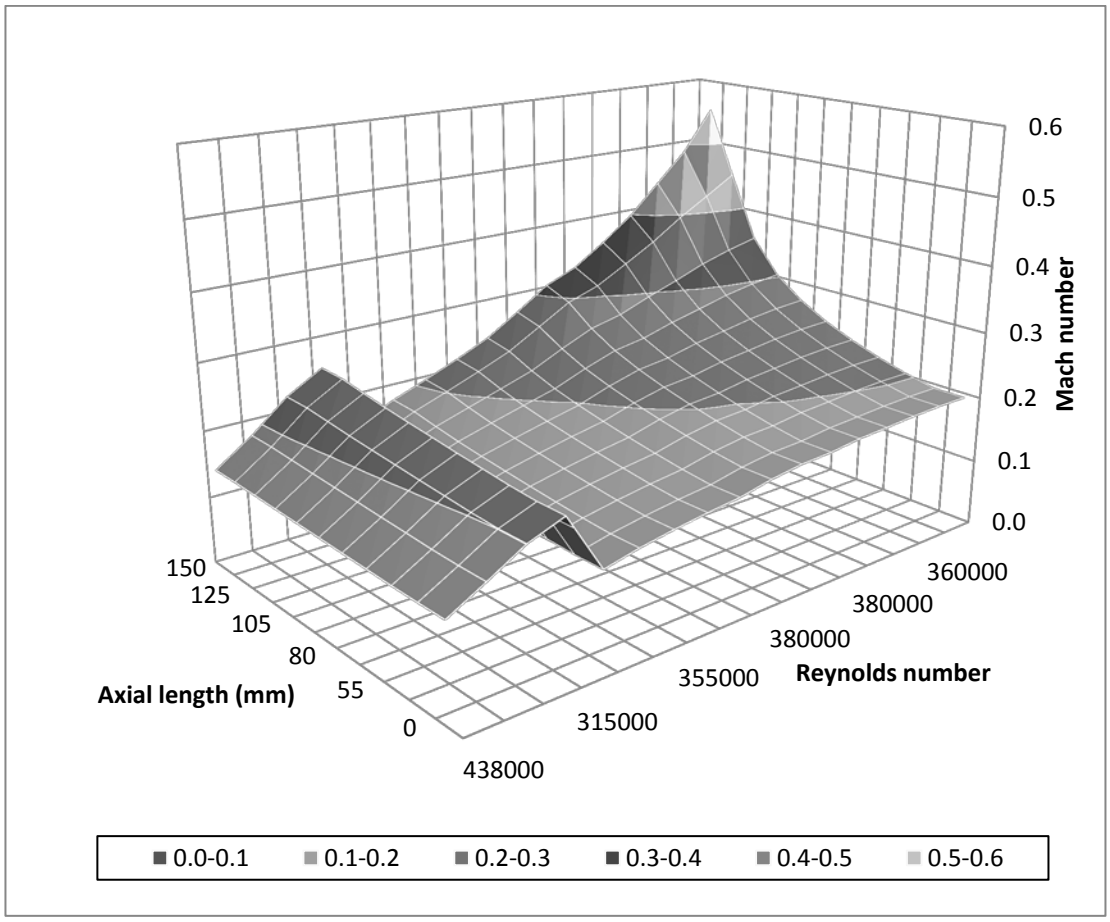

Figure 21– Mach number distribution along the length of the plate with varying Re

The next set of calculations is related to the computation of the Mach number along the length of the plate (using Eq.23). The representation is kept the same as that of the pressure variation in order to maintain uniformity. As seen from Fig. 21, though the

change in Mach number along the length of the plate remains fairly small for the cases before the jump, after the occurrence of the jump, the variation of the Mach number is significant. This indicates that compressibility effects in the flow are substantial and need to be considered while modeling the flow. Another important observation from this plot is that the Mach number does not reach unity even for the case with the highest Reynolds number. Although Asirvatham [1] did observe supersonic flow beyond the test section at the exit and that the flow choked at the exit of the plate in some cases, supersonic flow was not seen in the present case.

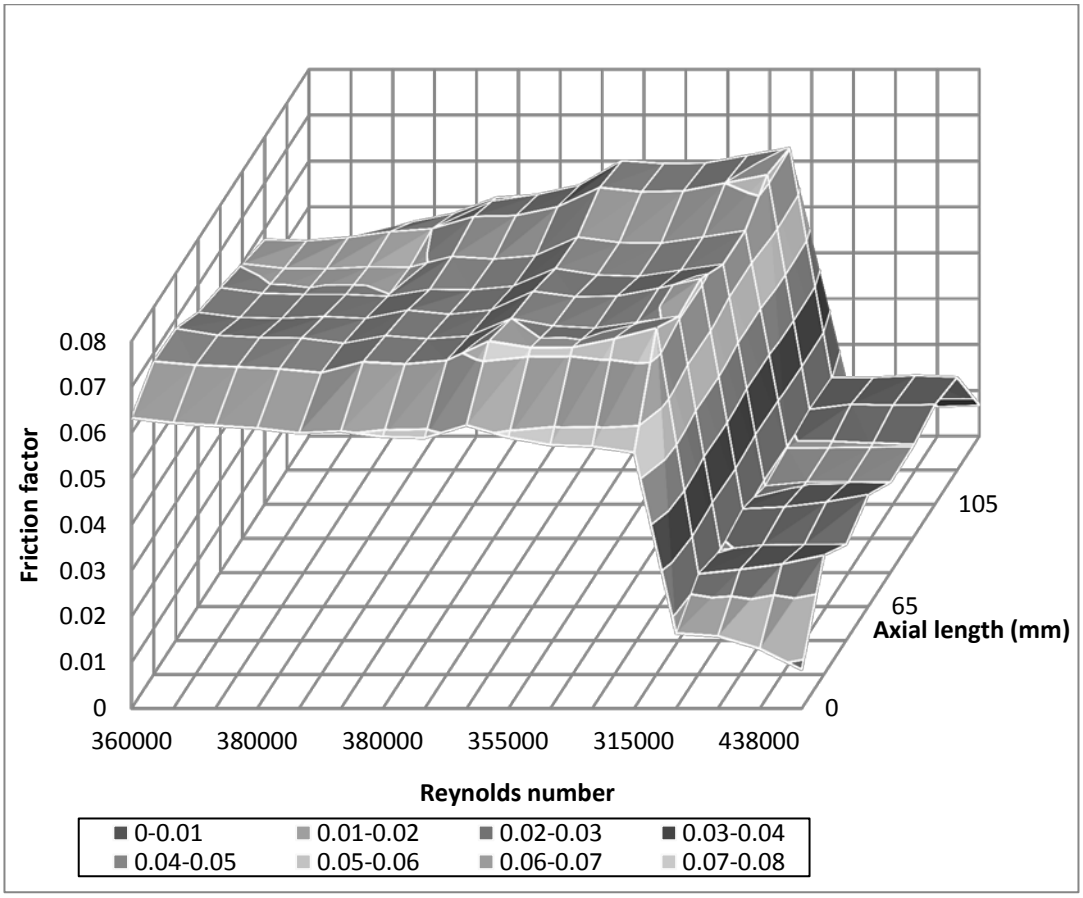

Figure 22– Friction factor distribution along the length of the plate with varying Re

Upon obtaining the Mach number, the next step is to use it to compute the Mach number gradient which is used in Eq. 24 to calculate the Fanning friction factor. Fig. 22 shows the variation of the friction factor along the length of the plate for all the different Reynolds numbers.There are a few observations that can be made from this plot. The first one is that at all values of Re, the entrance and exit effects are apparent in terms of

the friction factor showing a steep gradient at this region**.** The other remark that can be made based on this plot is that there is little variation of the friction factor along the length of the plate, apart from the aforementioned entrance and exit effects – when these values are ignored, it is possible to obtain a single average value of f_f for a given Re. This plot also shows the two distinct f_f values seen as a consequence of the jump; although different Re values show little variation in friction within the two 'zones', there is a large difference in the friction factor across the jump itself.

In order to obtain a closer idea of the nature of the data obtained, spectral analysis of the pressure time trace was carried out. As mentioned earlier, there are four dynamic pressure probes along the length of each plate, all of which have a resonant frequency[1] of 250 kHz. Fig. 23 shows the FFT of pressure taken from the four transducers on the smooth plate at a ΔP of 34,473 pa. This point was before the occurrence of the jump, and as seen here, all channels show a primary, dominant peak at around 1500 Hz. This is followed by the detection of different subdominant harmonics which vary slightly for each channel.

[1] A rule of thumb for dynamic measurement is to select a device with a diaphragm resonant frequency of at least two to three times the highest frequency to be measured. Based on results from available literature [19], frequencies of the order of 50,000 Hz were observed and transducers with 250 kHz were thus chosen.

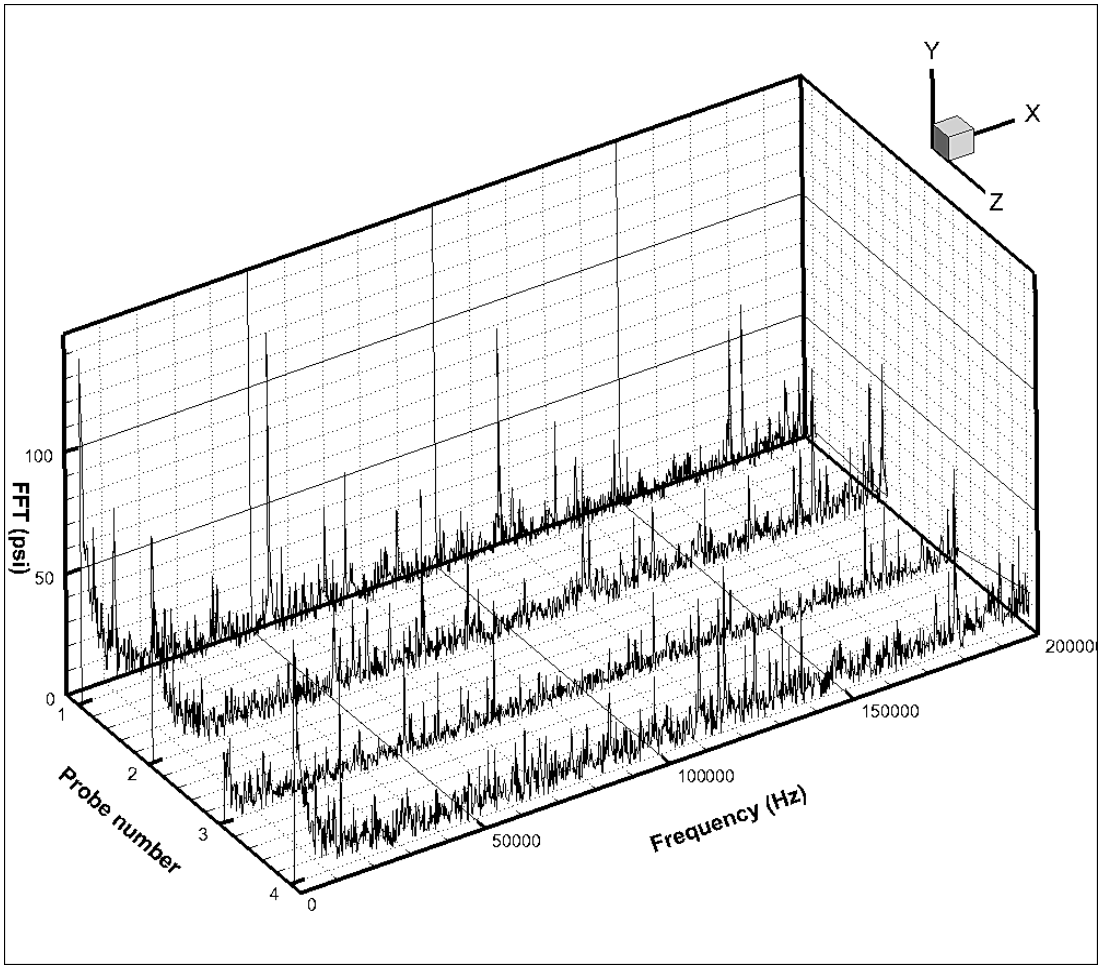

Figure 23 – FFT of pressure signal taken at 4 probes along the length of the plate for case with ΔP = 34,473 Pa

Probe 1, which is closest to the exit of the channel, shows peaks in the spectrum at 52,000 Hz, 114,200 Hz and 180,000 Hz; these peaks can be interpreted as an indication of distinct vortex families with little non-linear interaction between them.

Although all other probes show similar peaks, this probe is seen to allow for a more comprehensive detection of trends since all subdominant modes seen at the other probe locations are still captured at this probe. With this in mind, further analysis was done using the data from probe 1 at all the different ΔP conditions. Another observation made here is that the energy content of the flow is concentrated at the lower frequencies of the measured spectrum which further indicates the presence of large scale structures.

Figure 24 shows the waterfall plot of the FFT data at probe1 on the smooth plate with changing ΔP. This plot shows the variation at three different points – one before the jump, one right at the jump, and one after the jump. Studying the variation shows distinct changes in the spectra with the change in ΔP. As detailed earlier, for the case before the jump at $\Delta P = 5\ psi$ (or 34,473 pa), the spectrum is indicative of an instability mode with large scale, low energy structures resembling the wake mode. The presence of the subdominant modes can be further related to the influence of this large scale structure on the entire flow domain and other possible shedding frequencies from other vortex families.

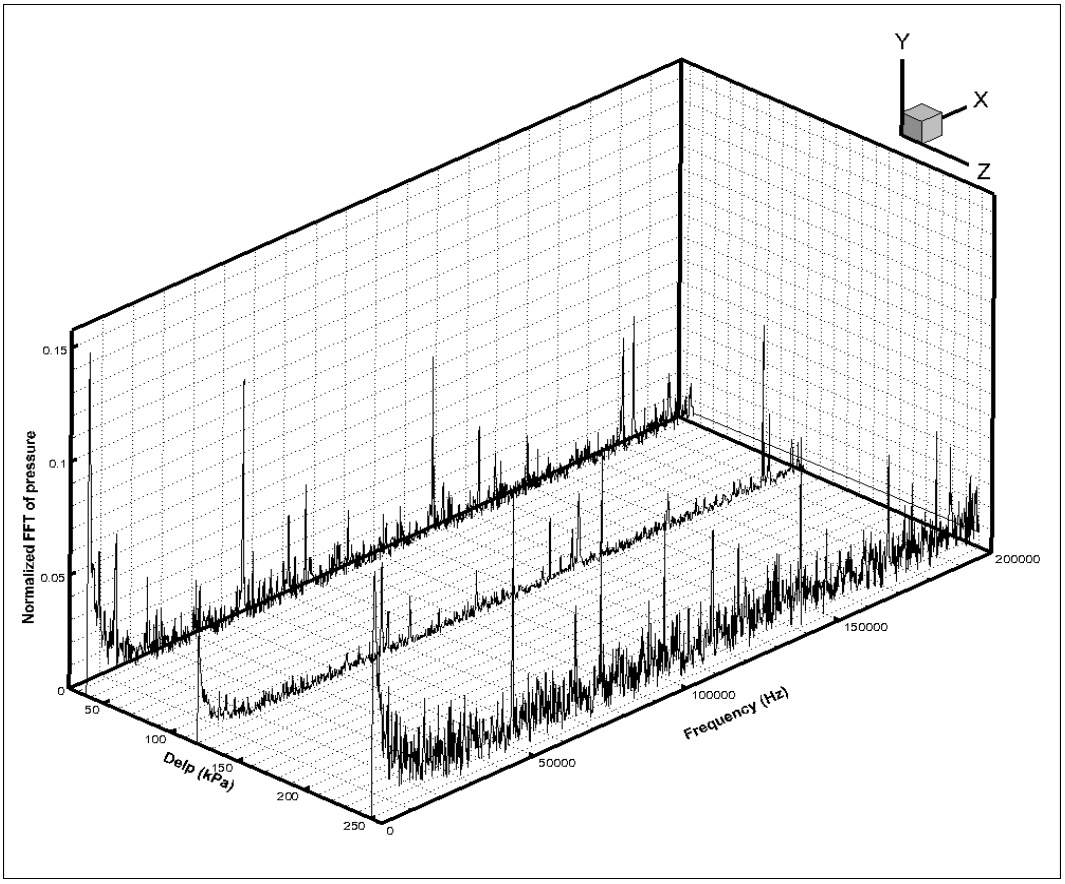

Figure 24 – FFT of pressure signal taken at channel 4 along the length of the plate for cases before, at and after the jump

The distribution at $\Delta P = 17\ psi$ (or 117210 pa) indicates a change in the type of instability. The magnitude of the dominant mode also shows lower energy content as compared to the earlier value and the subdominant modes are not strictly confined to harmonics of the dominant frequency. The dominant frequency in this case is seen at 183000 Hz, with subdominant modes at 122,000 and 61,000 where the presence of

harmonics indicates non-linear interactions between structures. This is a clear departure from the trend seen at the lower ΔP , and denotes transition towards an instability with high frequency vortex shedding and vortex pairing. Further, the broadband noise present in the spectrum is seen to be more subdued as well, indicating the changes in the energy distribution amidst the different structures in the flow. All of these trends suggest a modification in the basic flow behavior from the wake mode to one where the large scale structures seen earlier are not as dominant in the domain.

The last distribution in the waterfall plot is at $\Delta P = 36\ psi$ (i.e. 248211 pa) which shows a noticeably different behavior from what was seen before the jump. High energy content here is seen at much higher frequencies than before with multiple subdominant modes present at harmonics and sub-harmonics of the most dominant frequency. Although the dominant mode is seen at 12,000 Hz, this is followed by harmonics at 48,000 Hz, 72,000 Hz, 96,000 Hz and 144,400 Hz. These harmonics indicate the possible presence of feedback modes (resulting from interactions of the vortices with the downstream corner) which are characteristic of the shear layer instability. This high frequency content is further indicative of many small scale vortices in the flow and suggests the occurrence of vortex-vortex interactions, all of which strengthen the possible presence of a shear layer instability.

All of these experiments and the spectral analysis of the data therefore confirm a change in the flow behavior itself over the occurrence of the jump. This makes it necessary to look more closely into the nature of the flow and truly understand its physics to attempt to find a suitable explanation of this phenomenon.

7. THEORY OF LARGE EDDY SIMULATION AND NUMERICAL MODELS

The goal of carrying out a numerical study for this problem is to allow for an accurate understanding of this flow field without the additional investment of an expensive flow visualization system or rebuilding the test rig. As mentioned earlier, the simulations for this study were performed using ANSYS Fluent (12.0.16) which essentially solves the filtered Navier Stokes equations with a Subgrid scale (SGS) model for the turbulent stress. The idea behind using LES is that it allows for the complete resolution of large eddies while the small eddies are modeled. This is usually a suitable method in engineering applications where the costs for Direct Numerical Simulation (DNS) are prohibitive (the cost requires to resolve the entire range of scales in DNS is proportional to Re^3, making it unaffordable for high Reynolds number calculations). Fig.25 shows the relative differences between LES, DNS and Reynolds Averaged Navier Stokes (RANS) with respect to resolving all scales of a problem. The use of LES can be further justified by the following reasons –

- Momentum, mass and energy are mainly transported by the large eddies
- Large eddies are directly influenced by the geometry of the domain and the boundary conditions applied
- Small eddies are more universal , isotropic and less dependent on the problem
- It is easier to model small eddies owing to the properties listed above, which is what LES does

Although using LES helps obtain a compromise between the cost of DNS and the approximations of RANS, it should be remembered that LES still needs fine meshes and long flow-times to obtain useful results. It is therefore important to understand the implementation of this technique correctly before attempting to apply it to a problem.

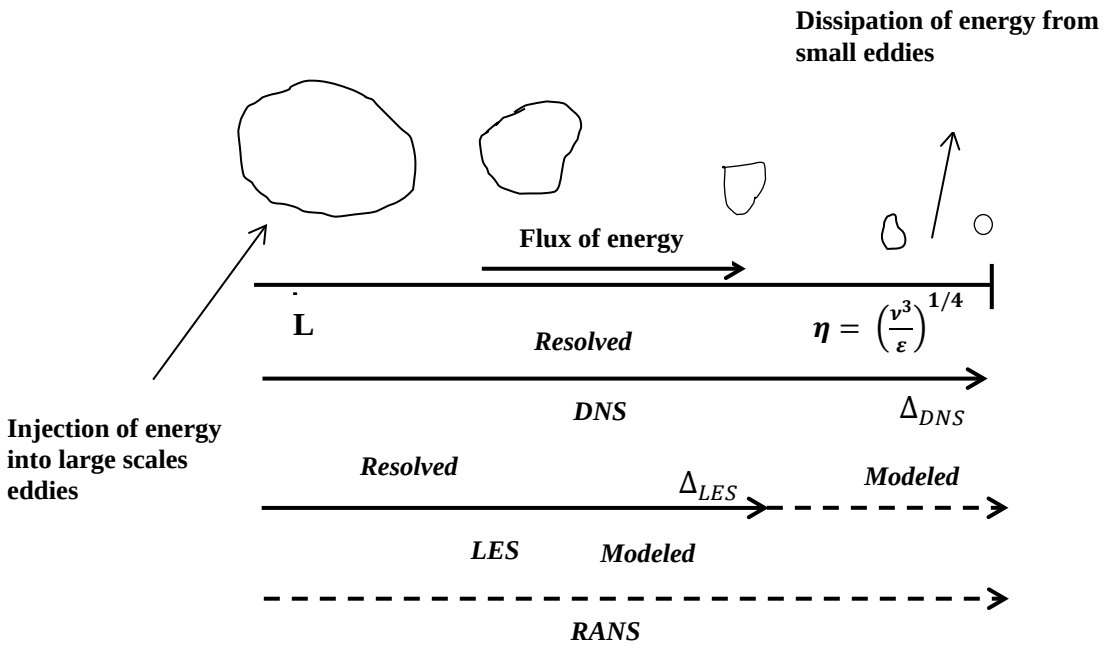

Figure 25 – Energy Cascade superposed with difference between the three modeling techniques

The starting point of LES are the governing equations used which are obtained by filtering the time-dependent Navier-Stokes equations. This process essentially filters

out the eddies whose scales are smaller than the filter width or the grid spacing that is used in computations [25].

A filtered variable is defined by –

$$\bar{\phi}(x) = \int_D \phi(x')G(x,x')dx' \tag{17}$$

where D is the fluid domain, and G is the filter function that determines the scale of the resolved eddies.

Since Fluent uses the finite-volume discretization method, the implicit filtering in this case is –

$$\bar{\phi}(x) = \frac{1}{V}\int_v \phi(x')dx' \qquad ,x' \epsilon v \tag{18}$$

where V is the volume of the computational cell.

The filter function, $G(x,x')$ is –

$$G(x,x') = \frac{1}{V} \qquad for\ x' \epsilon v \tag{19a}$$

$$G(x,x') = 0 \qquad for\ all\ other\ values\ of\ x' \tag{19b}$$

Filtering the Navier-Stokes equations using $\boldsymbol{u}(\boldsymbol{x},t) = \bar{\boldsymbol{u}}(\boldsymbol{x},t) + \boldsymbol{u}'(\boldsymbol{x},t)$ where $\bar{\boldsymbol{u}}(\boldsymbol{x},t)$ represents the resolved scales and $\boldsymbol{u}'(\boldsymbol{x},t)$ represents the subgrid scale gives –

$$\frac{\partial \rho}{\partial t} + \frac{\partial}{\partial x_i}(\rho \overline{u_\iota}) = 0 \tag{20a}$$

$$\frac{\partial (\rho \overline{u_\iota})}{\partial t} + \frac{\partial}{\partial x_j}\left(\rho \overline{u_\iota u_J}\right) = \frac{\partial}{\partial x_j}\left(\sigma_{ij}\right) - \frac{\partial \bar{p}}{\partial x_i} - \frac{\partial \tau_{ij}}{\partial x_j} \tag{20b}$$

where σ_{ij} , the stress tensor due to molecular viscosity is defined by

$$\sigma_{ij} \equiv \mu\left(\frac{\partial \overline{u_\iota}}{\partial x_j} + \frac{\partial \overline{u_J}}{\partial x_i}\right) - \frac{2}{3}\mu \frac{\partial \overline{u_\iota}}{\partial x_i}\delta_{ij} \tag{21}$$

and τ_{ij} is the subgrid stress defined by –

$$\tau_{ij} \equiv \rho\overline{u_i u_j} - \rho\overline{u}_i\overline{u}_j \tag{22}$$

This subgrid stress is the part of the equation that is modeled.

Applying the Boussinesq hypothesis,

$$\tau_{ij} - \frac{1}{3}\tau_{kk}\delta_{ij} = -2\mu_t\overline{S_{ij}} \tag{23}$$

where μ_t is the subgrid scale turbulent viscosity and $\overline{S_{ij}}$ is the rate-of-strain tensor for the resolved scale defined by –

$$\overline{S_{ij}} \equiv \frac{1}{2}\left(\frac{\partial\overline{u_i}}{\partial x_j} + \frac{\partial\overline{u_j}}{\partial x_i}\right) \tag{24}$$

For compressible flows, as in this case, it is convenient to introduce a density-weighted (also known as Favre) filtering operator as –

$$\tilde{\phi} = \frac{\overline{\rho\phi}}{\rho} \tag{25}$$

Though the Favre-averaged Navier-Stokes equations are of the same form as those written out in Eq.5, the subgrid stress tensor is defined as -

$$\tau_{ij} = \overline{\rho}\widetilde{u_i u_j} - \overline{\rho}\widetilde{u}_i\widetilde{u}_j \tag{26}$$

This term is split into its isotropic and deviatoric parts as –

$$\tau_{ij} = \tau_{ij} - \frac{1}{3}\tau_{kk}\delta_{ij} + \frac{1}{3}\tau_{kk}\delta_{ij} \tag{27}$$

where the first two terms on the right hand side represent the deviatoric part and the last term represents the isotropic part. The deviatoric part of the subgrid scale stress tensor is modeled using the compressible form of the Smagorinsky model -

$$\tau_{ij} - \frac{1}{3}\tau_{kk}\delta_{ij} = 2\mu_t\left(S_t - \frac{1}{3}\tau_{kk}\delta_{ij}\right) \tag{28}$$

The term μ_t i.e. the eddy viscosity, is modeled by the Smagorinsky- Lilly model as –

$$\mu_t = \rho L_S^2 |\bar{S}| \tag{29}$$

where L_S is the mixing length for the subgrid scales and $|\bar{S}| \equiv \sqrt{2\ \bar{S}_{ij}\ \bar{S}_{ij}}$.

In Fluent, L_S is computed using

$$L_S = \min(\kappa d, C_s \Delta) \tag{30}$$

where κ is the von Karman constant, d is the distance to the closest wall, C_s is the Smagorinsky constant and Δ is the local grid scale which is computed from the volume of the computational cell using $\Delta = V^{1/3}$. Though the value of C_s has been determined as a non-universal , a value of around 0.1 has been found to yield the best results for a variety of flows and was the value used for this study.

8. SIMULATION OF SHEAR LAYER AND WAKE MODES USING LARGE EDDY SIMULATIONS

As discussed earlier, the first step in the numerical study involves the simulation of two different open cavities with the dimensions and boundary conditions taken from benchmark studies [19, 23]. This chapter reviews the results from these simulations and characterizes the mechanisms at the onset of the instabilities.

8.1 Results from simulations for cavity with L/D = 2

The domain for this simulation is as shown in Fig. 9, the dimensions of which were discussed in the methodology section. In order to simulate the occurrence of the shear layer instability, as was predicted by Rowley [19], the boundary conditions were maintained in accordance with this study and this resulted in setting the Mach number at the inlet to 0.6. The simulations are initiated by spanning the cavity with a Blasius flat-plate boundary layer. Using the Reynolds Averaged Navier-Stokes equations (RANS) with the standard k-ε model, the simulation is allowed to run till the flow field is reasonably converged. An instantaneous flow field is then obtained from the steady state RANS results which provide a realistic starting point for LES. This also helps in reducing the time needed for LES to reach a statistically stable solution [29].

Once a steady state solution has been reached using RANS, the LES model is turned on with a time step size of 1e-8 seconds (with a maximum of 150 iterations per time step) and is allowed to run until the flow becomes statistically steady. After this step, the initial statistics are zeroed out and the **Data Sampling for Time Statistics**

option is enabled in Fluent. This ensures that Fluent gathers time statistics while performing the simulation; also, the **Sampling Interval** was set to once per iteration for each time step to enable the maximum frequency of data collection. The simulation is then continued until statistically stable data is obtained – this is done by allowing the solution to run for at least 5-6 mean flow residence times (where the mean flow residence time is defined as L/U with L as the characteristic length of the domain and U as the characteristic mean flow velocity). For this particular case of L/D = 2, the flow-through time (FTT) was found to be 9.17e-6 sec and the flow was therefore run for 9e-5 seconds *after* obtaining a statistically converged flow in order to ensure beneficial statistics. Fig. 26 shows the variation of pressure at X = 7D (downstream of the cavity) with the flow through time and the repeating oscillations show that statistical stability has been achieved.

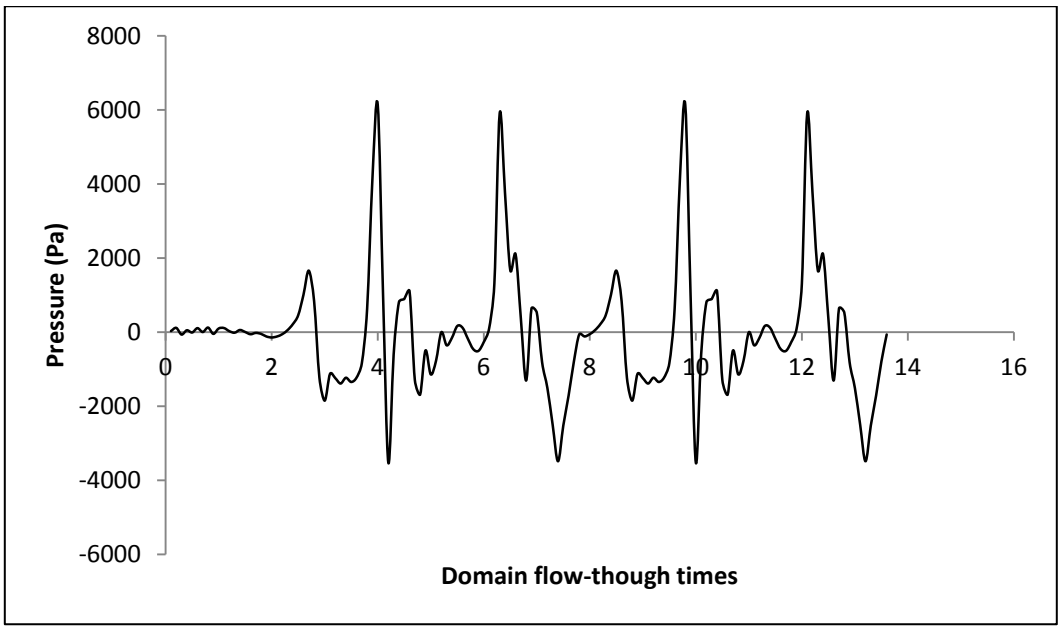

Figure 26 – Variation of pressure with FTT to monitor statistical stability

Fig. 27 shows the vorticity contours for the cavity, as they change with time. The geometry of this cavity along with the imposed boundary conditions leads to the occurrence of the shear layer instability. As described in the earlier sections, this instability is characterized by the following sequence of events – the roll-up of vorticity in the shear layer, the impingement of the resulting disturbances on the downstream cavity edge, upstream propagation of these disturbances and finally the receptivity of the shear layer to this propagation [19]. This process is clearly seen in the results from the LES. The movement of the vortices in the shear layer is apparent with the rest of the flow in and outside the cavity being fairly quiescent. The animation shows the vortices

being shed from the upstream edge of the cavity and traveling along the upstream edge. Vortices of the opposite sign are also seen to be generated and shed against the downstream wall of the cavity and this is the result of the interaction of the upstream disturbance with the downstream flow.

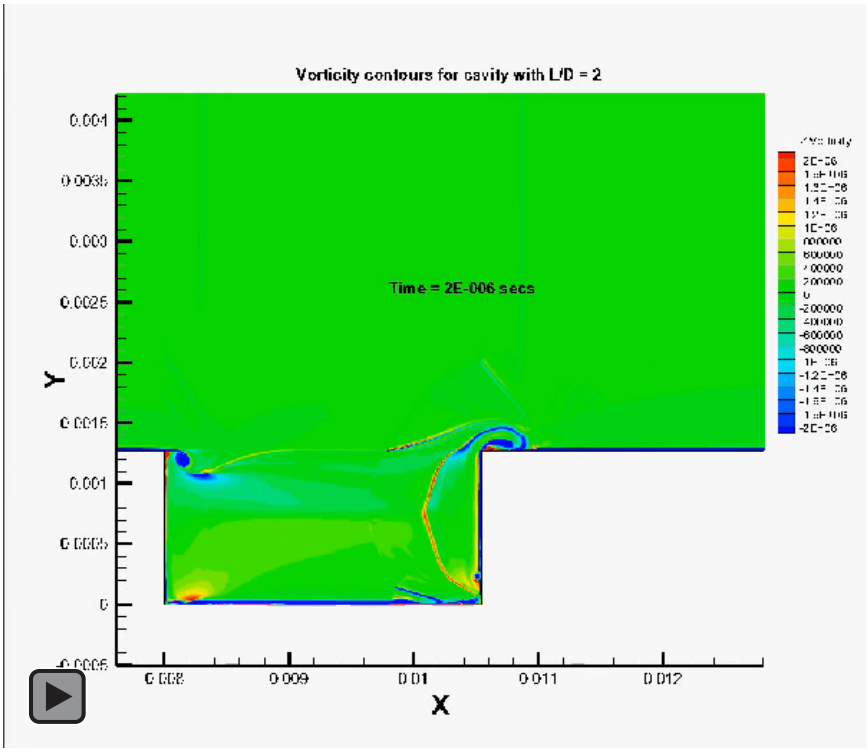

Figure 27 – Variation of Z vorticity with time showing shear layer instability

Fig. 28 shows the time-averaged (over the duration of one 'cycle' of the plot shown in Fig.26) flow for the cavity in terms of the X velocity contours superposed with the streamlines. This was done in order to obtain a qualitative verification of the nature of the instability by comparing it to the results from Rowley [19]. As seen in the comparison, both simulations show the presence of two large vortex structures whose influence is seen through the depth of the cavity. There is also a minimal disturbance above the cavity for both cases which is distinctive of the shear layer instability.

In order to confirm the presence of the shear layer instability and provide a more quantitative comparison with available results [19], the dominant frequency and the Strouhal numbers were also calculated from the results of the LES. As seen in Fig. 29, a dominant frequency of 32.2 kHz was obtained which translates to a Strouhal number (based on the length of the cavity) of 0.401. This compares well to the St value obtained by Rowley [19] which was 0.41 and this was also shown to be in accordance by the value predicted by Rossiter's formula for the mode with *n=1*. Another measure of comparison was provided by obtaining the ratio of the length of the cavity to the momentum thickness of the boundary layer (L/θ_0) – this was reported as 52.8 from the DNS simulations and the obtained to be 41.6 from the LES test case.

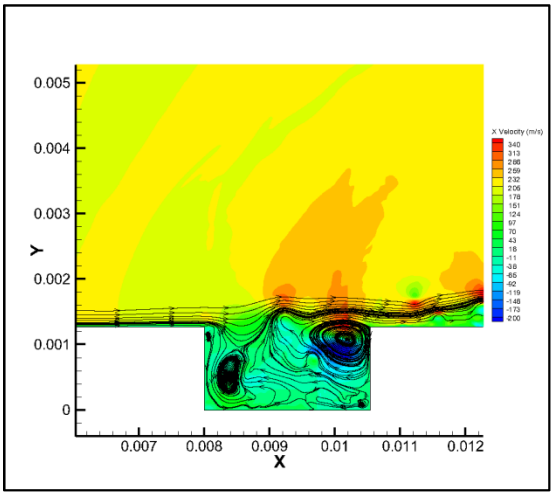

(a)

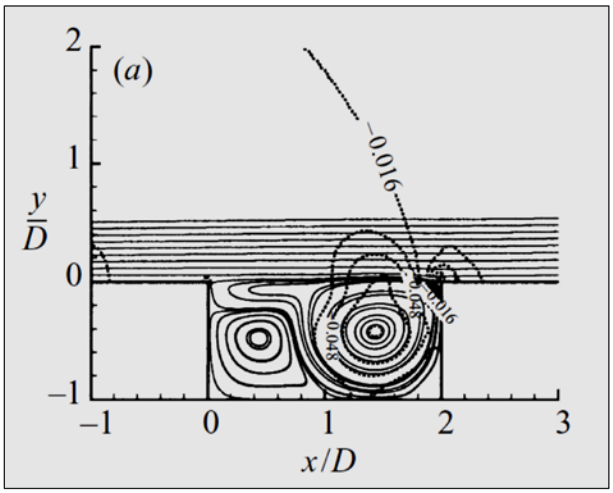

(b)

Figure 28 (a) – Time-averaged flow showing contours of X velocity superposed with streamlines for cavity with L/D = 2, (b) Time-averaged flow for DNS results from Rowley[19]

In addition to the predicted dominant modes, the simulations also show subdominant harmonic modes at 161 kHz and 275.6 kHz. The peak at 161 kHz is reminiscent of the counter rotating paired vortices that are generated via shedding from the upstream lip while the highest frequency is owing to the feedback loop that is set up due to the vortex-downstream edge interaction.

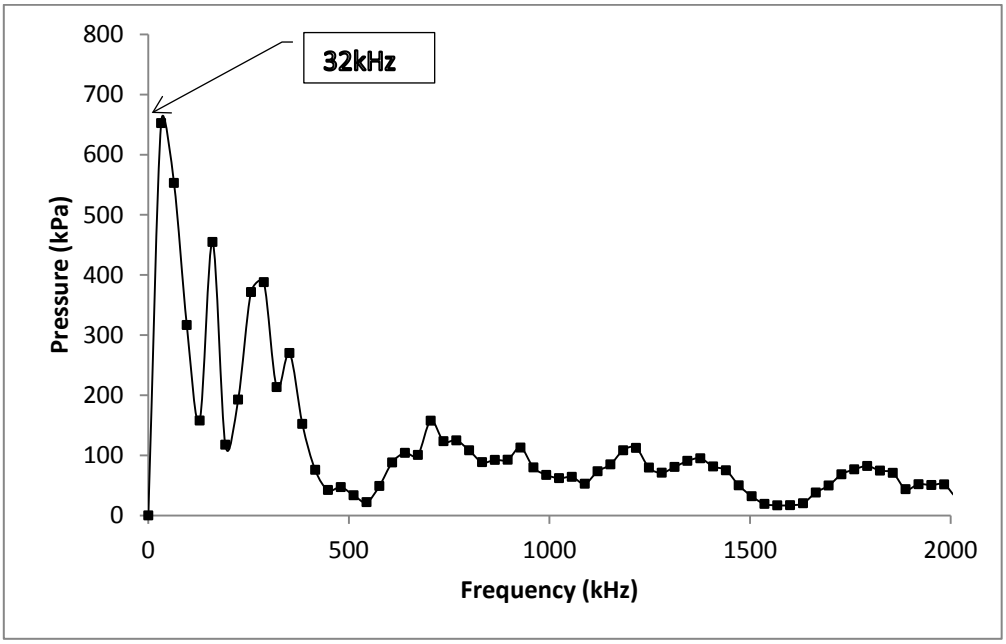

Figure 29 – Spectrum of pressure at upstream edge of cavity for cavity with L/D = 2

8.2 Results from simulations for cavity with L/D = 4

The next set of simulations involved modeling the flow through a cavity with a length to depth ratio of 4, keeping the boundary conditions the same as the previous case. Fig. 30 shows an animation of this simulation which was performed by following the same set of steps as accounted for the previous case. As seen in this case, there is a large scale shedding of vortices from the leading edge of the cavity.

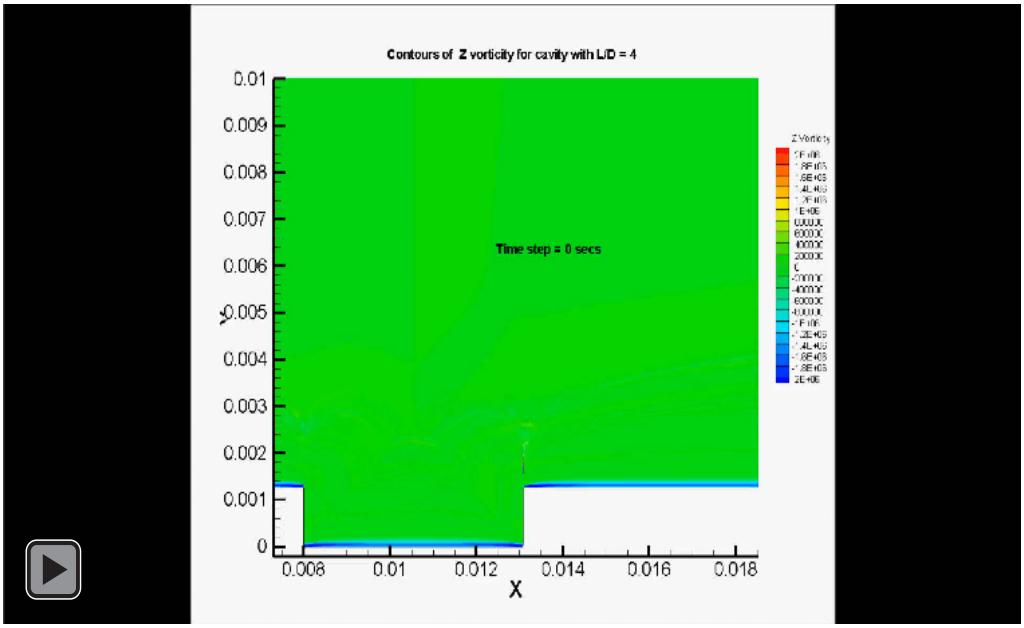

Figure 30 – Variation of Z vorticity with time showing wake mode instability

This was first investigated by Gharib and Roshko [18] who described the regime as the *wake mode*. The identifying characteristic of this instability is that the shed vortices have dimensions comparable to the cavity size. As this vortex is forming, free-stream fluid is directed into the cavity and impinges at the base, causing the shed vortex to be ejected from the cavity. Owing to the large size of the vortex, there is a potential for flow separation both upstream of the cavity and also in the boundary layer downstream as it is being convected away [19].

Fig. 31 shows the time-averaged flow for the cavity in terms of the X velocity contours superposed with the streamlines compared with a corresponding plot from Rowley [19]. As seen, the LES is able to replicate the results of the DNS data fairly well. Both plots show the presence of two distinct vertical structures, one whose dimensions are comparable to the cavity itself. The LES, however, slightly over predicts the size of the smaller vortex seen close to the leading edge of the cavity.

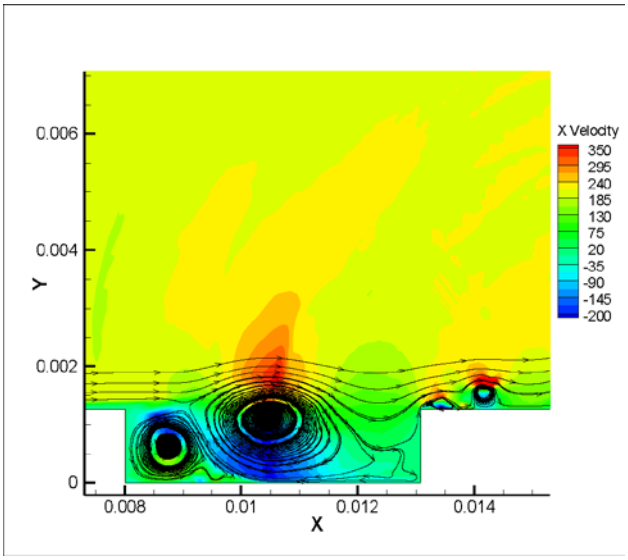

(a)

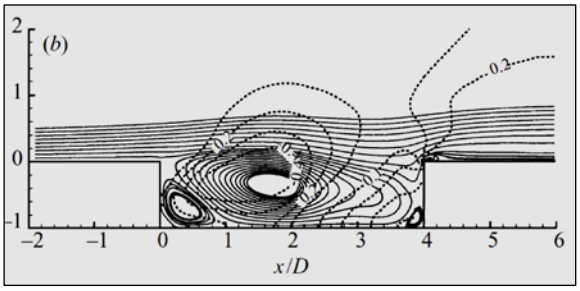

(b)

Figure 31(a) – Time-averaged flow showing contours of X velocity superposed with streamlines for cavity with L/D = 4, (b) Time-averaged flow for DNS results from Rowley[19]

The flow is also seen as strongly recirculating and as indicated by the C_p contours in Fig. 32, there is an impingement of the recirculating flow on the rear wall. These contours also show a significant variation in pressure from -0.25 in the impingement region to a

maximum of around 0.6 where the flow expands into the cavity. These values correlate with the pressure data of the benchmark study [19] as well where the range of C_p was from -0.3 to 0.5.

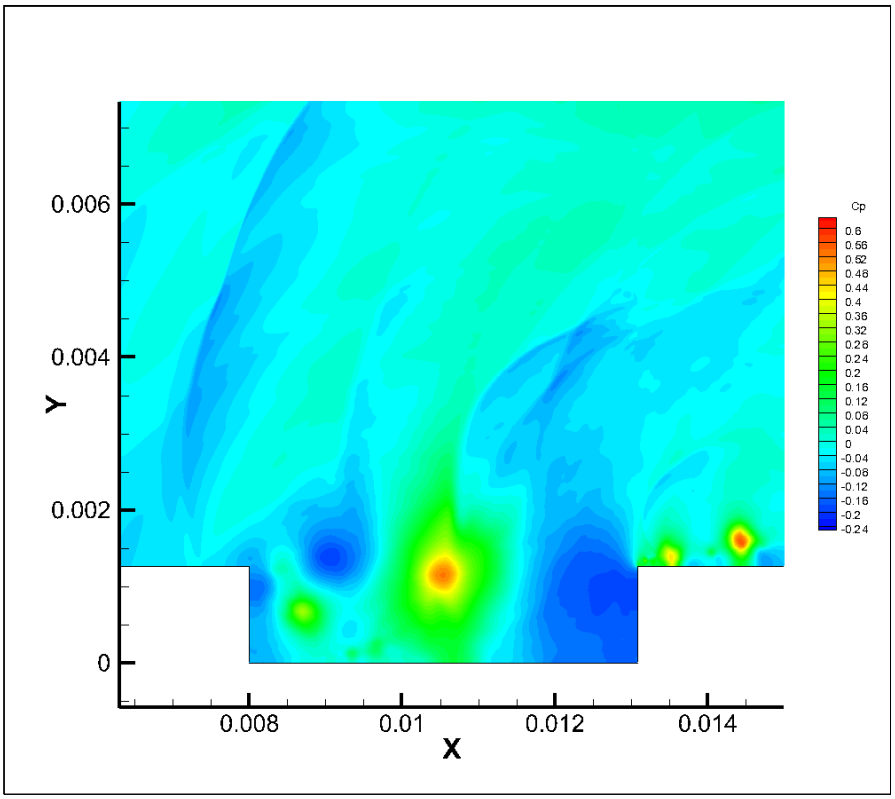

Figure 32 – Time-averaged flow showing contours of C_p for cavity with L/D = 4

As in case of the cavity with L/D =2, in order to obtain a quantitative verification of the nature of the instability, an FFT of the pressure at the upstream lip was carried out and the results as shown in Fig. 33. The dominant frequency obtained in this case was 12 kHz which corresponds to a Strouhal number of 0.29 and which compares well to the value of 0.25 reported by Rowley [19]. The ratio of the length of the cavity to the momentum thickness of the boundary layer (L/θ_0) was also obtained – this was reported as 102.1 from the DNS simulations and the obtained to be 117.1 from the LES test case. These results thus show that the numerical method chosen is suitable for the detection of both the shear- layer and the wake mode instabilities.

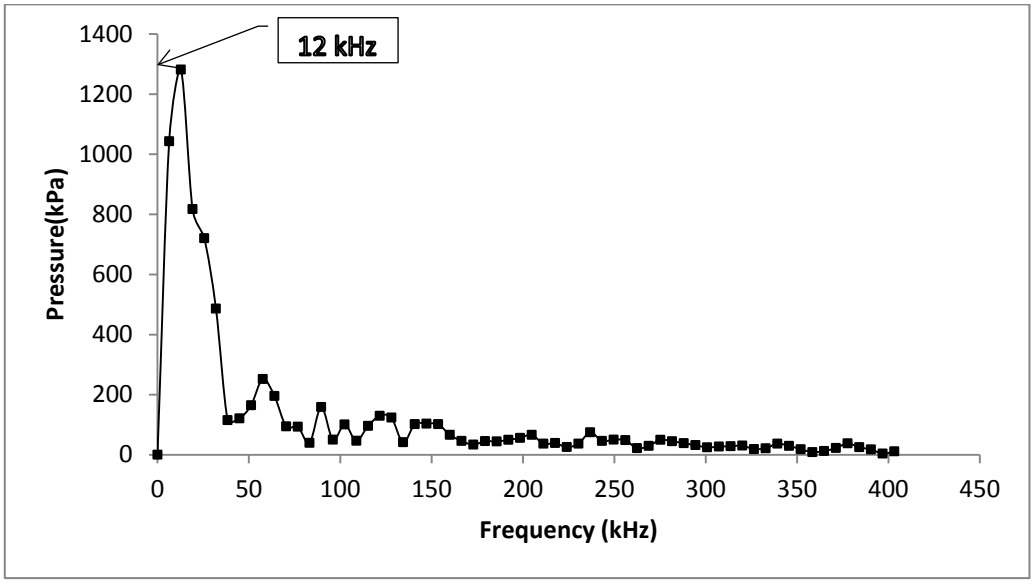

Figure 33 – Spectrum of pressure at upstream edge of cavity for cavity with L/D = 4

8.3 Comparison of the two instability modes

Fig. 34 shows the X velocity contours superposed with the streamlines for both cavities at the same flow times. In case of the shear layer instability, there are small vortices being shed from the leading edge of the cavity that travel to the downstream edge and the resulting disturbances travel upstream to affect the flow there. The progression of the wake mode on the other hand, initially indicates the effect of the previously shed vortex in terms of the streamlines showing the expulsion along the downstream edge. The vortex structure being formed in this case is also seen to have a much slower growth as compared to the shear layer vortices.

Another distinct difference between the two instabilities is seen in the effect of the vortex shedding on the flow outside the cavity – while the streamlines outside the cavity are minimally disturbed in case of the shear layer instability, the wake mode shows the effect of formation and shedding to extend to a height equal to the depth of the cavity itself, into the domain.

The aforementioned trends are reinforced from the spectra in Fig 29 and 33. While the spectrum of the shear layer instability shows a high frequency dominant mode which are followed by a couple of sub-dominant modes all in the same frequency range, the wake mode spectrum shows one dominant peak at a frequency that is a third of the that seen in the former case and no distinct subdominant modes. Rowley [19] also noted that the fundamental period seen in case of the wake mode, corresponded with the vortex shedding from the leading edge. The same study also showed that there was no variation of this fundamental frequency with change in Mach number, proving that the wake mode

is hydrodynamic and not acoustic in nature. Comparing the computed values of L/θ_0, it is also observed that the wake mode typically occurs for higher values of this ratio (there are however other parameters which determine this such as the Mach number and the Reynolds number).

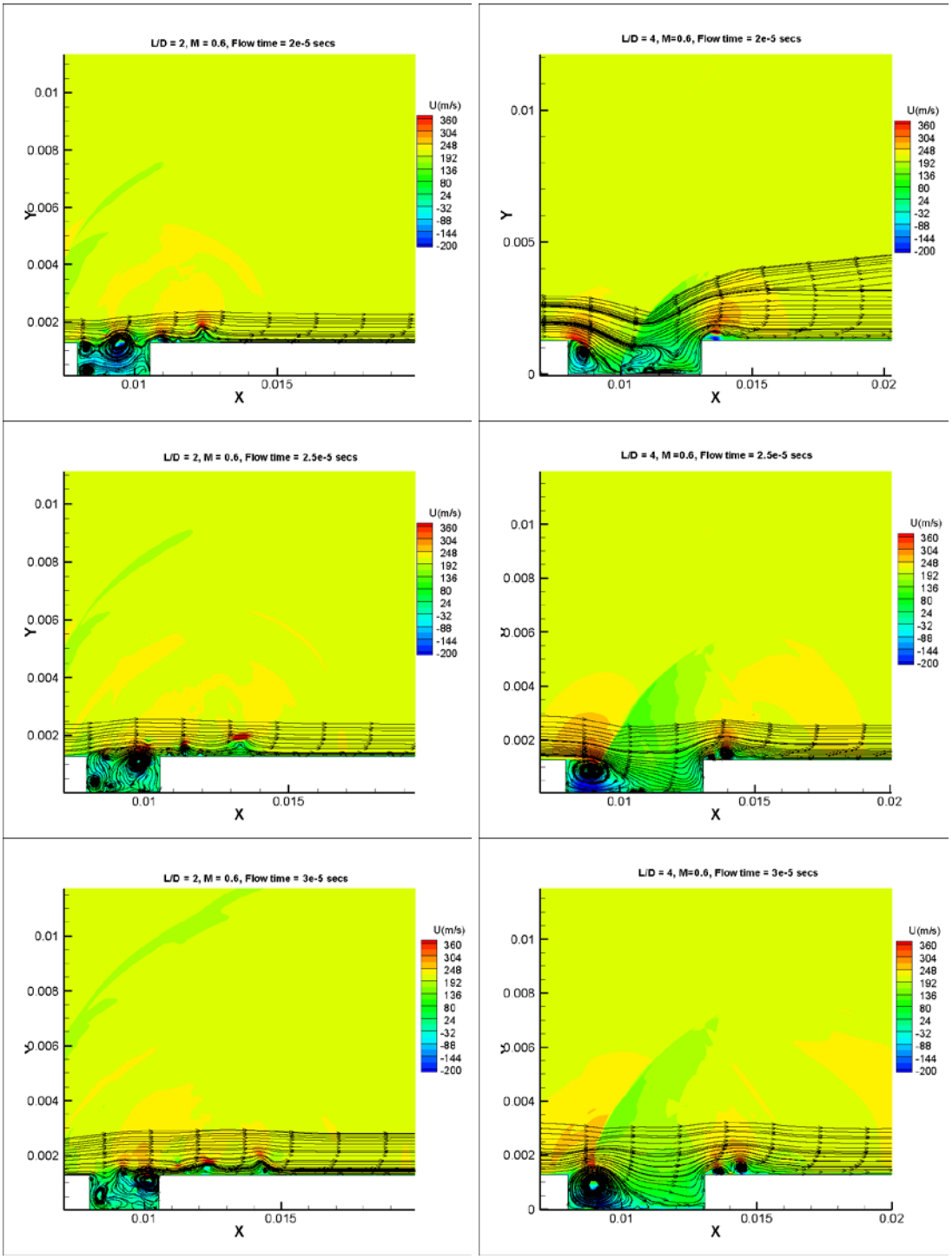

Figure 34 – Comparison of velocity contours and streamlines of the two instabilities at the same flow times

9. SIMULATION OF FLOW THROUGH A CAVITY OF THE HP SEAL USING LARGE EDDY SIMULATIONS

Although an extensive amount of research has been done on cavity flow where the cavity is away from the influence of solid boundaries, there has been a limited amount of study in trying to simulate or visualize the flow where the effect of the top boundary is of significance. Before attempting to study these cavities however, it is important to have a thorough knowledge of the characteristics of shear layers in compressible flows and their interaction with solid boundaries. The following section will attempt to recapitulate the findings so far and define concepts that have been established, in order to explain new findings clearly.

9.1 Shear layer dynamics and properties of excited shear layers

The subject of free shear layers has been studied by many researchers and the current study refers to the series of lectures by Gloerfelt [30] which provides a comprehensive review of the same. Shear layers in turbulent and transient flows have been studied using both statistical and *quasi-deterministic* methods (where the vortex structures are seen as the main building blocks of the mixing layers) and these studies, in combination have allowed extending of theories to analytical descriptions [31]. This was done using classical hydrodynamic stability theory where the unsteady mixing layer is conceptualized as a superposition of interacting instability waves that propagate and amplify in the downstream direction. It was seen that linear stability analysis was able

to describe the initial development of the mixing layer preceding the establishment of fully rolled-up vortices. Also, in conjunction with an appropriate phenomenological model this analysis can help determine physical parameters such as length scales of the structures.

The sequence of events in the shear layer for open cavities is described concisely by Gloerfelt [30] and reads as follows – as the incoming boundary layer reaches the upstream cavity edge, a mixing layer[2] is generated with the quiescent fluid in the cavity. The mean velocity profile then experiences an unstable inflection point (by the application of the Rayleigh theorem) and accordingly, linear, Kelvin-Helmholtz instabilities grow exponentially (as shown by Miksad [32]). Once the primary instability is saturated, non-linear instabilities start to develop and are seen as harmonics in the velocity spectra. These sub-harmonic components also lead to secondary instabilities that result in vortex-pairing events.

[2] The mixing layer is defined to be different from the shear layer in that the mixing layer is the flow that forms between two uniform, nearly parallel streams of different velocities [31]. Therefore all mixing layers can be referred to as shear layers but the converse is not always true.

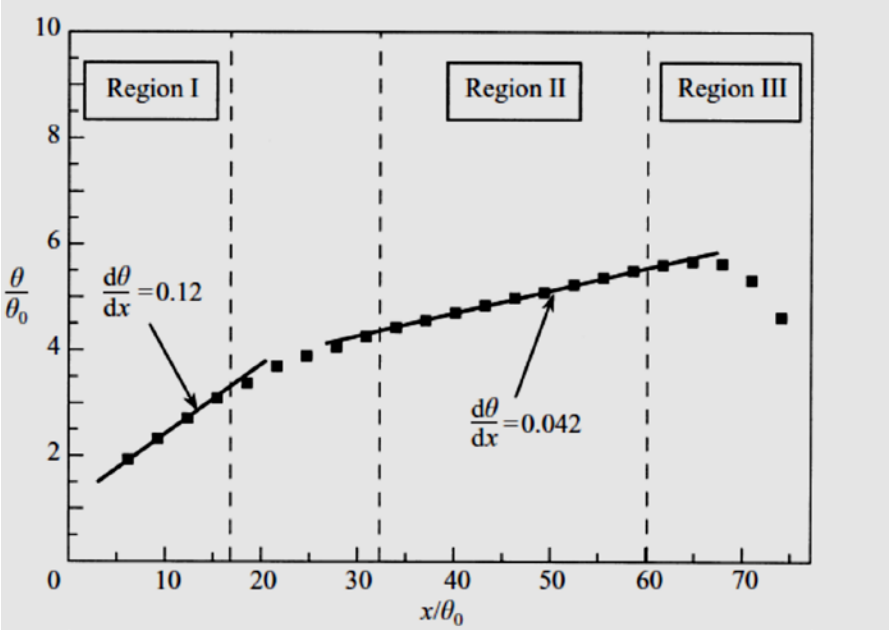

Figure 35 – Variation of momentum thickness in the mixing layer [35]

These events have also been confirmed experimentally by monitoring the momentum thickness of the mixing layer over the length of the cavity (i.e. between the upstream and downstream edges). Studying and characterizing the variation led to the following results – an initial region of high spreading rate (corresponding to the formation of large-scale Kelvin-Helmholtz vortices) is observed; this is followed by a second region where the growth is negligible owing to the absence of vortex pairing. The last region is the one that is a result of the impingement process – the motion near the downstream lip causes larger vertical components of velocity which translate to a high spreading rate. This is shown quantitatively in the experiments of Forestier et al. [34] as seen in Fig.35.

A feature that all shear flows have in common and that is the basis of possible structural vibrations is the principle of *selective amplification* [35]. This essentially states that energy transfer from the mean flow to the disturbances is a function of multiple parameters such as the geometry of the cavity and the flow itself but the frequencies of the disturbances are an important factor as well. A linear stability analysis of jet flows [36] also indicates that beyond a critical Reynolds number, only disturbances in a certain frequency range are amplified; this implies that even random disturbances in the incoming flow could be amplified to give periodic flow conditions at a specific frequency.

9.2 Vortex coalescence and collective interaction

Certain cavities at specific L/D ratios and subsonic Mach numbers have been seen to exhibit vortex pairing along with the occurrence of the shear layer instability [37]. This phenomenon, which is seen to occur near the downstream edge of the cavity, is important since it not only affects the growth of the mixing layer but is also seen to cause changes in instability modes. In addition to this, it was also hypothesized that vortex pairing was due to the presence of sub-harmonic instabilities (the formation of which was described in the previous section) in the flow but it was later on proved that though a sub harmonic could trigger pairing this was not the only reason for it. Moon and Weidman [38] also observed that the pairing of vortices in the free shear layer was usually intermittent and a ‘dropout’ vortex was frequently found between the upstream and downstream vortices.

Early shear layer growth also shows that the formation of large scale structures is possible through a collective interaction at the upstream edge of the cavity - this essentially translates to the fusion of smaller vortices being shed at the most unstable frequency of the shear layer. The occurrence of this phenomenon is seen to be important in the determination and analysis of the main oscillation frequencies of the flow and is also seen to affect the spreading rate dramatically. As observed by Ho and Huang [39], in a forced mixing layer, the initial formation of the vortices depends on the stability process and the external forcing function. The vortices form at the response frequency and the interaction between the fundamental, the response frequency, and the Mth sub-harmonic and the forcing frequency leads to the merging of *M* vortices.

9.3 Mechanics of vortex impingement at the downstream cavity edge

The point of interaction of the vortex with the downstream edge of the cavity is another important phenomenon that helps understand the effect of the resulting pressure fluctuations on the flow mechanism.

The work of Rockwell and Knisely [40] has helped classify four different vortex-corner interactions as follows –

(a) Complete clipping - this is when the impinging vortex is swept almost entirely into the cavity

(b) Complete escape – this is seen as almost the opposite of the *complete clipping* mechanism where the vortex structure bypasses the edge completely and travels downstream over it.

(c) Partial clipping – this accounts for cases where a part of the vortex is shed over the cavity edge but a majority of the clipped vortex is swept inside the cavity

(d) Partial escape – this is the opposite of *partial clipping* and is said to occur when a majority of the clipped vortex escapes over the downstream corner of the cavity

All four interactions are shown in Fig. 36, however it should be noted that this is just an indicative sketch; the strength of the vortices and the wavelength between successive vortices is not shown here.

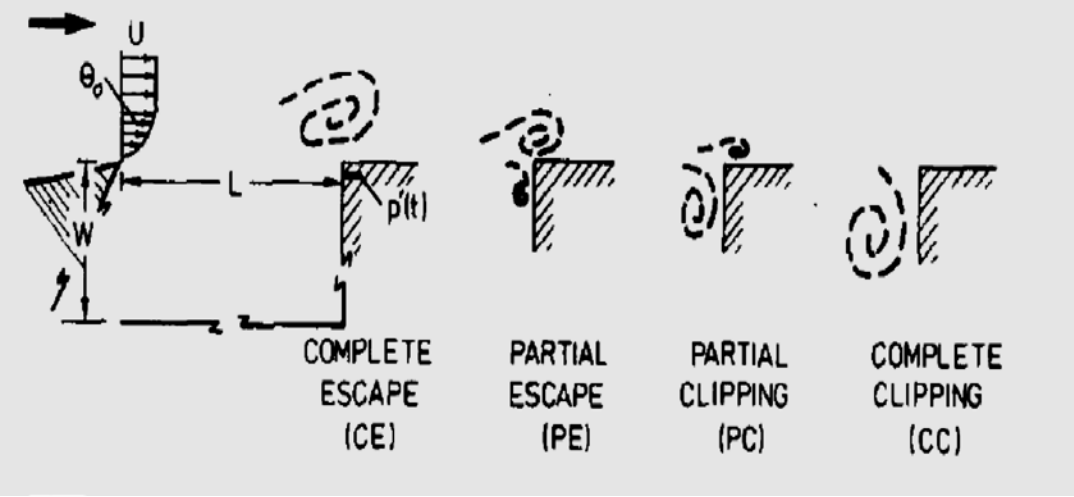

Figure 36– Classes of possible vortex-corner interactions [38]

The interaction produced is dependent on the mean flow, the geometry of the cavity and also any previous interactions seen in the system. Another important observation made is that these interactions are not limited to one specific kind for the duration of the flow – the occurrence of interactions was seen to be ordered, rhythmic and even cycling between the different classes mentioned. This random alternance, between classes, also known as *jitter,* was seen to induce intermittency and low frequency components into the flow. Further, it was seen that when *complete clipping* occurs, the recirculation zone induced by the cavity walls can also modify the trajectory of the vortical structures in the shear layer [30]. This phenomenon has been completely ignored in all the theoretical attempts to model self-sustained oscillations, but has an important effect in the occurrence and sustenance of vortex-corner interactions.

9.4 Formulation of domain and boundary conditions for LES

As mentioned in chapter 4, after the determination of a suitable simulation technique, the next step is to apply this technique to the current problem at hand to study the flow closely. Based on the literature available and the resources on hand, it was chosen to carry out LES for the domain shown in as discussed in Chapter 6. The boundary conditions were then determined based on the experimental data from Asirvatham [1]. Fig. 37 shows the variation of the mass flow rate with the change in pressure difference as seen in this study.

The occurrence of the friction factor jump is seen to translate to a jump in the mass flow rate (it should be recalled here that the *difference* in pressure refers to the pressure drop in the mean flow direction). In order to truly understand the nature of the jump, there were two conditions chosen for simulations – one at the maximum flow rate and one after the occurrence of the jump. The following sections describe the results and findings at each of these conditions.

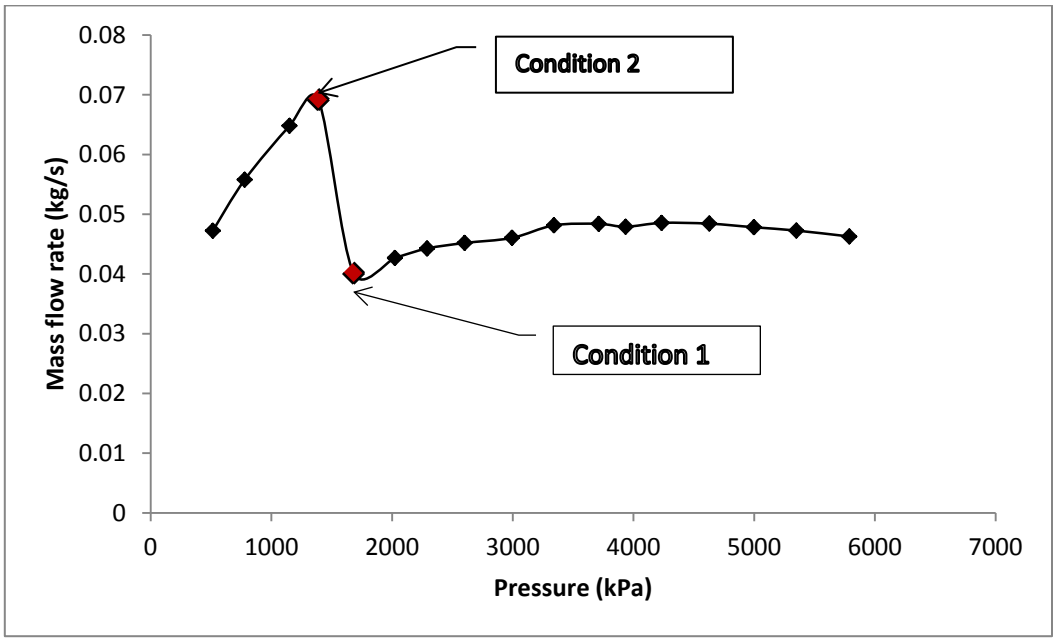

Figure 37 – Variation of the mass flow rate with ΔP indicating conditions for simulations

9.5 Results for simulation for ΔP = 1680 kPa (Condition 1)

Since the experiment was carried out by reducing the ΔP from the highest to the lowest value, it was proposed to simulate a condition (i.e. condition 1) before the occurrence of the jump in order to study the flow behavior here. Fig. 38 shows the variation of the vorticity contours with time for this case.

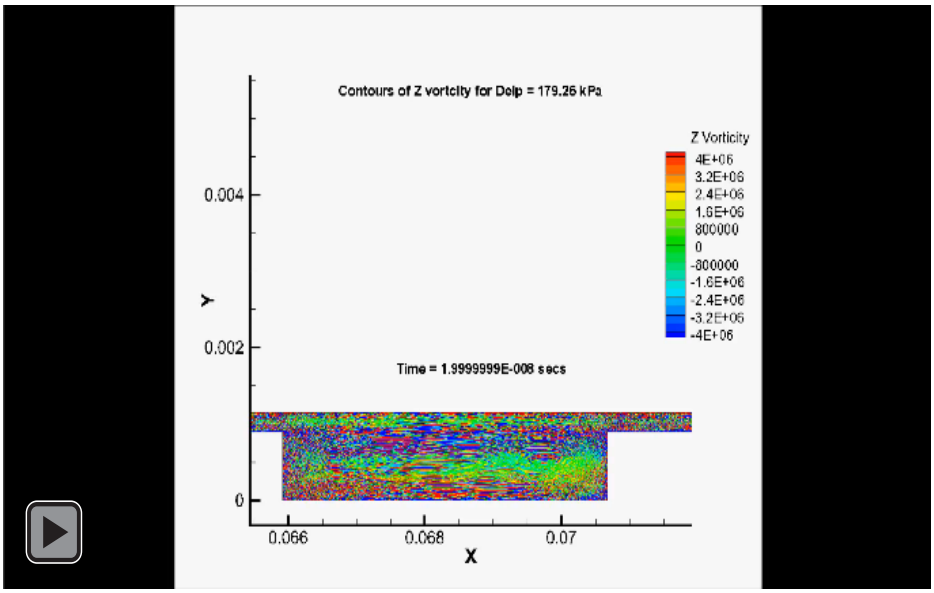

***Figure 38 – Variation of Z vorticity at* ΔP = 1680 kPa**

As seen in the simulation, as the upstream shear layer becomes unstable, vortices start shedding from the upstream corner of the cavity. This high frequency shedding is accompanied by the presence of a shear layer along the mouth of the cavity, which extends from the upstream corner to the downstream corner. Although the size of the vortices generated is smaller, the trend in vortex shedding resembles that of the shear layer instability. In addition to the conventional mode of shedding seen in this instability, a layer of counter vorticity is formed along the top boundary of the cavity and starts shedding vortices after a few flow through times have passed. These vortices then develop large enough to influence the already formed shear layer along the top of the cavity and also interact with the downstream edge where *partial clipping* occurs.

As is characteristic of the shear layer instability, the vortices generated and shed from the upstream edge against the downstream wall are clearly captured. Fig. 39 shows the onset and development of this instability as seen close to the upstream lip of the cavity.

The first figure, 39(a), shows the development of a crest in the shear layer at the upstream edge, which indicates the onset of the instability. The next figure in the sequence shows the roll-up of this shear layer into a mature vortex. A snapshot of the pressure contours at the same time step indicates pressure maxima at the cavity corner under the vortex and a pressure minima right in front of it (Fig 39(c)). This distribution is seen to be strongly indicative of periodic variations of the surface vorticity production, which is again characteristic of the shear layer instability [41].

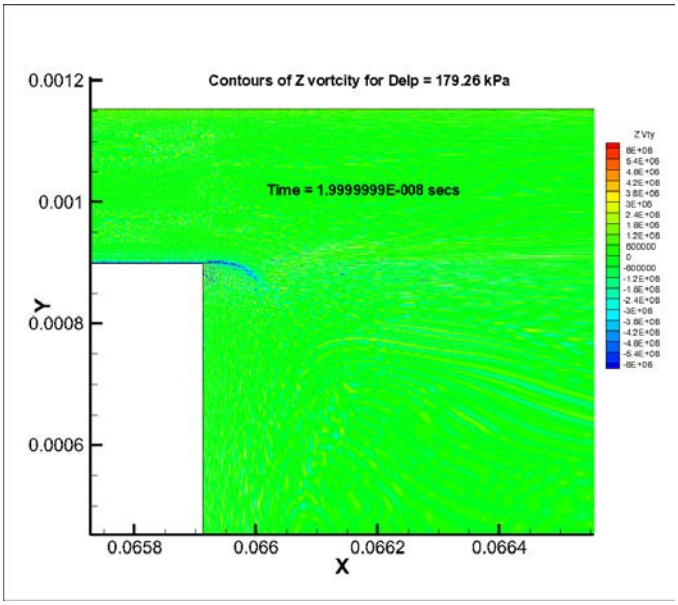

(a)

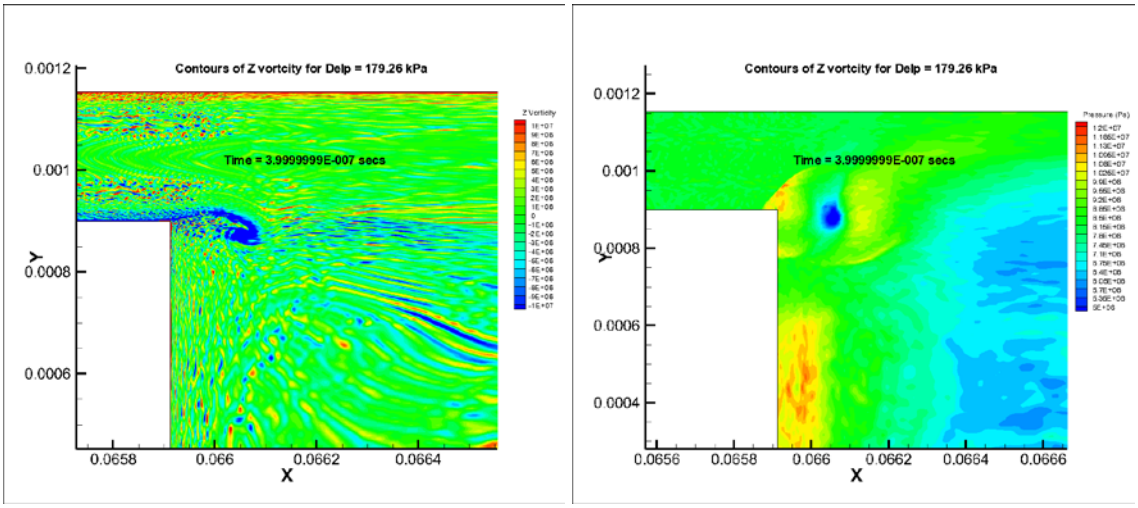

(b) *(c)*

Figure 39 – Close-up of Z vorticity contours at upstream cavity edge showing (a) onset of instability (b) roll-up of shear layer (c) pressure contours showing roll-up of shear layer

Though the presence of the shear layer instability is fairly apparent at this point, there are basic differences from the conventional nature of this instability owing to the presence of the top boundary. One major difference is that the shedding frequency is seen to be higher than that of the cavity without the top boundary. This is reinforced by Fig. 40 that shows the wavelength computation for this case as compared to that of the shear layer instability

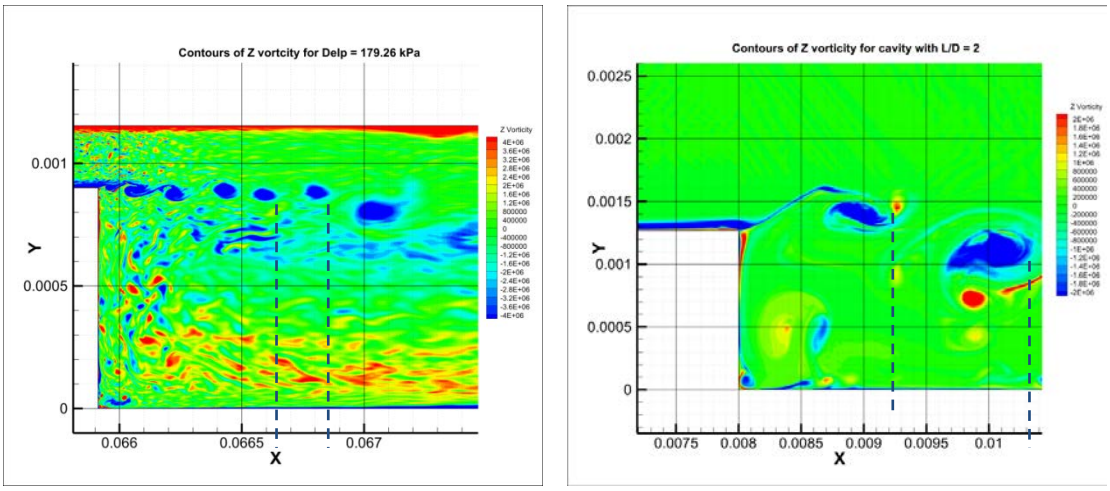

Figure 40 – Computation of wavelength for present case and for the original domain without the influence of the top boundary

The ratio of the wavelength to cavity length (which is a standard non-dimensionalization measure in this case) for initial domain, without a top boundary is 4.09 while the same value for this case is seen to be 0.59. This shows that the presence of the top boundary indeed influences the occurrence of the instability and also causes the instability to be better defined. Further, the ratio of the length of the cavity to the momentum thickness upstream of the edge was found to be 303.48 which is of the order of that seen for instabilities in open cavities by Rowley [19]. The convective speed of the vortices (before pairing) as determined from the simulation, was found to be around 216 m/s for this case and the free stream velocity was 308 m/s.

With regard to the vortices being shed from the upstream edge, closer examination of the vortex motion shows vortex pairing (where pairing is described by two adjacent vortices rotating around each other leading to possible amalgamation into one large structure). Although this phenomenon is less identifiable than in a free mixing layer, the occurrence is still detectable and is indicative of secondary instabilities in the flow. As indicated by Fig. 41, for every two vortices that show pairing, the next vortex skips pairing and is again followed by two vortex pairs. This is in line with the behavior seen by Moon and Wiedman [38] who documented this intermittent nature of vortex pairing and coined the term *dropout* vortices for the odd, unpaired vortices. This sequence of pairing is similar to that seen in unbounded 2-D mixing layers when excited by a random noise (Fig 41(b)), which indicates that there are multiple excitation frequencies present in the incoming flow. Vortex pairing, in general, is also seen to be

indicative of a subharmonic disturbance interacting with a fundamental frequency, in case of free shear layer [38].

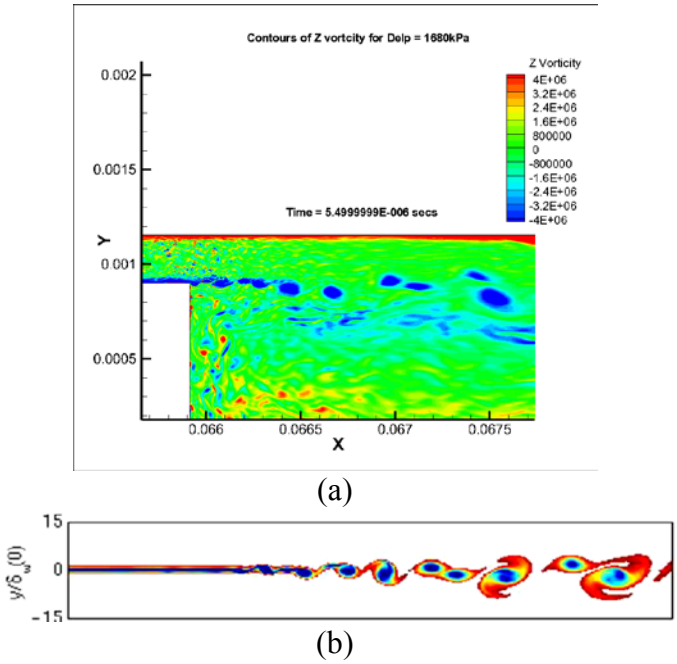

Figure 41 – (a) Vorticity contours showing vortex pairing in the cavity (b) Vortex pairing seen during the excitation of unbounded 2-D mixing layer with random noise [42]

Another difference seen is that in comparison with the vortex pairing occurring at the upstream lip in the case without the top boundary, the present case shows is a region of high counter vorticity in the shear layer along the top boundary of the cavity. This region develops along the length of the cavity in time and starting at 2.5 times the flow

through time, counter rotating vortices are shed from this layer (as shown in Fig. 42). The two shear layers (bounded and unbounded) interact by synchronizing their motion - the shedding frequency of the bounded shear layer is however seen to be lower than that of the free shear layer. Upon comparison, it is seen that the frequency of shedding of the bounded shear layer corresponds to the movement of the coalesced vortices (formed by vortex pairing) traveling along the free shear layer (Fig. 42(b)). Another observation, as made earlier is that the formation of this layer influences the transport of vortices shed from the upstream lip and also interacts with the downstream edge causing *partial clipping* (Fig. 42 (c)).

At this point it is useful to recall the concept of *jitter* which refers to the changes in the method of impingement (i.e. type of *clipping* of the structures) at the downstream edge. As mentioned earlier, the occurrence of *jitter* has been seen to introduce intermittency between instability modes and this is indicated by the presence of low frequency components in the flow. Another relevant implication of this phenomenon is that the absence or presence of *jitter* determines the changes in the feedback to the upstream edge which again translates to a variation of the instability mode.

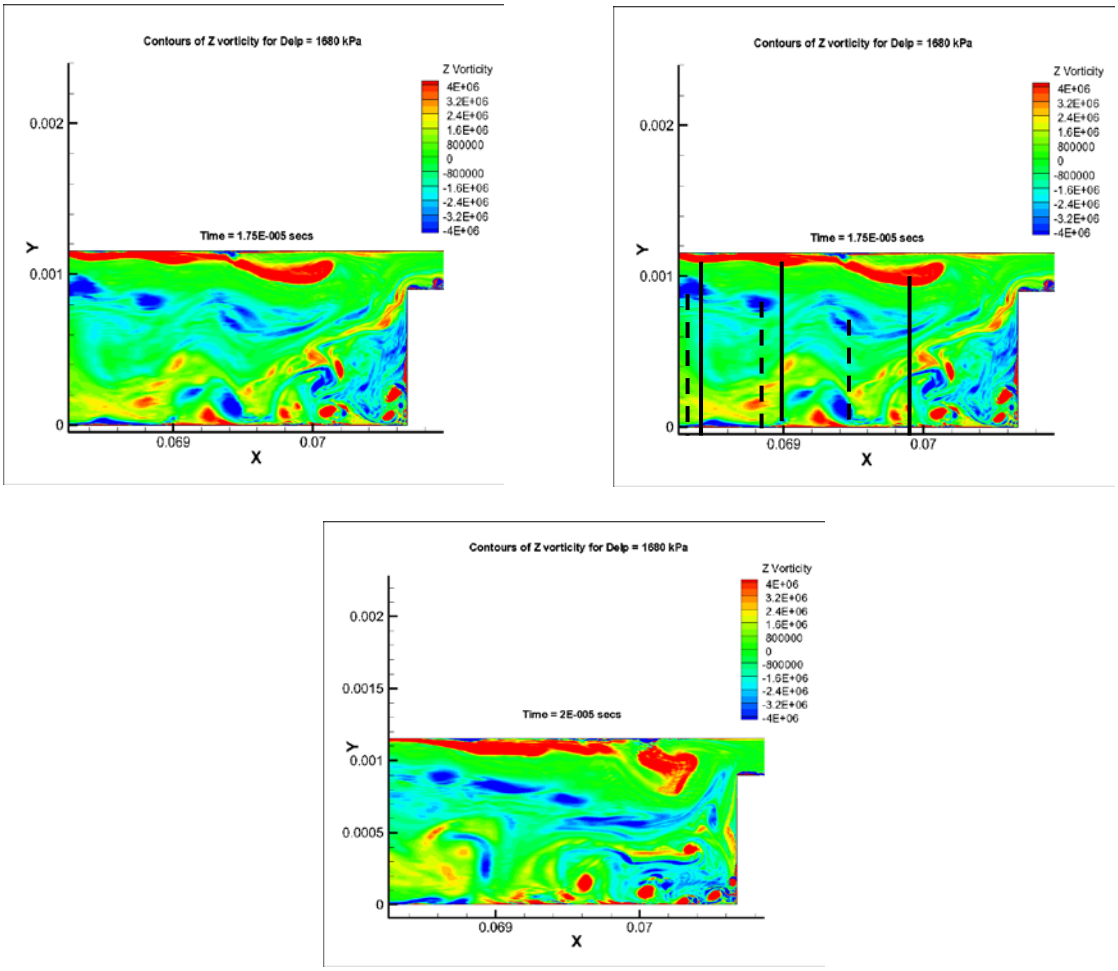

Figure 42– Vorticity contours showing the generation of counter vorticity at the top boundary of the cavity

Another effect of the top boundary is seen in the fact that the vortices formed in this case start to quickly lose their energy and dissipate before they reach the downstream lip of the cavity. Although this does not allow for a strict classification of the vortex-edge interaction mechanism by the terminology of Rockwell and Kinsely [40], the effect of the disturbance propagation and feedback is still apparent in terms of the shedding of vortices along the downstream wall.

Fig. 43 shows the vorticity contours superposed with the streamlines of the flow. The streamlines shown are comparable to those seen for the open cavity without the top boundary, with the shear layer instability. Both cases show the formation and transport of vortices along the top half of the cavity, the streamlines clearly showing that the influence of these vortices does not extend through the entire depth of the cavity. In addition to these structures, the streamlines further in time show the result of the feedback mechanism – vortices generated from the downstream wall are seen to make their way upstream along the bottom half of the cavity. All of these qualitative comparisons indicate that the type of instability seen in this case is indicative of the shear layer instability seen in open cavities apart from additional effects due to the presence of the top boundary.

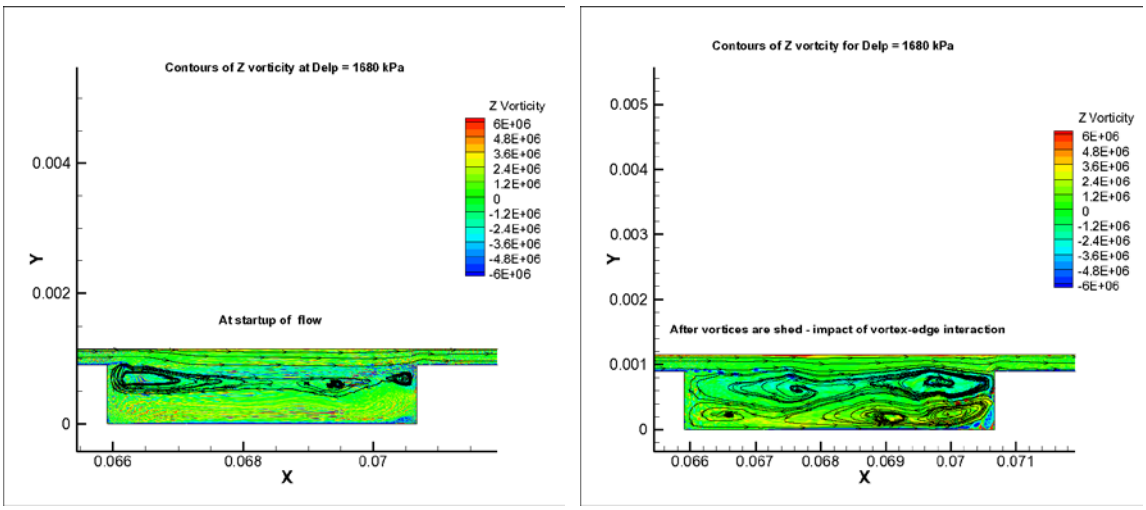

Figure 43 – Vorticity contours superposed with streamlines showing the formation and transport of generated vortices

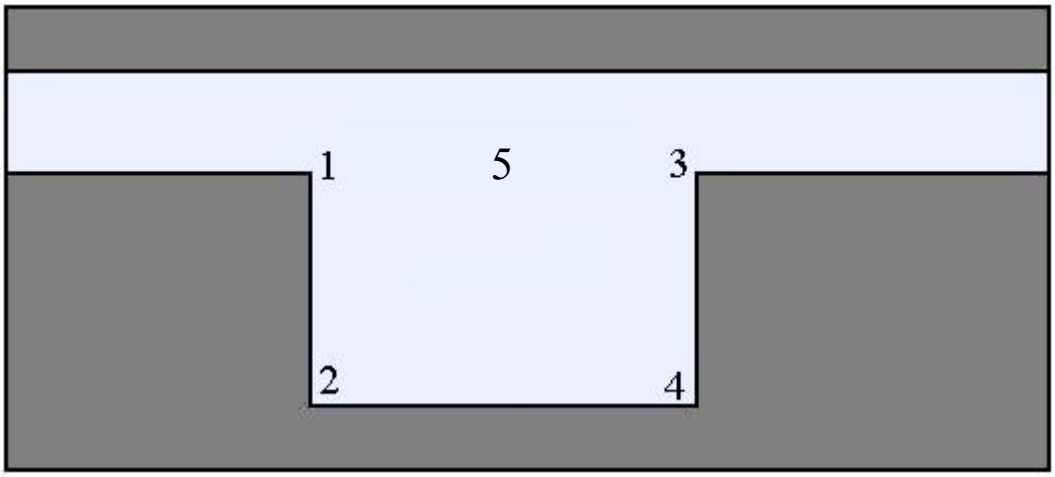

Figure 44 – Layout of cavity showing locations at which data was analyzed

In order to obtain a quantitative description of the flow, spectral analysis of the CFD data was carried out. For this purpose, it was decided to select two points in the cavity – one at the upstream lip and the other at the downstream lip (i.e. points ***1*** and ***3*** as shown in Fig. 44) and monitor the pressure variation at these two locations. The selection of these points was made based on trends seen in literature and observation of the fluid motion in the cavity. Fig. 45 (a) shows the FFT of the pressure distribution at point ***1.*** As seen from the plot, there is a broad peak of the variation centered at about 8.5 kHz, indicating the highest amount of energy is present in this frequency range. Although the presence of a broad peak could be indicative of the need for different windowing function, it was seen that application of different windowing functions retained the general nature of the peak. This helped establish that the nature of the distribution was a result of the flow itself and not a function of the signal processing technique.

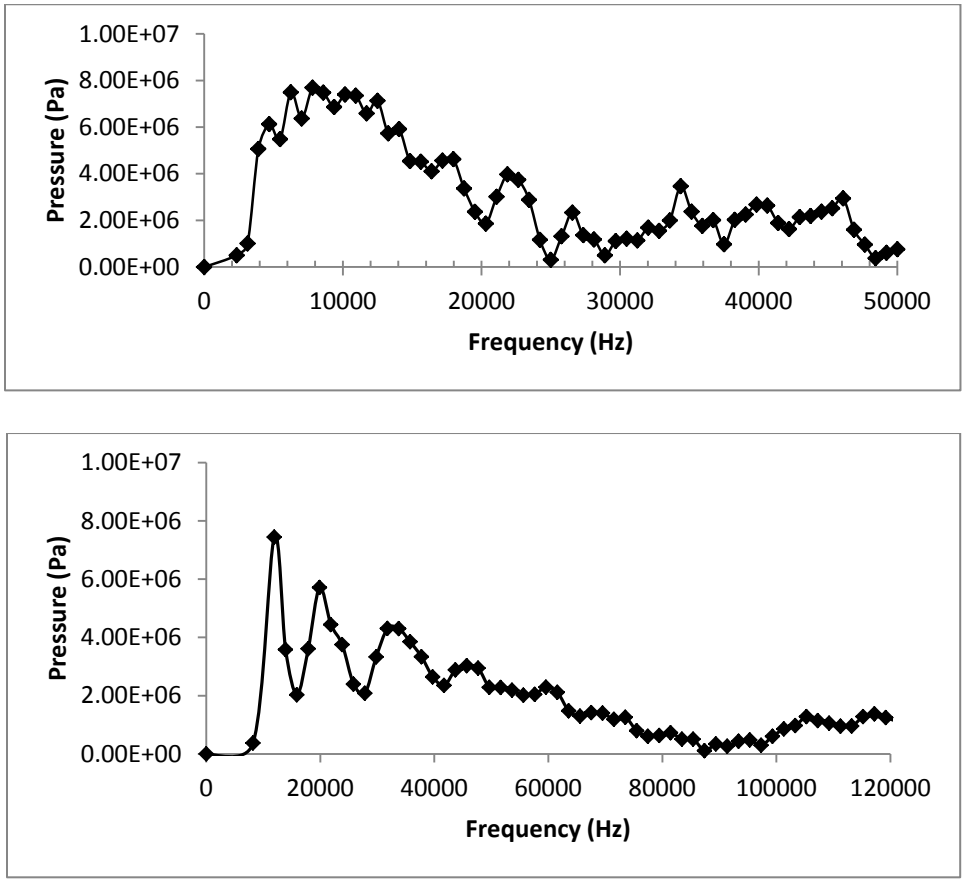

Figure 45(a) FFT of pressure distribution at the upstream lip of the cavity and (b) at the downstream lip of the cavity

Fig. 45(b) shows the FFT for point ***3***, located at the downstream lip of the cavity. This distribution shows a different trend than the one seen at the upstream point – there are multiple, sharp peaks seen with the dominant one at 11500 Hz. These subdominant peaks are located at harmonics of the fundamental frequency (i.e. at 23000 Hz and at 34,500Hz) indicating the presence of non-linear interactions in the flow. This

distribution also shows the effect of the multiple mechanisms occurring at the downstream lip i.e. the vortex impingement from upstream vortices, propagation of upstream disturbances and shedding along the downstream wall.

Further, the value of the dominant mode frequency is also in agreement with that seen from experimental data where the dominant frequency for this mode was seen as 12000 Hz. Further, the convective velocity can also be computed using the formula –

$$C_{ph} = \lambda f \tag{31}$$

Where C_{ph} is the convective speed, f is the dominant frequency and λ is the wavelength. Using the value of the dominant frequency as 11500 Hz and the wavelength as determined earlier (i.e. λ/L = 0.59), the convection speed of the vortices was found to be 215 m/s. This reinforces the value that was obtained by observation in the earlier sections and allows for verification that the convective speed is around 0.7 times the free stream velocity.

Looking at Figs. 45 (a) and (b) allows for the hypothesis that there is broad spectrum turbulence present upstream of the cavity which is seen as the broad peak in Fig. 45(a). The energy present in this mature, broad spectrum is then transferred to the mixing layer at the mouth of the cavity where the interaction with the upstream edge and the feedback loop allows for the amplification of select frequencies. This is represented by Fig. 45 (b) that shows distinct peaks at these limited frequencies.

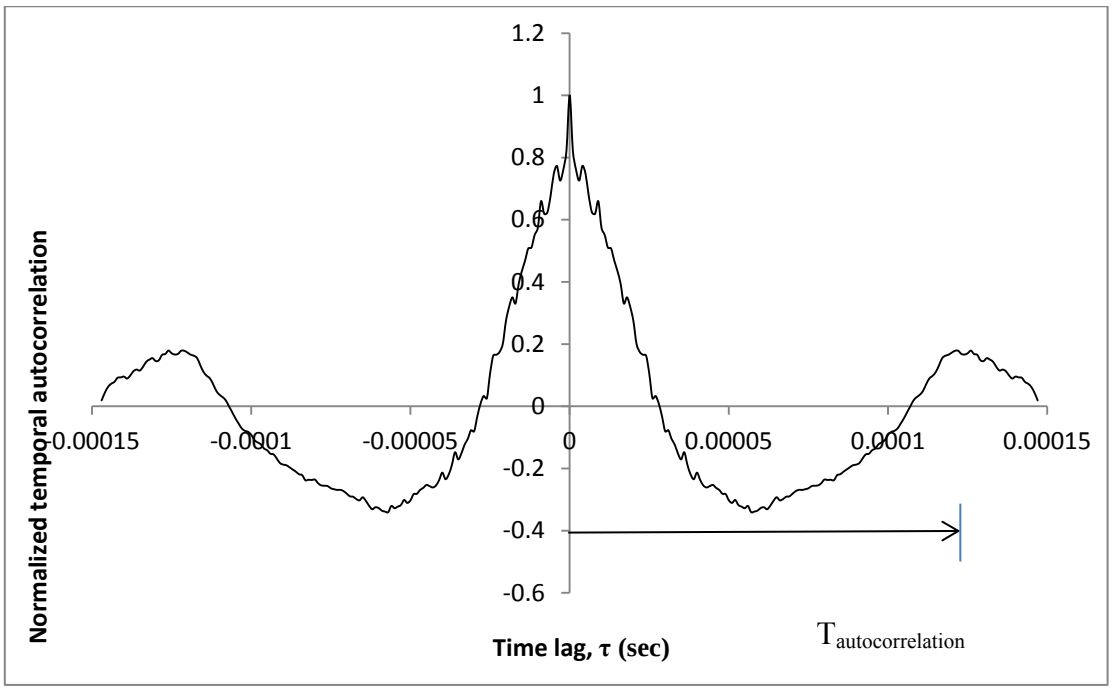

Figure 46 Temporal Auto-correlation of signal from upstream corner of the cavity

The next type of analysis carried out was a temporal autocorrelation of the pressure signal at the upstream point. This was done in order obtain more information about the nature of the signal and to better characterize it. The correlation was calculated and normalized using the following formula –

$$R\,(\tau) = \frac{\overline{P(t)P(t+\tau)}}{\overline{P(t)P(t)}} \tag{32}$$

where P(t) is the transient signal at time t and τ is the time lag or time advance. The plot obtained is typical for a turbulent quantity in a statistically stable flow [42] and has a

single hump at a zero time lag. The trend shows a high correlation at lag close to zero and starts decreasing until it shows a negative autocorrelation and the opposite trend is repeated. This kind of a pattern is a signature of a strong autocorrelation which indicates that a predictive model could be applied for this data. Closer observation near the peak also indicates that it is only about 15% of the signal that shows a strong correlation over one time period. Further, the time period of the correlation (defined as shown in Fig. 46) is seen to be 0.000125 secs indicating the corresponding frequency to be 8000 Hz. This frequency is in line with that seen at the broad peak in Fig. 45 (a) and is a known characteristic of fully developed turbulence.

A similar analysis carried out at the downstream point showed the same variation of the correlation coefficient hence confirming that the flow is indeed statistically stable and turbulent.

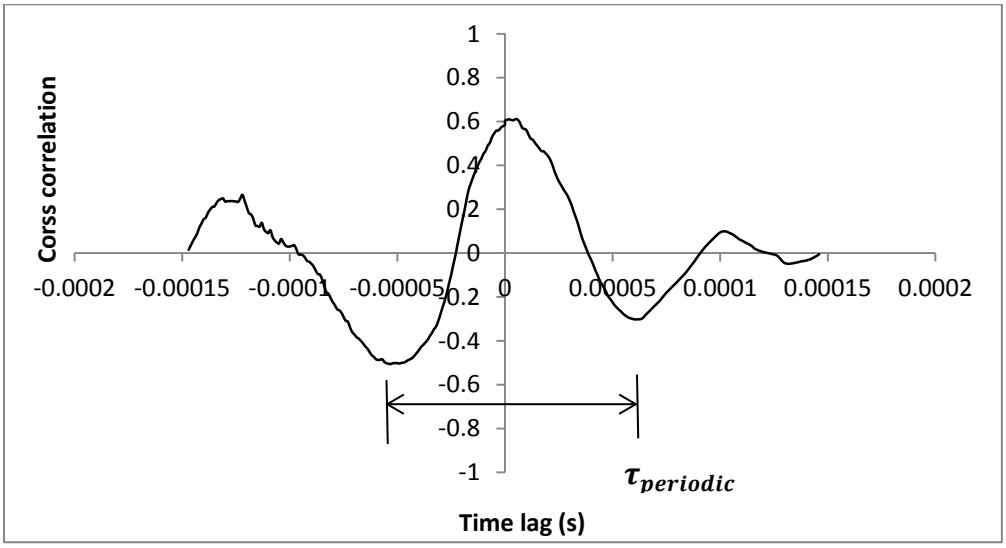

Figure 47 Cross-correlation of signal from upstream and downstream corners of the cavity

For further analysis of the obtained data, a temporal cross-correlation between the two signals was carried out using the following formula –

$$R_{13}(\tau) = \frac{\overline{P_1(t)P_3(t+\tau)}}{\overline{P_1(t)P_3(t)}} \tag{33}$$

where $P_1(t)$ is the transient signal at the upstream edge (legend as in Fig. 32) at time t, $P_3(t)$ is the transient signal at the downstream edge at t and τ is the time lag . Fig. 47 shows the variation of the correlation coefficient, R_τ with τ; the trend of the plot indicates the presence of a periodicity between the two signals, with $\tau_{periodic}$ representing the period of the variation. Computing the acoustic speed (i.e. speed at M =

1) to be 346.72 m/s , and using this to compute the time taken by a vortex to travel from point ***1*** to ***3*** –

$t_{travel} = 9.76\ e-7\ secs$

As seen from the cross correlation plot, the two signals are in phase (i.e show the highest correlation) close to $= 0$, and on closer inspection, this peak is found to be at 1e-6 secs. Taking into account the uncertainty in temperature computation (since the temperature is used to compute the acoustic speed), it is seen that this plot thus confirms the hypothesis of the acoustic feedback mechanism that drives the shear layer instability.

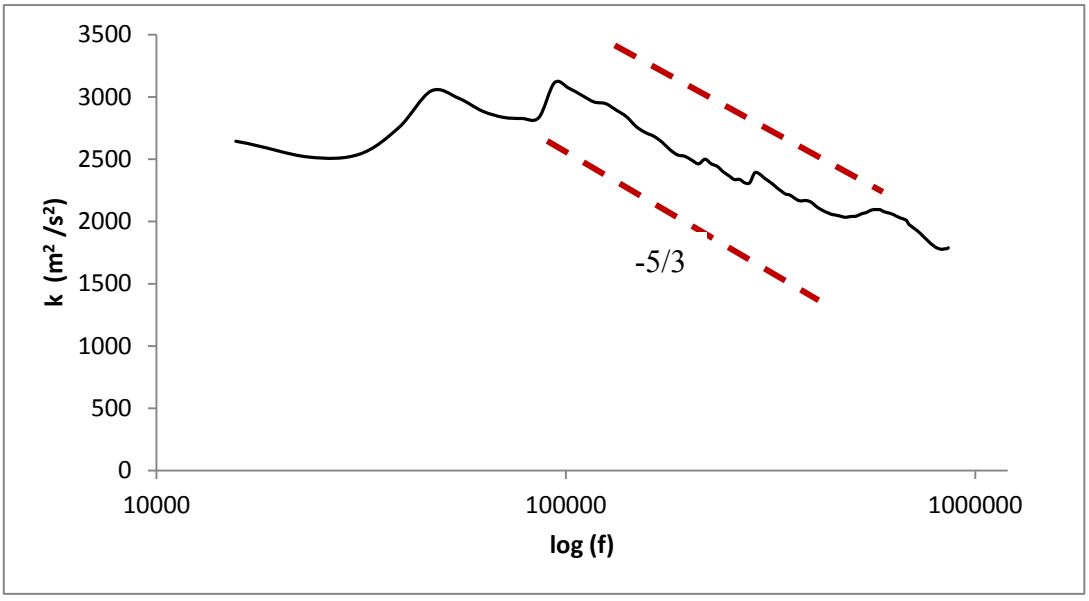

Figure 48 Spectrum of turbulent kinetic energy at point 5

To quantitatively ensure that the LES was indeed capturing the large scales of the flow, it was also decided to compute the power spectral density, defined using the autocorrelation as –

$$S(f) = 4\int_0^\infty R(\tau)\, e^{-2\pi i f \tau}\ d\tau \tag{34}$$

This was done at a point midway along the top boundary, i.e point 5 from the legend. As seen from Fig. 48, which is a semi-log plot of the turbulent kinetic energy, the large scales of the flow are indeed captured. Also, the two dashed red lines indicate the -5/3 slope as predicted by Kolmogorov to define the inertial range and the data is in fair agreement with this theoretical prediction.

9.6 Results for simulation for ΔP = 131 kPa

Fig. 49 shows the variation of Z vorticity contours with time for the case at the peak of the jump, i.e. where the mass flow rate was maximum. Initial activity shows the shear layer shedding vortices from the upstream lip, as seen in the previous case. However, with time, the nature of the shedding is seen to be distinctly different from the shear layer instability. The first difference is seen with regard to the development and shedding of counter-rotating vortices from the top boundary of the cavity – this, unlike the previous case, the top boundary has a greater influence on the flow behavior even at the initial flow-through times.

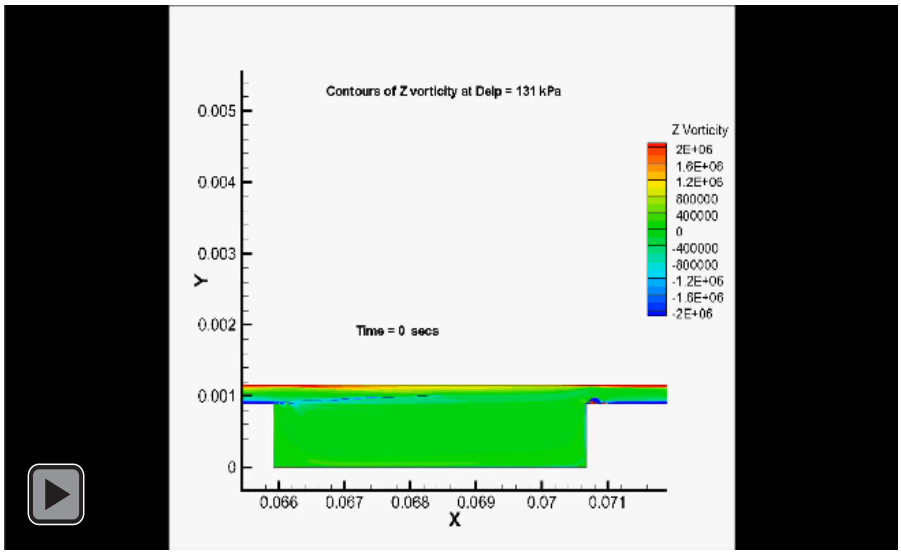

***Figure 49 – Variation of Z vorticity at* ΔP = 131 kPa**

Further in time, the region of high vorticity at the top boundary starts to shed vortices at seemingly the same frequency as the upstream edge. This causes counter rotating vortex pairs to be formed (the occurrence of counter rotating vortex pairs as been seen in a range of flows, such as wakes of airfoils [43] but a detailed stability analysis of this phenomenon itself is beyond the scope of the present study). Fig. 50 shows the vortex shedding after multiple cycles and helps quantitatively compare the wavelength between the counter rotating vortices. Using the same non-dimensionalization as earlier, the ratio of this wavelength to the cavity length is seen to be 0.178 for the clockwise vortices and 0.188 for the counter clockwise vortices. This supports that the frequencies of shedding are almost the same for both cases and also allows for the formation of the vortex pairs.

Comparing this wavelength with what was obtained for the previous case (which was 0.59) shows that the shedding frequency of the free shear layer is higher in the present case than in the previous case. The convective velocity (computed as before) is also seen to be lower for this case and was found to be 103.42 m/s (which was around 0.62 times the free stream velocity). Also, as computed for the previous case the ratio L/θ_0 for this case was seen to be 100.57 confirming a change in the behavior of the incoming flow.

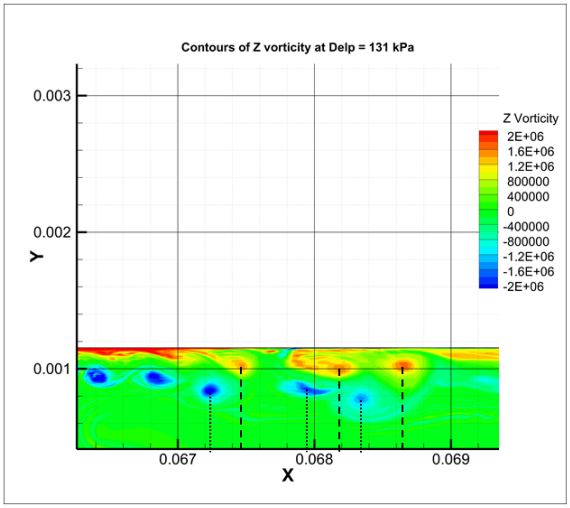

Figure 50 Computation of wavelength for present case with ΔP = 131 kPa

Another observation that can be made from the simulation is that although the vortex pairs initially travel along the top edge of the cavity without extending into the depth, as the flow through time increases, the presence of a large recirculation zone

becomes clear. The vortex pairs follow the streamlines created by the zone, and travel along its path, deep into the cavity until they dissipate. Any pairs that still have a strong core by the time they reach the downstream edge are seen to be forced out of the cavity. Again, this behavior is reminiscent of the wake mode instability the difference being that the top boundary causes the expulsion to be more subdued. The evolution of this entire process corresponds with the development of the wake mode instability seen in open cavities [40] where the occurrence of the wake mode was always preceded by the shear layer instability. There is however a departure from the conventional nature of this instability as seen in open cavity flows. Comparing the values of the L/θ_0 ratio, the present condition shows a lower value of this ratio than that seen for the shear layer instability, wherein the opposite trend was seen in cases without the top boundary.

Fig. 51 shows a close-up of the upstream edge during the formation and shedding of a vortex - both the pressure and vorticity contours are shown so as to enable a similar analysis as in the previous case. Studying the vorticity contours during the formation of the vortex (Fig. 51 (a)) shows the crest in the shear layer - though discernible, this crest behaves differently from that seen earlier, in that the roll-up of the shear layer is more subdued. This is another indication of the fact that the top boundary of the cavity has a greater effect on the vortex formation and shedding in this case. The corresponding pressure contours are visibly different from that seen in the previous case; while the former showed distinct pressure maxima under the core of the forming vortex, the current case does not show one. Additionally, a pressure minimum in front of the vortex

is missing as well, confirming that this type of vortex shedding and formation does not indicate the presence of the shear layer instability.

The overall pressure variation is also significantly lower than that seen in the previous case – while the range of variation was around 7000 kPa in that case, it is limited to around 1500 kPa now. This trend coupled with the vorticity ranges indicate that the strength of the vortices being shed is not as high in this case as in the previous one. With time, as the vortex detaches itself from the shear layer (Fig. 51(c)), there is a significant change in the pressure distribution (Fig 51(d)) in that a large pressure maxima dominates the region just under the upstream lip. The shape and variation of pressure within this maxima is consistent with the formation of a recirculation zone. Further, the influence of the vortex being shed is seen to extend as a minima through the clearance region above the cavity, unlike the previous case where the activity was confined along the top edge of the cavity

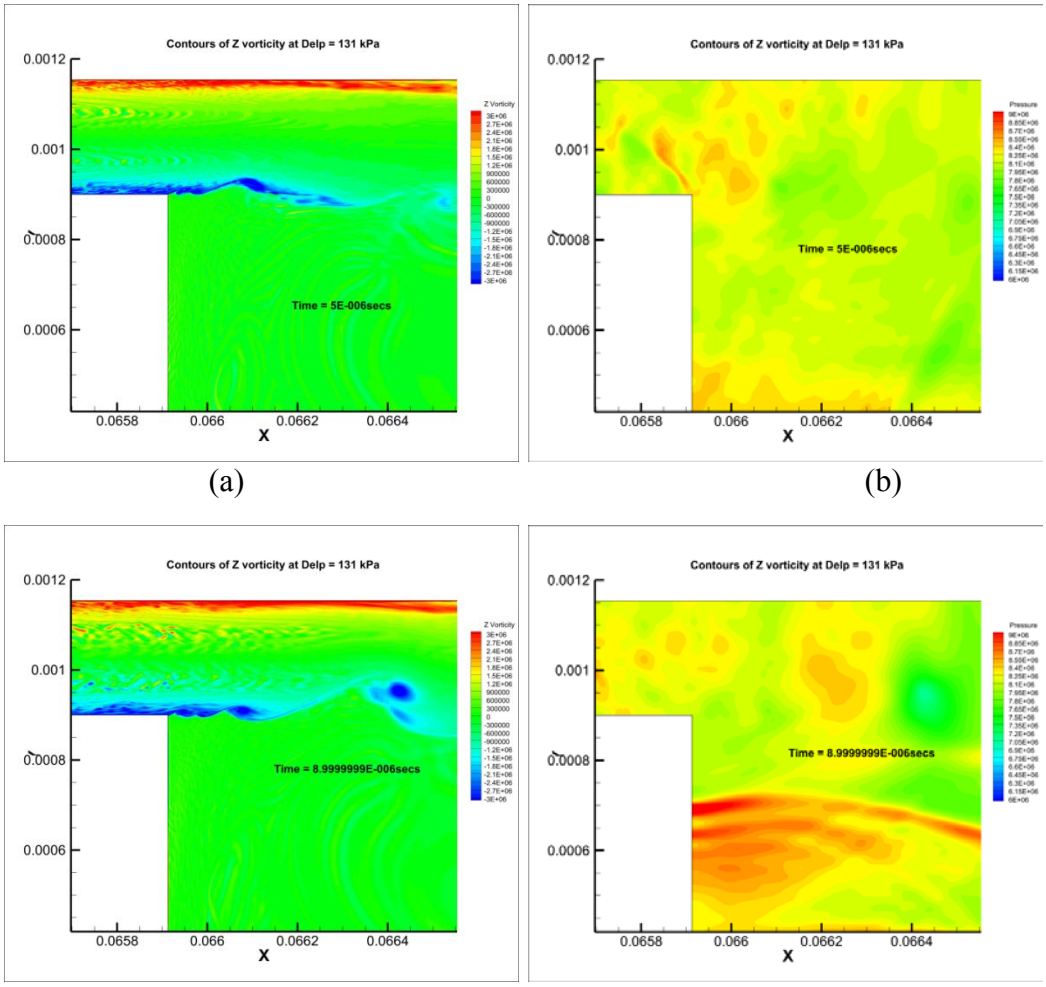

(a) (b)

(c) (d)

Figure 51(a), (b) - Vorticity and Pressure contours showing formation of crest for the case with ΔP = 131 kPa ,(c),(d) Vorticity and Pressure contours showing detachment of vortex from shear layer at ΔP = 131 kPa

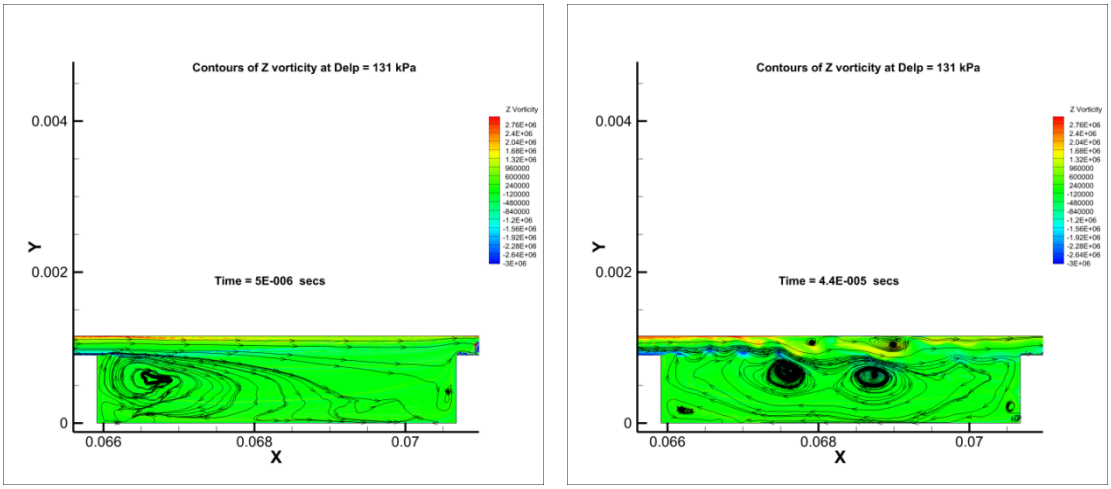

Figure 52 – Vorticity contours superposed with streamlines showing the formation and transport of generated vortices

The streamlines seen in Fig. 52 corroborate the wake mode like behavior of the present case. As seen in the first time capture (showing the Z vorticity with the streamlines superposed on it), the formation of a vortex comprises streamlines that extend throughout the depth of the cavity. The dimensions of the structure being formed are comparable to the dimensions of the cavity itself and it can be recalled that this is defined as an identifying characteristic of the wake mode instability. There are no other structures forming anywhere else in the cavity which again points to the presence of a strong recirculation due to this vortex. The second plot in sequence shows the streamlines at a time after one vortex that has been shed is still traveling towards the downstream edge, and a second one is shed right behind it. It is also seen that both

vortices maintain similar dimensional characteristics though there is no coalescing of the structures.

As in case of the previous flow condition, spectral analysis was carried out for the present case as well. The same legend from Fig. 45 is used in order to describe the location of the points and as in the previous case, points ***1*** and ***3*** were used for this part of the analysis. Fig. 53 shows the FFT of the pressure distribution at points ***1*** and ***3*** respectively. As seen here, the distribution at point ***1*** indicates the presence of a fairly uniform flow with no distinct dominant frequency components. The basic observation that can be made, however, is that the frequency range of the components is an order of magnitude higher than that seen in case of the shear layer instability. The second distribution at point ***3*** allows for the determination of dominant and subdominant frequency modes. The main dominant mode that was seen in experimental data at 183 kHz is captured in 185 kHz and is slightly over predicted. In addition to this, the subdominant mode at 61 kHz is also captured at 63 kHz. The CFD data also allows for the capture of a third peak at 400 kHz which was unable to be detected by the experimental setup (this was owing to the fact that the maximum frequency of the transducers was 250 kHz).

The spectra therefore confirm the presence of a change in the instability mode between this case and the previous case. While the present case is reminiscent of a wake mode (although the presence of the top boundary significantly alters the mechanism of the instability), the previous case behaves as a shear layer instability. It is therefore seen

that there is indeed a change in the behavior of the flow itself over the occurrence of the jump and this is corroborated by both experimental and numerical data.

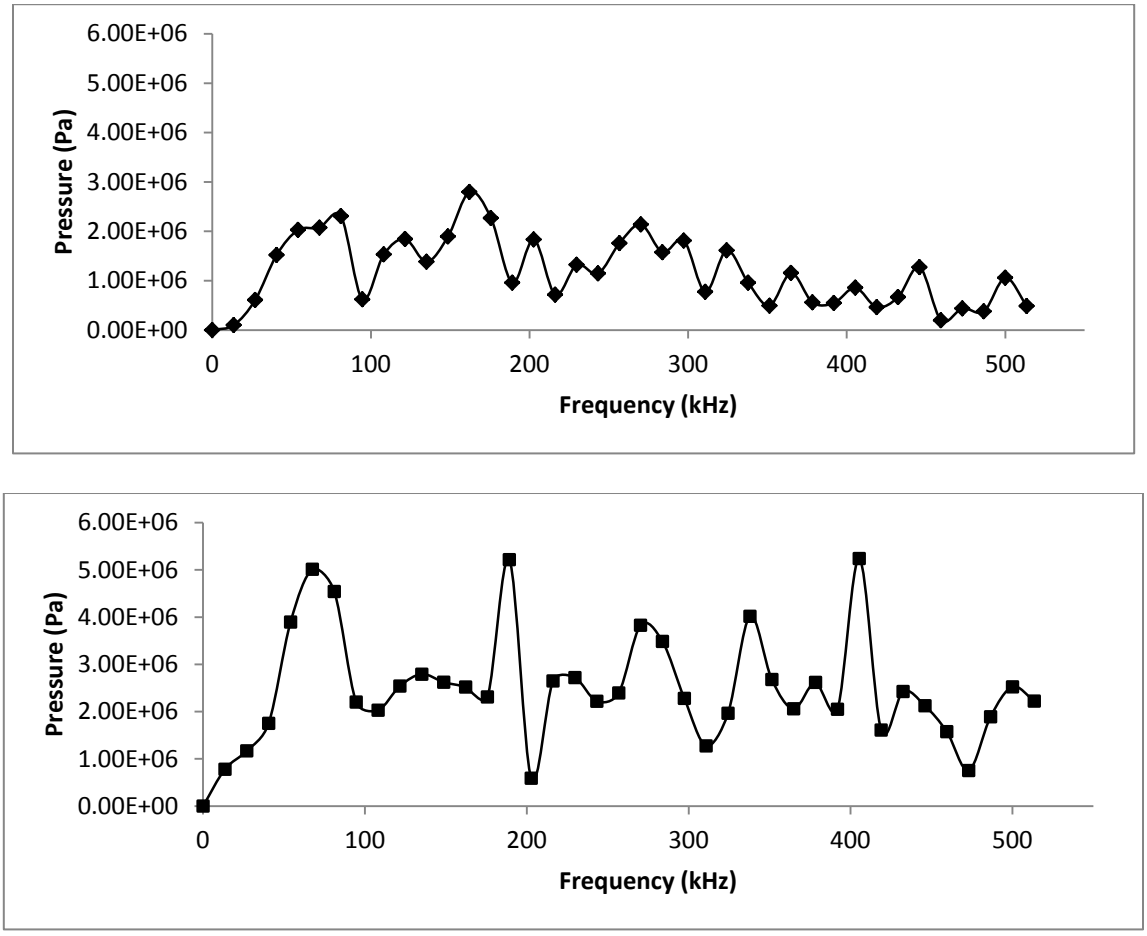

Figure 53(a) FFT of pressure distribution at the upstream lip of the cavity and (b) at the downstream lip of the cavity

As for the previous pressure difference, a temporal cross correlation between these two signals was done in this case as well and the results are as shown in Fig. 54. The variation of the correlation coefficient, R_τ with τ again indicates the presence of a periodicity between the two signals, with $\tau_{periodic}$ representing the period of the variation. Unlike the previous case, the lag at the peak seen here does not correspond with the acoustic speed computation, supporting the fact that the wake mode does not show an acoustic feedback loop. The value of $\tau_{periodic}$ also varies from 0.0001113 secs in the previous case to 0.0000863 secs for the present case.

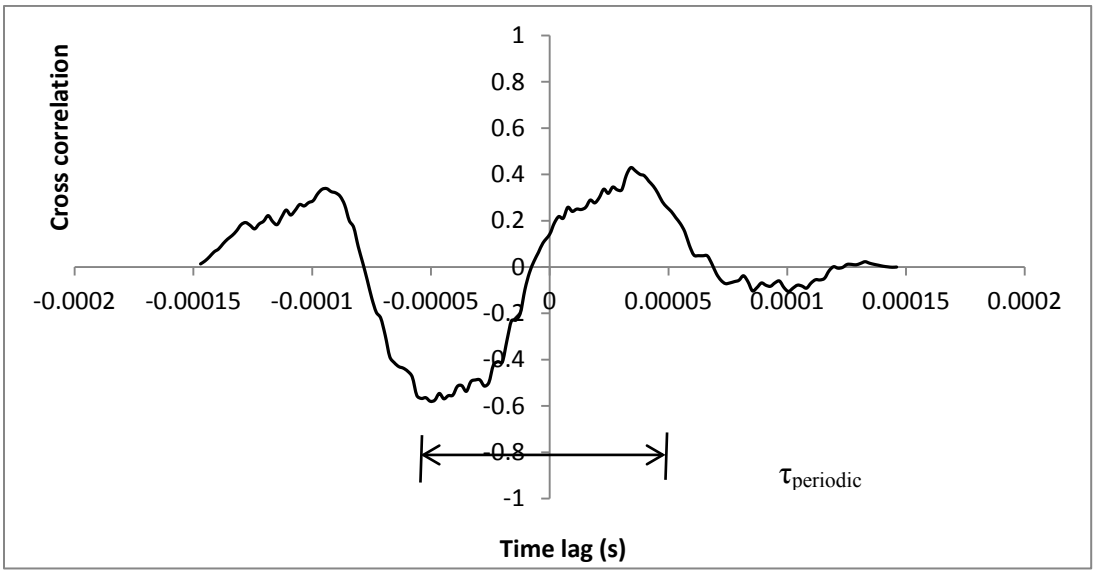

Figure 54 Cross-correlation of signal from upstream and downstream corners of the cavity for ΔP = 131 kPa

In order to obtain a better idea of the motion of the structures in the cavity, a more detailed analysis was carried out by obtaining the spectra at five other points along the mouth of the cavity. The legend is as shown Fig. 55 where ***a, b, c, d*** and ***e*** are all equally spaced along the mouth of the cavity.

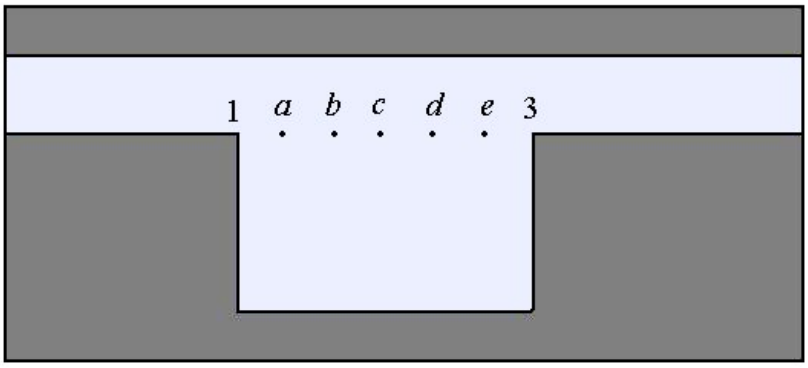

Figure 55– Layout of cavity showing additional locations at which data was analyzed

Cross correlations among these data points were then carried out in order to study the trends better. The first plot from Fig.56, shows the temporal cross correlation of the X velocity component between points **1** and **a, 1** and **b, 1** and **c, 1** and **d, 1** and **e,** and **1** and **3** for the case with a pressure difference of 1680kPa**.** This was done over all time steps, for both positive and negative time lags.

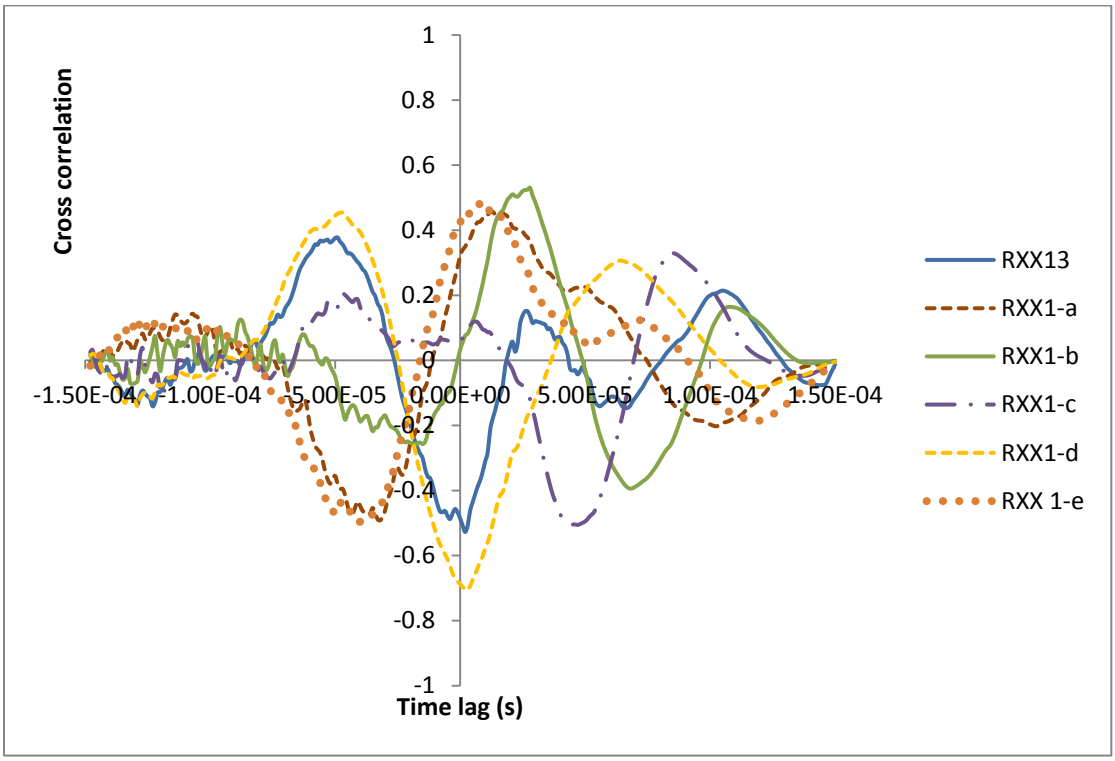

Figure 56 – Temporal correlation of X velocity for all points along the mouth of the cavity with point 1(ΔP = 1680 kPa)

As seen here the correlation between points **1** and **a** shows the highest value of correlation at -0.000034s indicating the presence of out of phase structures at this lag. This peak then shifts to a positive time tag of 0.000025 s for points **1-b and** moves to 0.000044 s for **1-c.** The trend is then reversed to the peak now moving closer to the zero lag, further away from the upstream edge – points **1-d** show a peak at 0.000006 s while

1-e shows a lag at 2e-6 s. Though the trend for the maximum correlation has been described here, the plot shows multiple peaks in addition to this maximum which confirms the presence of multiple length scales. This also allows for a quantitative verification of the vortex pairing phenomenon, leading to larger structures, as observed from the simulation.

A similar analysis was carried out for the case with ΔP = 131 kPa and the results are as shown in Fig 57. As seen here, the trends seen in this plot are distinctly different from that seen for the shear layer instability in Fig. 58. The maximum peak is always seen for negative time lags and is also seen to move over the mouth of the cavity indicating the motion of a large structure. The highest peak moves from -7.33e-5 s (at **1-a)** to -1.19 e-5 s (at **1-c**) and again starts to shift to higher lags of -4.8e-5 for both **1-d** and **1-e.** The presence of multiple length scales is also not indicated by the nature of the plot, thereby showing that this is indeed a different instability mode that what was seen earlier.

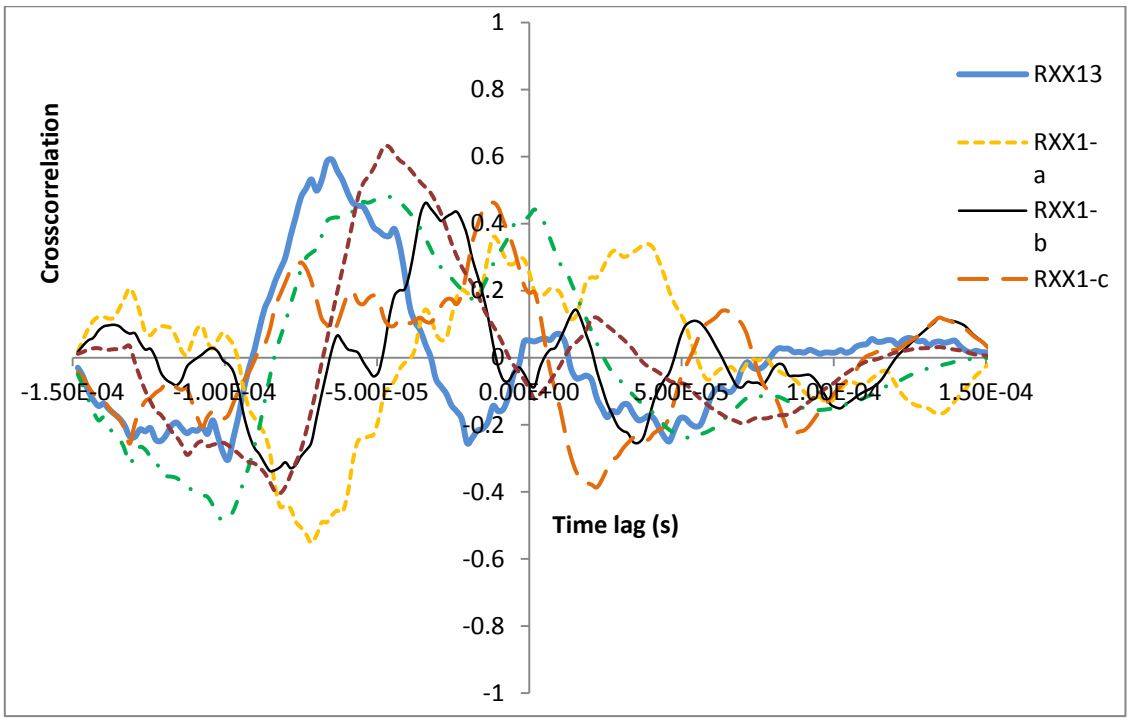

Figure 57– Temporal correlation of X velocity for all points along the mouth of the cavity with point 1 (ΔP = 131 kPa)

9.7. Comparison of results from experiment and simulations

In order to ensure the validity of the CFD results, a simple comparison of results was carried out with respect to the mass flow rates and the friction factor obtained by the experiment. Fig. 60 (a) shows the variation of mass flow rate with ΔP plotted along with the results obtained from CFD (black marker points).

The mass flow rate was obtained by a *direct reporting* method from Fluent while the friction factor was calculated using the expression for the Fanning friction factor as –

$$f_f = \frac{2\,\tau_f}{\rho\, v^2} \tag{35}$$

where τ_f is the wall shear stress.

As seen from Fig 58, both results therefore show good agreement with the experimental data showing a maximum deviation of 11% at ΔP = 131000 Pa. This therefore indicates that the CFD was indeed able to replicate the results seen in the experiment and that the 'jump' phenomenon was indicative of a flow related phenomenon rather than a function of the test facility.

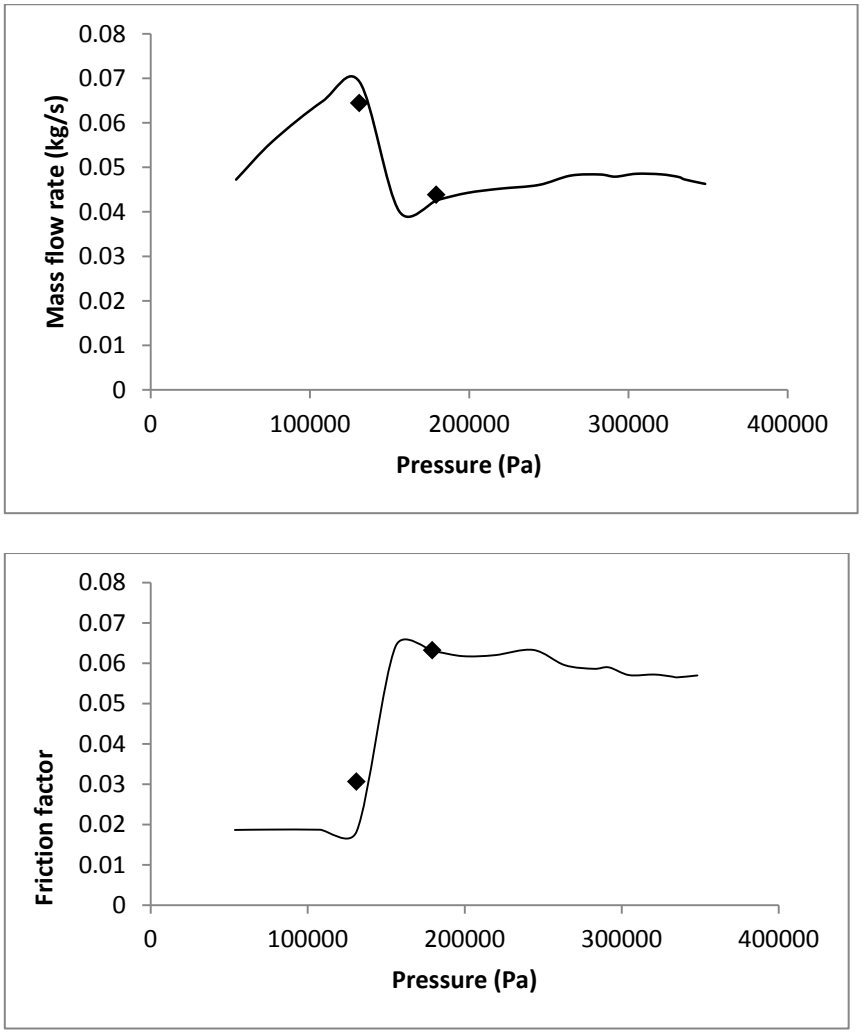

Figure 58 (a) – Variation of the mass flow rate with ΔP showing results of simulations (b) Variation of friction factor with ΔP showing results of simulations

10. CONCLUSIONS AND FUTURE WORK

A thorough investigation of the friction factor upset phenomenon seen in hole-pattern seals was carried out using both experimental and numerical means. A hole-pattern plate with a hole diameter of 3.175mm and hole depth of 0.9mm was tested against a smooth plate maintaining a clearance of 0.254 mm between the plates. In keeping with the method of testing used by Asiravatham[1], the pressure difference across the plates was reduced from 350 kPa to 50 kPa. Results showed a 'jump' in the friction factor at 131 Pa, recording a change in the friction factor by a factor of 3.5 (corresponding to a change in mass flow rate by about 1.7). Spectra taken over the range of conditions show a distinct change in the dominant frequency modes as well. The distribution before the jump indicates the presence of a large scale, low energy structures while the spectra after the jump showed the presence of multiple structures present at high frequencies through harmonics and sub harmonics of a fundamental frequency. This indicates a change in the flow instability modes over the jump which needs a deeper investigation.

In order to closely examine the nature of the flow over the cavities of the seal, it was decided to carry out CFD simulations of the problem domain. The first step for this part of the study was to determine a suitable method of simulation, which was done by recreating the results from Rowley's [19] DNS study of different instabilities in open cavity flow (i.e. cavities without the influence of a top boundary). Results from these simulations as compared to the DNS results allowed for a conclusion that LES via Fluent

is successfully able to capture the two expected types of instabilities in cavity flows – namely the shear layer instability and the wake mode. This was verified through both qualitative means (comparing the streamlines and structures in the flow) and quantitative means (comparison of Strouhal number and L/θ_0 ratio).

Upon arriving at a method of simulation, a domain was formulated to study the current geometry closely. Based on previous studies and to maximize computational efficiency, it was decided to simulate a single cavity using the pressure boundary conditions at the inlet and exit of the test section. Two conditions were chosen for simulation – one before and one at the jump and this was done in order to determine and compare any changes in the flow behavior. The results obtained showed good agreement with the mass flow rate and friction factor data from the experiment. Upon carrying out spectral analysis of the data, the existence of two distinct instability modes was confirmed – one with a shear mode like behavior which is enhanced by the presence of the top boundary and the other with a wake mode like behavior.

The shear mode reminiscent instability was seen before the occurrence of the jump and the presence of high frequency vortex shedding was confirmed via both qualitative observation and spectral analysis. The top boundary was seen to act as a mechanism for the instability to be better defined and the expected pairing pattern for vortices shed from the upstream edge was detected as well. Further, the presence of the top boundary influences the vortex-edge interaction at the downstream edge of the cavity which further encourages *jitter* and adds intermittency to the flow. The dominant frequency for the spectra was seen at 11.5 kHz and subdominant harmonics were at 23

kHz and at 34.5 kHz indicating the presence of vortex pairing and nonlinear interactions in the flow.

For the wake mode like behavior, the top boundary is seen to have more of an impact in and the vortex shedding frequency seen from the bounded and free shear layers are almost the same. This leads to the presence of counter rotating vortex pairs which then define the recirculation zone. Further, the dominant frequency is seen at 185 kHz with a subdominant mode at 63 kHz (both of which correspond to values obtained from the experiment). Studying the evolution of the flow and the spectra in conjunction allows for the verification of two distinct instability modes before and after the jump.

A combination of the experimental and CFD work therefore allowed for the explanation of the friction factor jump. The present study has, in essence, looked at understanding instabilities in flow through cavities with the effect of a top boundary and has seen how the conventional nature of the instabilities are modified as a result of the same. To obtain an even better understanding of the flow physics, one could extend the simulations to a three dimensional model and analyze the mechanisms of the instability. Another possibility of extending the work would be to carry out a parametric study by simulating different conditions and characterize the changes in instability modes based on the pressure drop and clearance of the channel. All of these extensive studies would help obtain a thorough understanding of flow instabilities in hole-pattern seals and therefore allow for better design and operational capabilities. .

REFERENCES

[1] Asirvatham, D.A., 2010, "Friction Factor Measurement, Analysis, and Modeling for Flat-Plates with 12.15 mm Diameter Hole-Pattern, Tested with Air at Different Clearances, Inlet Pressures, and Pressure Ratios," M.S. Thesis, Department of Mechanical Engineering, Texas A&M University, College Station, TX.

[2] Kheireddin, B.A., 2009, " Investigation of the Friction Factor Behavior for Flat Plate Tests of Smooth and Roughened Surfaces with Supply Pressures up to 84 Bars" . M.S. Thesis, Texas A&M University, College Station, TX.

[3] Ha, T.W., 1992, "Rotordynamic Analysis of Annular Honeycomb-Stator Turbulent Gas Seals Using Friction factor Model Based on Flat Plate Tests," PhD. Dissertation, Department of Mechanical Engineering, Texas A&M University, College Station, TX.

[4] Childs, D.W., and Moyer, D., 1985, "Vibrations Characteristics of the HPOTP (High Pressure Oxygen Turbo Pump) for the SSME (Space Shuttle Main Engine),"ASME Journal of Engineering for Gas Turbine and Power, **107**, no.1, pp. 152-159.

[5] Zeidan, F., Perez, R., and Stephenson, E., 1993, "The Use of Honeycomb Seals in Stabilizing Two Centrifugal Compressors," Proceedings of the Twenty-Second Turbomachinery Symposium, The Turbomachinery Laboratory, Texas A&M University, College Station, TX, pp. 3-15.

[6] Armstrong, J., and Perricone, F., 1996, "Turbine Instability Solution- Honeycomb Seals", Proceedings of the 25th Turbomachinery Symposium, Turbomachinery Laboratory, Texas A&M University, College Station, TX, pp. 47-56.

[7] Childs, D.W., and Yu, Z., 1988, "A Comparison of Experimental Rotordynamic Coefficients and Leakage Characteristics Between Hole-Pattern Gas Damper Seals and a Honeycomb Seal," Journal of Engineering for Gas Turbines and Power, **120**, pp. 778-783.

[8] Moody, L.F., 1944, "Friction Factors for Pipe Flow," Transactions of the American Society of Mechanical Engineers, **66**, pp.671-684.

[9] Ha, T.W., 1989, "Friction Factor Data for Flat-Plate Tests of Smooth and Honeycomb Surfaces," M.S. Thesis, Department of Mechanical Engineering, Texas A&M University, College Station, TX.

[10] Zeidan, F., Perez, R., and Stephenson, E., 1993, "The Use of Honeycomb Seals in Stabilizing Two Centrifugal Compressors," Proceedings of the Twenty-Second Turbomachinery Symposium, The Turbomachinery Laboratory, Texas A&M University, College Station, TX, pp. 3-15.

[11] Elrod, D., 1988, "Entrance and Exit Region Friction Factor Models for Annular Seal Analysis," PhD. Dissertation, Texas A&M University, College Station, TX.

[12] Thomas, J., 1992, "Determination of Variation of Friction Factor with Reynolds number for Flow between Two Closely Spaced Rough Plates," Senior Thesis, Texas A&M University, College Station, TX.

[13] Nava, D.L., 1993, "Observations of Friction factors for Various Roughness Patterns in Channel Flow," M.S. Thesis, Department of Mechanical Engineering, Texas A&M University, College Station, TX.

[14] Childs, D.W., and Fayolle, P., 1999, "Test Results for Liquid Damper Seals Using a Round-Hole Roughness Pattern for the Stators," ASME Journal of Tribology, **121**, pp. 42-49.

[15] Nayyar, P., 2005, "CFD Analysis of Transonic Turbulent Cavity Flows," PhD. Dissertation, University of Glasgow, Glasgow, Scotland.

[16] Rossiter, J.E., 1964, "Wind Tunnel Experiments on the Flow Over Rectangular Cavities at Subsonic and Transonic Speeds", R. &M. No. 3438, British A.R.C.

[17] Bres, G., 2007, "Numerical Simulations of Three-Dimensional Instabilities in Cavity Flows," PhD. Dissertation, California Institute of Technology, CA.

[18] Gharib, M. & Roshko, A., 1987, "The Effect of Flow Oscillations on Cavity Drag," Journal of Fluid Mechanics, **177**, pp.501-530.

[19] Rowley, C.W., Colonius, T., Basu, A.J., 2002, "On Self-Sustained Oscillations in Two-Dimensional Compressible Flow Over Rectangular Cavities", Journal of Fluid Mechanics, **455**, pp. 315-346.

[20] Larsson, J., Davidson, L., Olsson, M. & Eriksson, L. 2004 "Aeroacoustic Investigation of an Open Cavity at Low Mach Number," AIAA Journal, **42**, no.12, pp. 2462-2473

[21] Shieh, C. M. & Morris, P. J., 2000, "Parallel Computational Aeroacoustic Simulation of Turbulent Subsonic Cavity Flow," AIAA Paper 2000-1914.

[22] Suponitsky, V., Avital, E. & Gaster, M., 2005, "On Three-Dimensionality and Control of Incompressible Cavity Flow," Physics of Fluids, **17-104103**.

[23] Krishnamurty, K., 1956, "Sound Radiation from Surface Cutouts in High Speed Flow," PhD dissertation, California Institute of Technology, CA.

[24] Rogallo, R. S. & Moin, P., 1984, "Numerical Simulation of Turbulent Flows" Annual Review of Fluid Mechanics, **16**, pp. 99–137.

[25] Liliedahl, D.N., Carpenter, F.L., Cizmas, P.G.A., "Prediction of Aeroacoustic Resonance in Cavities of Hole-Pattern Stator Seals", Journal of Engineering for Gas Turbines and Power, **133,** pp. 022504-1-10.

[26] John, J.E.A., Keith, T.G., 2006, *Gas Dynamics,* Prentice Hall, Upper Saddle River, NJ.

[27] Morrison, G.L., 2008, "Gas Dynamics Class Notes," Texas A&M University, College Station, TX.

[28] Vannarsdall, M., "Reference manual for test cell 130", Turbomachinery Laboratory, Texas A&M University, College Station, TX.

[29] Fluent, ANSYS., 2010, *Fluent Theory Guide.* Fluent Theory Guide, SAS IP, Inc.

[30] Gloerfelt, X., "Lectures on Cavity Noise," Arts et M´etiers ParisTech, France.

[31] Ho, C.-M. & Huerre, P., 1984, "Perturbed Free Shear Layers," Annual Review of Fluid Mechanics, **16**, pp. 365–424.

[32] Miksad, R.W., 1972, "Experiments on the Nonlinear Stages of Free-Shear-Layer Transition," Journal of Fluid Mechanics, **56(4)**, pp. 695–719.

[33] Pope, S.B., 2000, *Turbulent Flows,* Cambridge University Press, Cambridge, UK.

[34] Forestier, N., 2001, "Etude exp´erimentale d'une couche cisaill´ee au-dessus d'une cavit´e en r´egime transonique," Ph.D. thesis, Ecole Centrale de Lyon. No NT 2001-1.

[35] Naudascher, R., Rockwell, D., 2005, *Flow-induced Vibrations: An Engineering Guide,* Dover Publications, New York, USA.

[36] Bajaj, A.K., Garg, V.K., 1977, "Linear Stability of Jet Flows," ASME Transactions, Series E - Journal of Applied Mechanics, **44**, pp. 378-384.

[37] Gloerfelt, X., Bogey, C., Bailly, C. & Juv´e, D., 2002, "Aerodynamic Noise Induced by Laminar and Turbulent Boundary Layers Over Rectangular Cavities," AIAA Paper, 2002-2476.

[38] Moon, H. T., Weidman, P. D., 1988, "Local Vortex Pairing in a Free Shear Layer," Physics of Fluids, **31** , pp. 3804-3806.

[39] Ho, C.-M. & Huang, L.-S., 1982, "Subharmonics and Vortex Merging in Mixing Layers," Journal of Fluid Mechanics., **119**, pp. 443–473.

[40] Rockwell, D., Knisely, C., 1979, "The Organized Nature of Flow Impingement upon a Corner," Journal of Fluid Mechanics., **93**, pp. 413–432.

[41] Liu, X.F., Katz, J., 2008, " Cavitation Phenomena Occurring Due to Interaction of Shear Layer Vortices With the Trailing Corner of a Two-Dimensional Open Cavity, " Physics of Fluids. **20**(4), pp. 041702-1-4.

[42] Bogey, C., 2000, "Calcul direct du bruit a´erodynamique et validation de mod`eles acoustiques hybrides," Ph.D. thesis, Ecole Centrale de Lyon. No 2000-11.

[43] Mathieu, J., Scott, J., 2000, *An Introduction to Turbulent Flow,* Cambridge University Press, Cambridge, UK.

[44] Ortega, J.M., 2001, "Stability Characteristics of Counter-Rotating Vortex Pairs in the Wakes of Triangular-Flapped Airfoils," PhD. Dissertation, Department of Mechanical Engineering, University of California at Berkley, Berkley, CA.

[45] Brandt, T., 2007, "Study on Numerical and Modelling Errors in LES using A Priori and A Posteriori Testing," DSc. Dissertation, Department of Mechanical Engineering, Helsinki University of Technology, Espoo, Finland.

[46] Geurts, B. J., Fröhlich, J., 2002, "A Framework for Predicting Accuracy Limitations in Large-Eddy Simulation," Physics of Fluids, **14** (6), pp. L41-L44.

[47] Meyers, J., Geurts, B. J., Baelmans, M., 2003, "Optimality of the Dynamic Procedure for Large-Eddy Simulations," Physics of Fluids, **17,** pp. 045108-1-9.

[48] Coleman, H.W, 1989, "Experimentation and Uncertainty Analysis for Engineers," John Wiley & Sons Inc., New York, NY.

APPENDIX A

GRID INDEPENDENCE STUDY

In the context of any CFD study, it is necessary to ensure that the solution obtained is not only physically appropriate but also numerically justified. This is done by carrying out a grid independence study which involves successive refinements of the grid and monitoring resulting changes in the solution. Another reason for carrying out a grid independence study is to ensure computational efficiency – i.e. to ensure that the gird used is not of very high resolution when not required by the problem

In case of an LES, a grid-independent LES refers to a simulation where the grid resolution is increased to a level where the effect of numerics is negligible while the effect of the SGS model is preserved [45]. The method applied for the present study is based on that used by Geurts and Fröhlich [46] and Meyers at al [47] who applied an implicit filtering provided by the Smagorinsky model (which is the technique used by FLUENT) and approached a grid independent solution by increasing the grid resolution while keeping the model length scale constant.

It is suggested that while employing the standard Smagorinsky model, the grid-independent solution can be approached by keeping the product of the Smagorinsky constant, C_S and the length scale Δ_S constant as the grid is refined. This approach looks at the LES equations as a set of differential equations with $\Delta_S C_S$ as an externally defined parameter (which is a function of the grid resolution) [45]. The reader is referred to Geurts and Fröhlich [46] for a detailed explanation of the formulation and

implementation of these parameters. Applying these concepts, a grid independence study was carried out for each of the simulations in the present study. Fig.59 is a representation of the results from the grid independence study carried out for the open cavity (i.e. without the top boundary) with L/D = 2. As done to determine statistical stability, the pressure at an upstream point is monitored over time and the results are compared to determine the effect of the grid on the solution. From Fig. 59, it can be seen that although the coarse grid under predicts the solution by a factor of two (at the most), the medium grid provides a good estimate of the solution while ensuring computational accuracy.

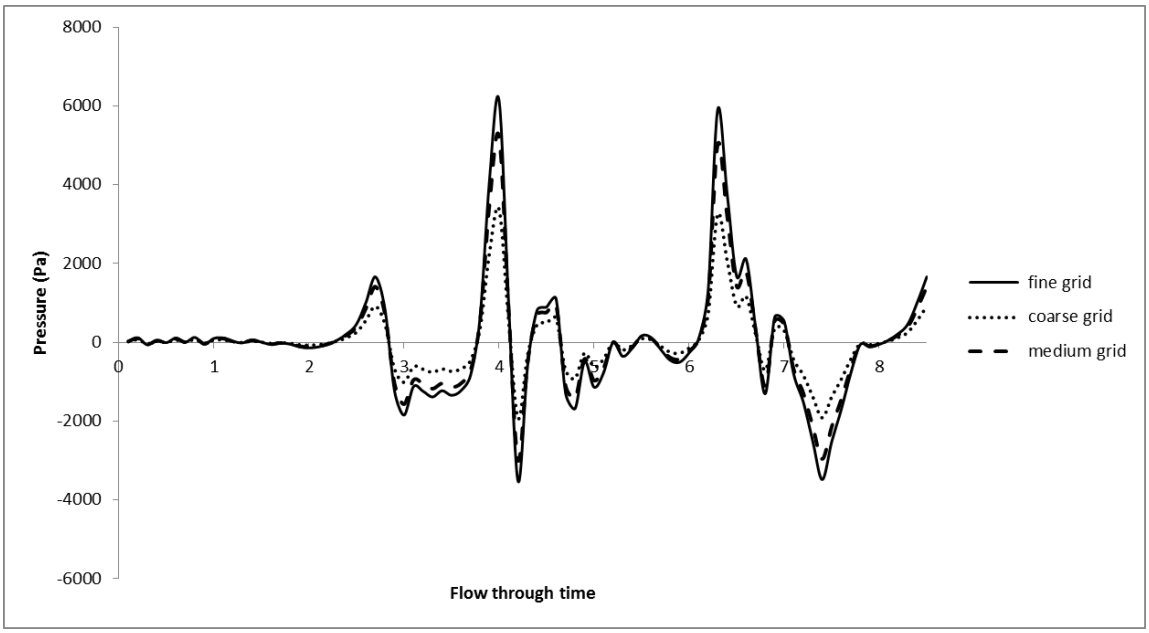

Figure 59 – Variation of pressure with FTT to compare solutions from different grids

Table 1. Details of three meshes used during grid independence studyfor cavity with L/D = 2

Grid	**Number of node points in cavity**
Coarse	425 X 375
Medium	720 X 630
Fine	850 X 750

APPENDIX B

UNCERTANITY ANALYSIS

A quantitative measure of the accuracy of an experimental procedure is determined by carrying out an uncertainty analysis of the data. The result of this procedure is a combination of errors due to instrumentation and methodology and allows for an accurate interpretation of the experimental data. The following section details the computation of uncertainties in Mach number and friction factor using the Kline – McClintock single measurement technique (a thorough account of this procedure can be found in [48]). According to this method, the uncertainty in a variable R that is a function of n variables, $x_1, x_2, x_3 \ldots . x_n$ is given by the following relation –

$$w_R = \sqrt{\left[\frac{\partial R}{\partial x_1} w_1\right]^2 + \left[\frac{\partial R}{\partial x_2} w_2\right]^2 + \left[\frac{\partial R}{\partial x_3} w_3\right]^2 + \cdots + \left[\frac{\partial R}{\partial x_n} w_n\right]^2} \tag{36}$$

The same technique was also used by Kheireddin [2] to compute the uncertainty of the values in his experiments. Looking at Eq. (15), the primary variables are $\dot{m}, P, A$ and T_t- the uncertainties in these variables are taken to be 1.7 e-5 kg/sec, 0.008 bar, 1.29 e-6 m^2 and 1^o K respectively. Differentiating each term of Eq. (15) with respect to the primary variables –

$$\frac{\partial M}{\partial P} = \frac{-\frac{1}{P}\left(\frac{\dot{m}}{PA}\right)^2\left(\frac{RT_t}{\gamma}\right)}{M\sqrt{1+0.8\left(\frac{\dot{m}}{PA}\right)^2\frac{RT_t}{\gamma}}} \tag{37}$$

$$\frac{\partial M}{\partial A} = \frac{-\frac{1}{A}\left(\frac{\dot{m}}{PA}\right)^2\left(\frac{RT_t}{\gamma}\right)}{M\sqrt{1+0.8\left(\frac{\dot{m}}{PA}\right)^2\frac{RT_t}{\gamma}}} \tag{38}$$

$$\frac{\partial M}{\partial \dot{m}} = \frac{\dot{m}\left(\frac{\dot{m}}{PA}\right)^2\left(\frac{RT_t}{\gamma}\right)}{M\sqrt{1+0.8\left(\frac{\dot{m}}{PA}\right)^2\frac{RT_t}{\gamma}}} \tag{39}$$

$$\frac{\partial M}{\partial T_t} = \frac{\left(\frac{\dot{m}}{PA}\right)^2\left(\frac{R}{\gamma}\right)}{2M\sqrt{1+0.8\left(\frac{\dot{m}}{PA}\right)^2\frac{RT_t}{\gamma}}} \tag{39}$$

Accordingly, the maximum uncertainty in the Mach number is calculated to be around 2.2 %. Similarly, for the friction factor, from Eq. (10) –

$$\frac{\partial f}{\partial H} = \frac{4\left(1-M^2\right)}{1.4M^3(1+0.2M^2)}\frac{dM}{dx} \tag{40}$$

$$\frac{\partial f}{\partial (dx)} = \frac{4H\left(1-M^2\right)}{1.4M^3(1+0.2M^2)}\frac{dM}{(dx)^2} \tag{41}$$

$$\frac{\partial f}{\partial (M)} = \frac{8C_P\,(3\,M^4\gamma-3M^4-5M^2\gamma+7M^2-6)}{1.4M^3(1+0.2M^2)^2}\frac{dM}{dx} \tag{42}$$

The estimated maximum uncertainty from this equation is 2.5 %.